

5-2013

Quantum Resonant Beats and Revivals in the Morse Oscillators and Rotors

Zhenhua Li

University of Arkansas, Fayetteville

Follow this and additional works at: <http://scholarworks.uark.edu/etd>



Part of the [Quantum Physics Commons](#)

Recommended Citation

Li, Zhenhua, "Quantum Resonant Beats and Revivals in the Morse Oscillators and Rotors" (2013). *Theses and Dissertations*. 813.
<http://scholarworks.uark.edu/etd/813>

This Dissertation is brought to you for free and open access by ScholarWorks@UARK. It has been accepted for inclusion in Theses and Dissertations by an authorized administrator of ScholarWorks@UARK. For more information, please contact scholar@uark.edu.

Quantum Resonant Beats and Revivals in the Morse Oscillators and Rotors

Quantum Resonant Beats and Revivals in the Morse Oscillators and Rotors

A dissertation submitted in partial fulfillment
of the requirements for the degree of
Doctor of Philosophy in Microelectronics-Photonics

By

Zhenhua Li
Zhongshan University
Bachelor of Science in Physics, 1995
University of North Dakota
Master of Science in Physics, 2005

May 2013
University of Arkansas

Abstract

Analytical eigenfunctions and eigenvalues for the Morse oscillator were applied to investigate the quantum resonant beats and revivals of wave packet propagation. A concise way for exact prediction of the complete revival period of the Morse oscillator was given for the first time. It was suggested that any complete period was made of integer numbers of the minimum or fundamental period. Within the fundamental period, the anharmonicity of this oscillator appeared to cause interesting space-time phenomena that include relatively simple Farey-sum revival structures. In addition, a simple sum of two Morse oscillators led to a double-Morse well whose geometric symmetry provided analytical eigenfunctions and eigenvalues for certain low-lying energy levels. The quantum tunneling between the double-Morse well significantly affected the resonant beats and revivals local to each well, and gave rise to interesting tsunami-like waves in the middle of the double well. Furthermore, quantum rotor wave functions based upon Wigner-D matrix were applied to investigate the quantum resonant beats and revivals that occur in experimentally accessible spin systems. Interesting physical effects in quantum rotors between half-integer spin and integer spin systems were observed to show effects of symmetry. Essentially, the quantum revivals in these quantum systems exhibited number-information aspects of surprisingly simple Farey-sum and Ford circles geometry. Such quantum dynamics will provide a physical insight to further develop matter wave packet technology, and might have applications for quantum information processing and quantum computing.

**This dissertation is approved for recommendation
to the Graduate Council.**

Dissertation Director:

Dr. William G. Harter

Dissertation Committee:

Dr. Daniel Kennefick

Dr. R. Panneer Selvam

Dr. Surendra P. Singh

Prof. Ken Vickers

The following signatories attest that all software used in this dissertation was legally licensed for use by Mr. Zhenhua Li for research purposes and publication.

Student: Zhenhua Li

Professor: William G. Harter

This dissertation was submitted to <http://www.turnitin.com> for plagiarism reviewed by the TurnItIn company's software. The signatories have examined the report on this thesis that was returned by TurnItIn and attest that, in their opinion, the items highlighted by the software are incidental to common usage and are not plagiarized material.

Prof. Ken Vickers, Program Director

Dr. William G. Harter, Dissertation Director

©2013 by Zhenhua Li
All Rights Reserved

Dissertation Duplication Release

I hereby authorize the University of Arkansas Libraries to duplicate this dissertation when needed for research and/or scholarship.

Agreed

Zhenhua Li

Refused

Zhenhua Li

Acknowledgements

I wish to express my appreciation to Professor William Harter, who encouraged me to explore the geometrical aesthetic and physical insight throughout this two years investigation. This is clearly a force of his curiosity and enthusiasm with physics and mathematics to steer me down a wonderful track after switching from 4 academic advisors in two universities during my 10 years Ph.D. long-haul journey.

I would never have been able to finish my dissertation within one year unless I had the assistance and guidance of Professor Ken Vickers, who encouraged me to skill in professional time management and entrepreneurship. Also, I take this opportunity to thank the wonderful people in his Microelectronics-Photonics program and Physics department including secretary Renee Hearon and colleagues Sabina Koukourinkova, Nikhil Thomas, Jeevaka Weerasinghe, and Zhigang Gui.

I am indebted to Thalia & Todd Ballinger family, Elizabeth & Maynard Sandol family, Becky & Edward Bedore family, Marin & Dale Bergsrud family, Becky & Cory family, and Fang & Bin Fan family. These wonderful American friendship families have enriched my life profoundly.

My special thanks go to my friends including Beau Bedore, Corey Bergsrud, Wang Lily, and Dr. Chen Jun, and my relatives including my uncle, Li RuiXing, and my cousins, Li Qin, Chen WeiHui and Weng ChunLi.

My deepest thanks go to my parents, Li Fei and Chen CaiLian, and my brothers, Li JinQiang and Li JinGang, for their priceless encouragement and patience with the best wishes.

Dedication

This Ph.D. is dedicated to my parents, 李飞 & 陈彩莲, and my brothers, 李进强 and 李进钢 for the perseverance.

Table of Contents

Chapter 1: Introduction	1
Chapter 2: Morse Oscillator	7
2.1 Analysis of Exact Revival Period T_{rev}	11
2.2 Fibonacci Sequence and Exchange Rate of $\frac{T_{min-rev}}{T_{max-beat}}$	17
2.3 Farey Sequence and Ford Circles within a Perfect Minimum Revival Period	20
2.3.1 Autocorrelation Function and Farey-sum Sequence	22
2.3.2 Ford Circles Geometry for Quantum Revivals	24
2.4 Conclusion of Morse Oscillator	27
Chapter 3: Double-Morse Oscillator	28
3.1 A Genuine Double-Morse Potential	30
3.1.1 High Fidelity between a Razavy Potential and a Specified Double-Morse potential	32
3.1.2 Exact Eigenfunctions and Eigenvalues of a Deep Double-Morse Potential	37
3.2 Resonant beats and Revivals from Tunneling States	42
3.3 Tsunami-like Resonant Beats and Revivals from Non-tunneling States	43
3.4 Conclusion of Double-Morse Oscillator	44
Chapter 4: Quantum Rotor	45
4.1 Symmetric Rigid Rotor	45
4.1.1 Wigner-D Matrix — a Rotation Matrix for Any Spin	46
4.1.2 Quantum Rotor Wave Function	49
4.2 Resonances and Revivals in Quantum Rotor	50
4.2.1 Integer Spin — Boson System	50
4.2.2 Half-integer Spin — Fermion System	62
4.3 Conclusion of Rotor Dynamics	74

Chapter 5: Conclusion	75
References	76
Appendix A: Description of Research for Popular Publication	80
Appendix B: Executive Summary of Newly Created Intellectual Property	81
Appendix C: Potential Patent and Commercialization Aspects of Each Numbered Item in Appendix B	82
C.1 Patentability of Intellectual Property	82
C.2 Commercialization Possibilities of Intellectual Property	82
C.3 Possible Prior Disclosure of Intellectual Property	83
Appendix D: Broader Impact of Research	84
D.1 Applicability of Research Methods to Other Problems	84
D.2 Impact of Research Results on U.S. and Global Society	84
D.3 Impact of Research Results on the Environment	84
Appendix E: Microsoft Project Printout of Microelectronics-Photonics PhD Degree Plan	85
Appendix F: Identification of All Software Used in Research and Dissertation Generation	89
Appendix G: All Publications Published, Submitted and Planned	90
G.1 Publications in Journal Papers	90
G.2 Publications in Conference Abstracts and Contributed Talks	90
Appendix H: My Source Codes in Mathematica™	91

Chapter 1

Introduction

The study of wave packet dynamics has a long history, and has more recently been accelerated by modern computer technology that provides better ways to visualize spatial and temporal behaviors. Wave packet dynamic systems have been studied for over 200 years in a wide scope: from classical tsunami waves to electromagnetic non-dispersive solitary waves. In 1926, Erwin Schrodinger developed quantum matter wave for the solutions of Schrodinger's equation [1]. Since then, the dynamic behaviors of quantum wave packets have been active research topics in atomic physics and molecular chemistry. In a theoretical way, quantum wave packet studies served as the solid steppingstone to the birth of quantum optics in 1963 [2], where Glauber's work on the quantum theory of optical coherence was based on the coherent states of quantum harmonic oscillator in Figure 1.1. This work led him to become the 2005 Nobel Laureate in Physics [3].

A coherent state is a remarkable example for the correspondence principle that connects classical and quantum physics. The wave packet of this coherent state keeps the same shape as the ground state, but its time propagation is concentrated along the classical trajectories of a classical harmonic oscillator. The moving path of a coherent state of quantum harmonic oscillator is illustrated in Figure 1.1 (d-f). The coherent states are important for comparing the wave-like and particle-like behavior of quantum systems.

In an experimental way, a milestone of the quantum wave packet study was reached in 1987 through Zewail's work on the transition states of chemical reactions using femto-second ($10^{-12}s$) spectroscopy [4]. His investigation of ultra-fast chemical phenomena was based on the observation of coherent wave packet motion between covalent and ionic states. This work marked the birth of femto-chemistry, and led him to become the 1999 Nobel Laureate in Chemistry [5]. The generation of vibrational wave packet of molecular electrons is described in Figure 1.2. In the case of monochromatic light as shown in Figure 1.2 (a), only one stationary state is excited. While, in case of femto-second laser pulse as shown in Figure 1.2 (b), the intrinsic bandwidth of this ultra-short laser pulse is broad enough to excite several stationary states simultaneously. These excited

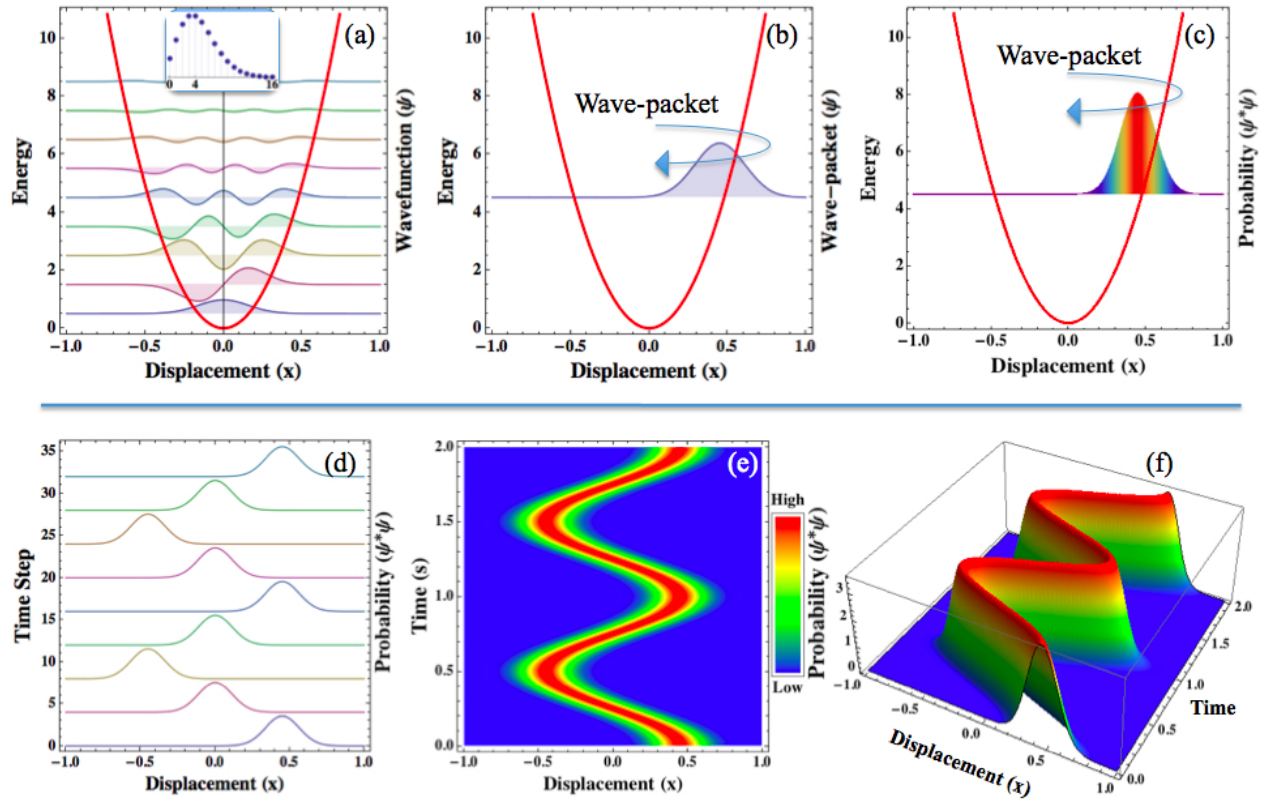


Figure 1.1: Coherent state of quantum harmonic potential: (a) A branch of eigenfunctions in the potential well (red-color-line) is scaled by the Poisson-distribution (dotted-line) for keeping the minimum-uncertainty, and (b) superposed together to form a coherent eigenfunction-wave-packet, which establishes (c) the corresponding coherent probability-wave-packet. (d) A branch of the coherent probability-wave-packets as a function of time-step. (e) The probability density map of the coherent wave packet as a function of space-time. (f) The 3-dimensional (3D) probability distribution map of the coherent wave packet as a function of space-time.

electronic stationary states are superposed together to form a propagating wave packet, as shown in the top of Figure 1.2 (b). The resulting wave packets can be seen as a linear combination of the oscillator's eigenfunctions

$$\psi(x, t) = \sum_{n=0}^N c_n \phi_n(x) e^{-iE_n t/\hbar} \quad (1.1)$$

where $\phi_n(x)$ denotes the n -th order eigenfunction, c_n stands for the n -th order constant coefficient, $e^{-iE_n t/\hbar}$ is the complex exponential factor related with time t . The wave packets established by various ultra-fast light pulses are applied for a detailed understanding of molecular dynamics, which is of fundamental interest in physics and chemistry.

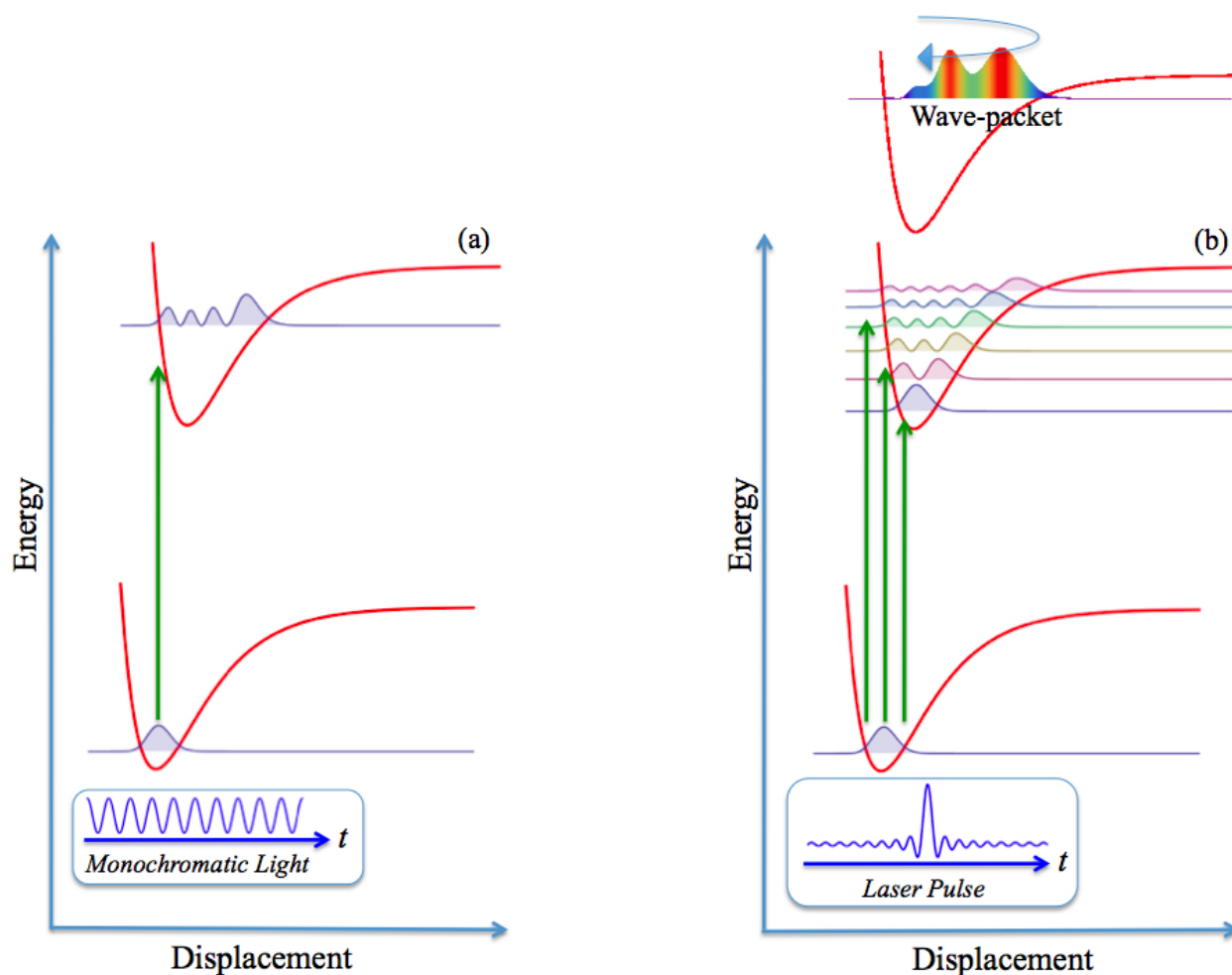


Figure 1.2: Generation of quantum dynamic wave packet in potential well (red-color-line). (a) Monochromatic light is able to excite only one stationary state. (b) An ultra-fast laser pulse is capable to excite a branch of stationary states that superpose into a wave packet.

In the late 1970s and the early 1980s, quantum wave packet studies began with revivals in cavity quantum electrodynamics simulations by Eberly [6] and computer simulations of molecular vibrational dynamics [7, 8]. With the birth of ultra-fast laser spectroscopy in the late 1980s, it became possible to observe quantum wave packet resonance and the localized periodic motion in many experimental situations [4, 9, 10] involving atoms, molecules, and cavities [10, 11]. Considerable progress has been made in understanding the physics and chemistry of ultra-fast spectroscopy and laser-molecular interaction [11, 12]. Many of existed research groups focus on real-time experimental observation and simulation. For instance, a quantum dynamics group in the Max-Planck-Institute simulated its real-time observation of vibrational revival in laser-molecular interaction [10], whereas numerical simulation exhibits qualitative agreement with its laser-induced H_2 ionization experimental data, as shown in Figure 1.3.

However, a relatively small fraction of the research involves aspects of number-theory or information-theory that shows up in the space-time complexity of quantum wave packet dynamics. This is still a largely unexplored field. In 2001, Harter published two pioneering papers addressing the dynamics of wave-packet in a simple quantum rotor system with C_n -group and Farey-sum analysis [13, 14], his works were cited by Schleich's group as a potential application for factorizing numbers [15, 16]. In the past decade, the examination of number-information was limited to wave packets confined by one dimensional infinite-square-wells or flat ring potentials, as shown in Figure 1.4. In 2011, the author demonstrated that anharmonic Morse potential well exhibits similar Farey-sum arithmetic revival structure in its wave packet propagation [17]. This work motivated the author to do a closer examination of the resonance and revival phenomena among various quantum systems, especially the double-Morse potential wells and the dynamic quantum rotors. This new work is the topic of this dissertation and should provide a further step towards a systematic understanding of the rich and diverse behavior of quantum wave packet dynamics.

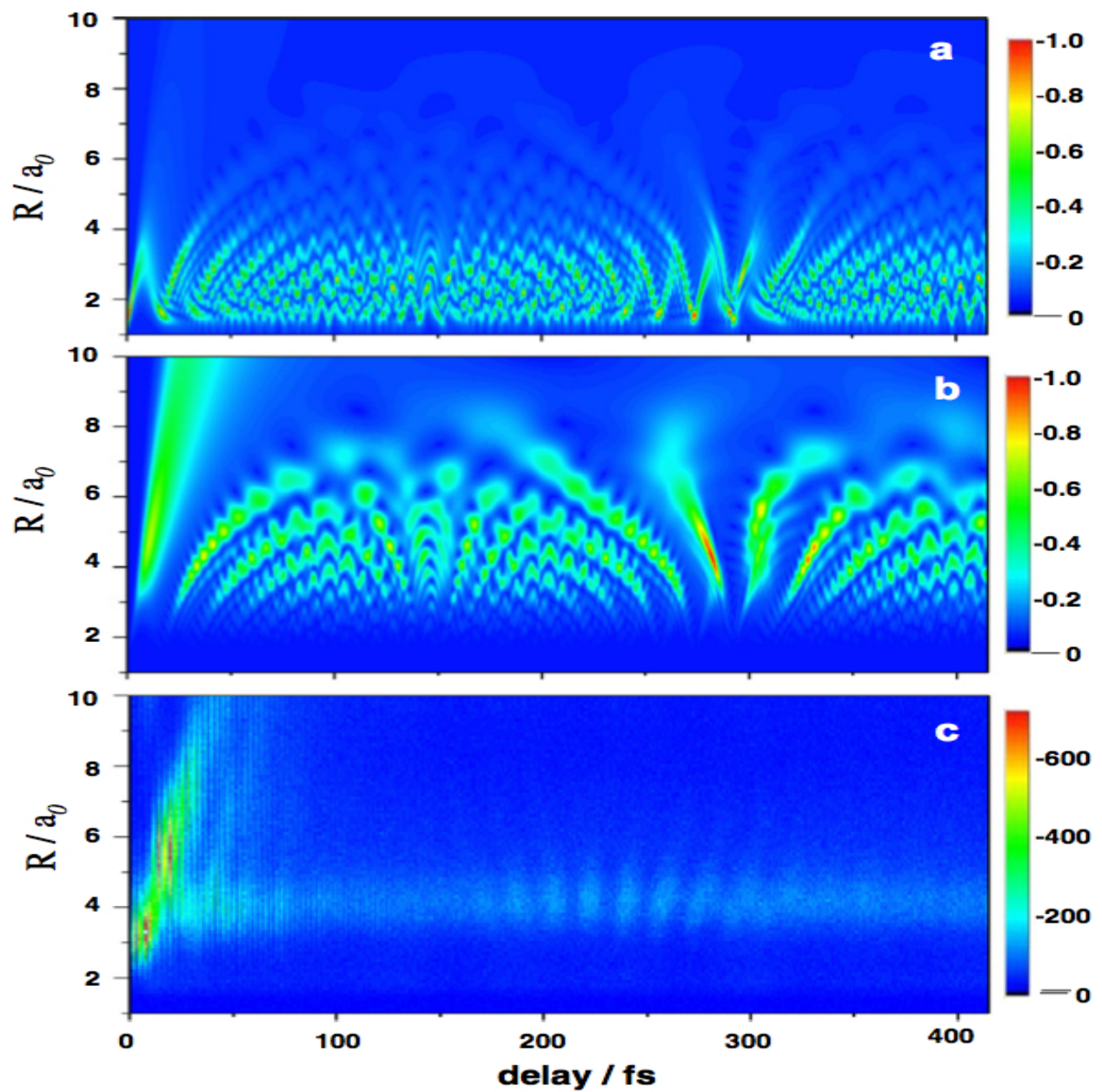


Figure 1.3: Research approach from Ullrich's group in Max-Planck-Institute. (a) Numerical calculated probability plot of H_2^+ wave packet propagation. (b) The same calculated probability plot as (a) but weighted by the ionization probability. (c) H_2^+ wave packet is rebuilt from experimental data of laser-ionization [10].

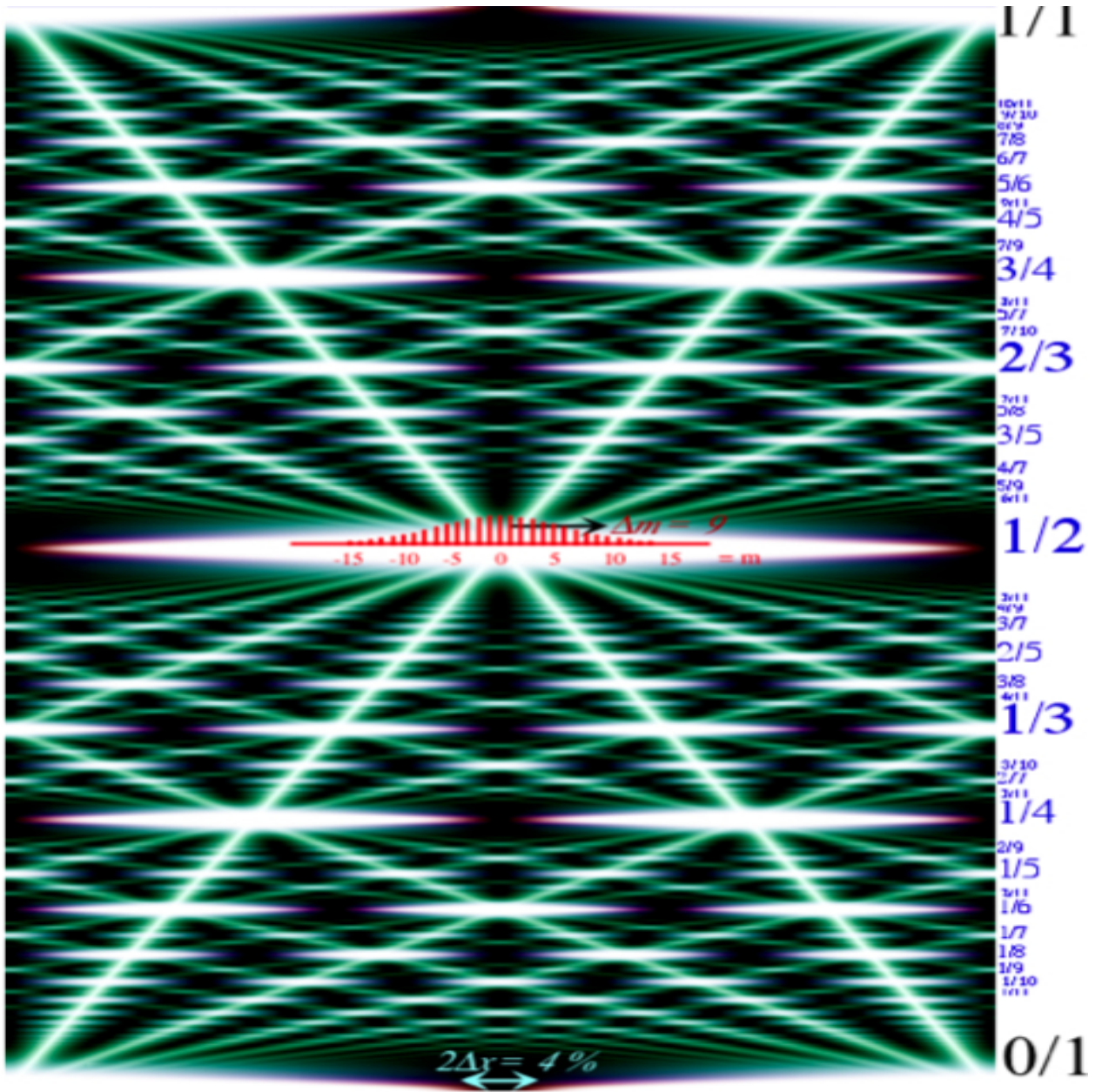


Figure 1.4: Research approach from Harter's group at University of Arkansas. The Farey-sum structure in the quantum revivals of a Bohr ring [13].

Chapter 2

Morse Oscillator

The Morse oscillator is representing a simple but realistic choice among various anharmonic potentials [18]. Experimentally, the Morse-type anharmonic oscillators have been applied widely for the description of covalent molecular bonding, and some important dynamic aspects of this anharmonic oscillator have been studied [19, 20, 21, 22, 23]. Mathematically, the Morse potential is one of the simplest models for describing the anharmonicity of real chemical bonding, and is given by

$$V_M(x) = D(1 - e^{-\alpha x})^2 \quad (2.1)$$

In this one dimensional model of Equation 2.1, the coefficient D is the bond dissociation energy where the potential approaches its maximum inflection value as x approaches $+\infty$, it relates to both harmonic frequency ω_e and anharmonic frequency ω_χ , and is found by the equation

$$D = \frac{\omega_e^2}{4\omega_\chi} \hbar \quad (2.2)$$

The constant parameter α regulates the “width” of the Morse potential well by associating the reduced mass μ and anharmonic frequency ω_χ , and is found by the relation

$$\alpha = \sqrt{\frac{2\omega_\chi\mu}{\hbar}} = \sqrt{\frac{\omega_e^2\mu}{2D}} \quad (2.3)$$

The coordinate x denotes the variation of a chemical bond from its equilibrium length, and where the potential has its minimum and zero value at $x = 0$.

Recently McCoy [24] revived interest in exact eigenfunctions and eigenvalues [25] of Morse oscillator as shown in Equation 2.4 and Equation 2.5a below. This allows analytical analysis of their quantum dynamics that may shed light on dynamics of extended Morse-type systems and anharmonic potentials in general.

The Morse oscillator, as an anharmonic oscillator, has unequal spacing between its energy

levels which is in contrast with the uniform energy level spacing of harmonic oscillator. The energy levels $E_n = \hbar\omega_n$ in Equation 2.4 have uniform (harmonic) spacing $\Delta E = \hbar\omega_e$ compressed at higher quantum number n if anharmonic frequency ω_χ is positive.

$$E_n = \hbar\omega_n = \hbar\omega_e\left(n + \frac{1}{2}\right) - \hbar\omega_\chi\left(n + \frac{1}{2}\right)^2 \quad (2.4)$$

The corresponding Morse eigenfunctions of the eigenvalues are given by Equation 2.5a where L_n^{2s} represents a generalized associated Laguerre polynomial [24].

$$\phi_n(x) = e^{\frac{-y(x)}{2}} y(x)^{s(n)} \sqrt{\frac{\alpha(\nu - 2n - 1)n!}{\Gamma(\nu - n)}} L_n^{2s(n)}(y(x)) \quad (2.5a)$$

The exponentially scaled coordinate $y(x)$, and exponent $s(n)$ are given as follows

$$y(x) = \nu e^{-\alpha x} \quad (2.5b)$$

$$s(n) = \frac{1}{2}(\nu - 2n - 1) \quad (2.5c)$$

Here, the scaling parameter ν is given as

$$\nu = \frac{4D}{\hbar\omega_e} \quad (2.5d)$$

A linear combination of the stationary eigenfunctions will give rise of a dynamic wave packet

$$\psi(x, t) = \sum_{n=0}^{n_{max}} c_n \phi_n(x) e^{-i\frac{E_n t}{\hbar}} \quad (2.6)$$

where n_{max} is the highest bound state that its eigenvalue is the nearest value to dissociative limit D , c_n stands for the n -th order constant coefficient, and $e^{-iE_n t/\hbar}$ is the complex exponential factor related with time t .

A sample Morse oscillator potential shown in Figure 2.1 (a) was made of harmonic frequency

$\omega_e/2\pi c = 18(\text{cm}^{-1})$ and anharmonic frequency $\omega_\chi/2\pi c = 1(\text{cm}^{-1})$, and each of its stationary eigenfunction ϕ_n was plotted on a energy level of eigenvalue E_n . If the initial wave packet (Equation 2.6 at $t = 0$) is a sum of nine stationary bound states (from $n = 0$ to $n_{max} = 8$) shown in Figure 2.1 (b), it evolves in space and time as shown in Figure 2.1 (d-f) ending in the lowest $\Psi(x, T)$ trace of Figure 2.1 (d) with a full revival of its initial shape.

For simplicity, the constant coefficient $c_n = 1$ is assumed in this Morse oscillator research. The space-time plots of the probability $\Psi(x, t)^*\Psi(x, t)$ in Figure 2.1 (e-f) show quantum beats in space and time. The resonant beat nodes and anti-nodes in Figure 2.1 (e-f) outline semi-classical trajectories $x(t)$ corresponding to energy values E_n ranging from the lowest ground state E_0 up to the highest $E_{n_{max}}$.

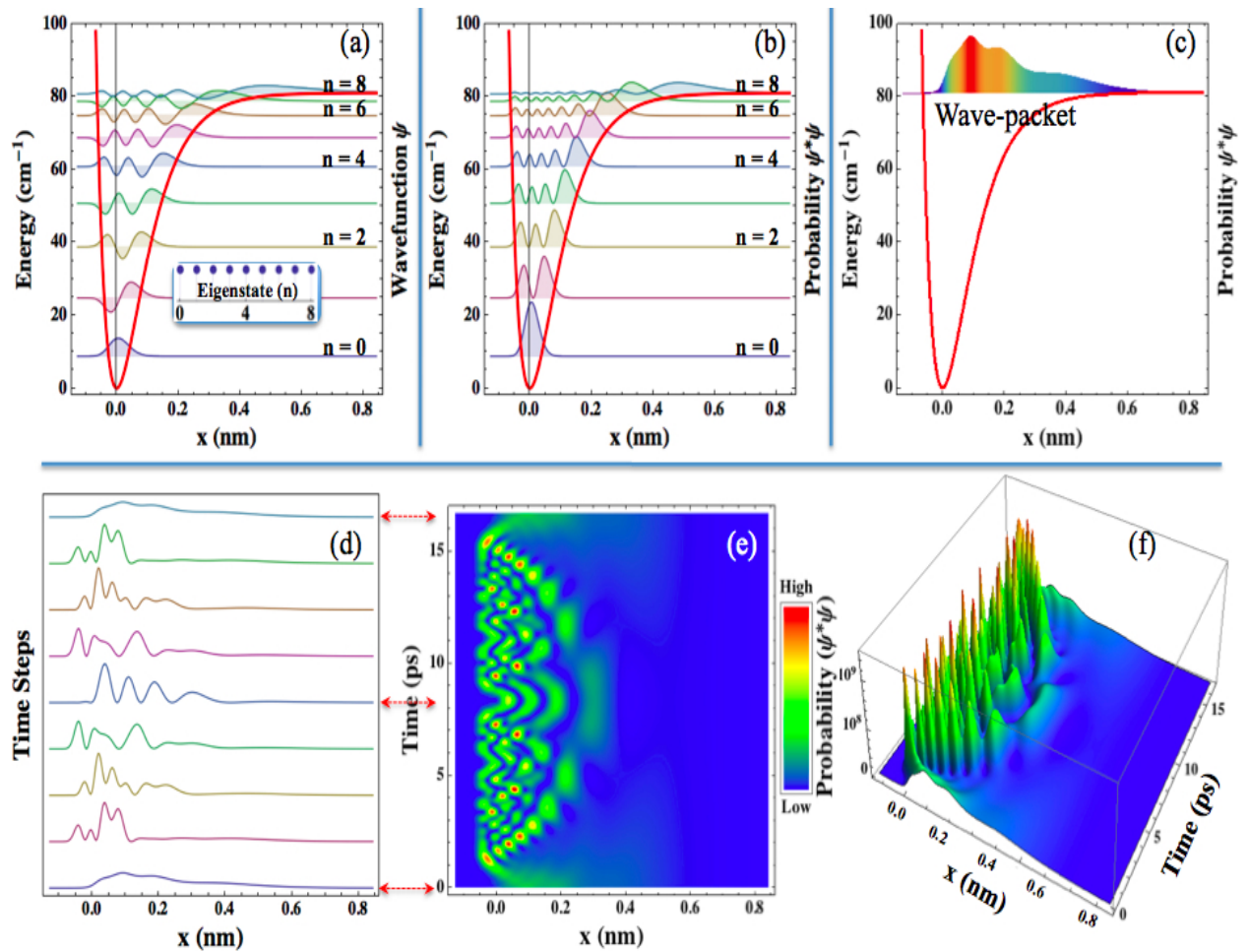


Figure 2.1: The Morse oscillator with harmonic frequency $\omega_e/2\pi c = 18(\text{cm}^{-1})$ and anharmonic frequency $\omega_x/2\pi c = 1(\text{cm}^{-1})$. (a) A total of 9 bound stationary states is listed along the corresponding energy level in the potential well (red-color-line), these wave functions are normalized (indicated by the same-height dotted-line). (b) The probability distribution of these stationary states is listed along the corresponding energy level in the potential well. (c) The corresponding probability-wavepacket is formed by the superposition of these bound eigenstates at $t = 0$. (d) The wavepacket is propagated along the time-steps. (e) The probability density map of the wavepacket as a function of space and time. The double arrows connecting (d)-(e) indicate the corresponding time events. (f) The 3 dimensional (3D) probability distribution map of the wave packet as a function of space and time.

2.1 Analysis of Exact Revival Period T_{rev}

In the analysis of wave packet dynamics in anharmonic oscillating system, the first essential and challenge thing is to do a prediction of the exact revival period of the wave packet. Suppose T is the revival period time, the wave packet function satisfies $\psi(x, t) = \psi(x, t + T)$, and is expressed as

$$\psi(x, t) = \sum_{n=0}^N \phi_n(x) e^{-i \frac{E_n}{\hbar} t} = \psi(x, t + T) = \sum_{n=0}^N \phi_n(x) e^{-i \frac{E_n}{\hbar} (t+T)} \quad (2.7a)$$

When $t = 0$, it becomes

$$\psi(x, 0) = \sum_{n=0}^N \phi_n(x) = \psi(x, T) = \sum_{n=0}^N \phi_n(x) e^{-i \frac{E_n}{\hbar} T} \quad (2.7b)$$

For nontrivial solution, it demands

$$\phi_n(x) = \phi_n(x) e^{-i \frac{E_n}{\hbar} T} \quad (2.7c)$$

Then, it requires

$$\frac{E_n}{\hbar} T = 2\pi M_n \quad (2.7d)$$

where M_n are integers. When E_n is substituted by the Morse energy level Equation 2.4, this requirement becomes

$$E_n T = [(n + \frac{1}{2})\omega_e - (n + \frac{1}{2})^2 \omega_\chi] T = 2\pi M_n \quad (2.7e)$$

It can be rewritten as

$$E_{n+1} T = [(n + 1 + \frac{1}{2})\omega_e - (n + 1 + \frac{1}{2})^2 \omega_\chi] T = 2\pi M_{n+1} \quad (2.7f)$$

where M_{n+1} are integers. Then the subtraction of above two nearby equations gives

$$E_{n+1}T - E_nT = [\omega_e - (2n + 2)\omega_\chi]T = 2\pi(M_{n+1} - M_n) \quad (2.7g)$$

Similarly, it can be rewritten as

$$E_{n+2}T - E_{n+1}T = [\omega_e - (2(n + 1) + 2)\omega_\chi]T = 2\pi(M_{n+2} - M_{n+1}) \quad (2.7h)$$

Then the subtraction of above two nearby equations gives

$$(E_{n+2}T - E_{n+1}T) - (E_{n+1}T - E_nT) = 2\omega_\chi T = 2\pi(M_{n+2} - 2M_{n+1} + M_n) \quad (2.7i)$$

Therefore, the revival period time of the Morse oscillator can be expressed concisely as

$$T = \frac{\pi}{\omega_\chi} \mathbb{M} \quad (2.8a)$$

where \mathbb{M} is integer coefficient. This concise revival period formula reveals two facts of the dynamic wave packets in the Morse oscillating system. The first fact is that the minimum or fundamental revival period is

$$T_{min-rev} = \frac{\pi}{\omega_\chi} \quad (2.8b)$$

which is exactly the shortest revival time for Morse oscillator found by Wang and Heller [23]. And the second fact is that any complete revival period is made of integer numbers of the fundamental period. In other words, any complete quantum trajectory must contain integer numbers of semiclassical-trajectory-profile period (the minimum revival period) which is approximately outlined by a classical particle oscillating with anharmonic frequency $2\omega_\chi$ in the Morse potential.

For illustrating the connection between semiclassical-trajectory-profile period and quantum period, consider three classical particles with corresponding quantum eigenvalue energies are oscillating in a Morse potential well as shown Figure 2.2 (a), where the rainbow-shape trajectory of a

classical particle with E_2 energy is having a classical oscillating period T close to the fundamental period of π/ω_χ . While the trajectory of classical particle with $E_3 = D$ energy indicates that this particle is escaping from the limit of the Morse potential well, and will never come back.

Above simple procedure provides a general revival period formula for the Morse oscillator straightforwardly. For practical applications, it is necessary to determine the integer coefficient \mathbb{M} of Equation 2.8a. In order to determine a specific integer \mathbb{M} for a specified Morse oscillator with given parameters (ω_e, ω_χ) , more analysis are required.

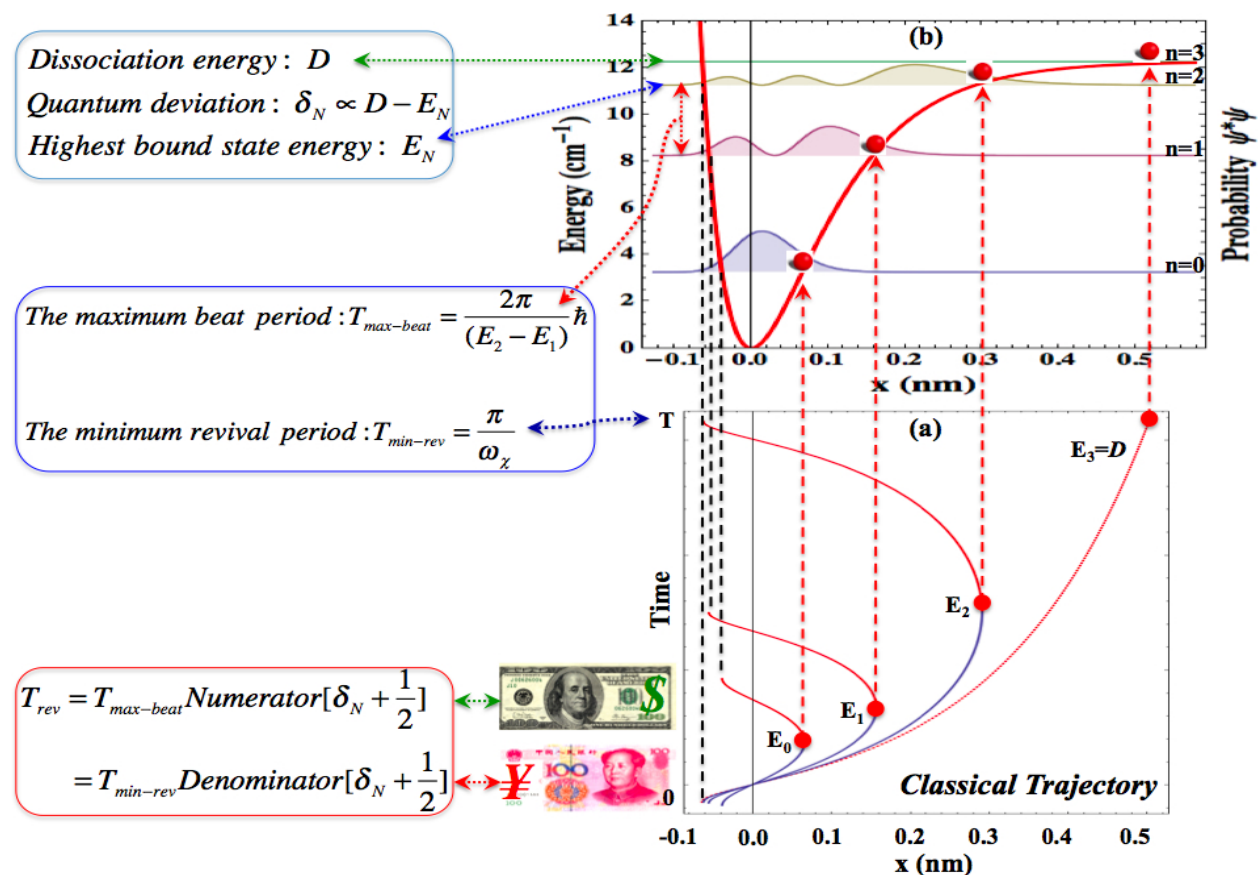


Figure 2.2: The connection between the maximum beat period and semiclassical-trajectory-profile period (the minimum revival period). (a) 3 classical trajectories of particles oscillating in a Morse potential are plotted in one period time, and one additional classical trajectory of particle with dissociation energy D is also plotted. The red-balls in (a) and (b) indicate that these classical particles have the same energies as the corresponding quantum eigenvalue energies. (b) The probability amplitudes of 3 bound quantum eigenfunctions are listed along energy level in a Morse potential (red-thick-line). In the bottom, two fundamental ways for predicting the same period are symbolized by two basic monetary units: the U.S. dollar and Chinese yuan.

The beating between waves with close frequency is playing key role in wave packet dynamics. Especially, the maximum beat period $T_{max-beat}$ generating by two closest bound energy levels in the Morse well is the key for searching revival period. A complete revival of $|\Psi(x, t)|^2$ at time T_{rev} must contain integer numbers of all beat periods including at least one fundamental time period $T_{max-beat}$ for the slowest beat frequency. This assumption of wave beat period is expressed as

$$T_{rev} = T_{max-beat}\mathbb{N} \quad (2.9)$$

where \mathbb{N} is integer coefficient. According to the Morse energy level Equation 2.4, the gap between energy levels is given

$$\Delta E = E_n - E_{n-1} = \hbar(\omega_e - 2\omega_\chi n) \quad (2.10)$$

This Equation 2.10 exhibits clearly that ΔE approaches minimum as n approaches maximum, which indicates the minimum energy gap is occurring between the highest bound quantum number n_{max} and n_{max-1} . Therefore, by the energy and frequency relationship $E = \hbar\omega$ of quantum matter wave, the maximum beat period between any two energy levels is expressed as

$$T_{max-beat} = \frac{2\pi}{(\Delta\omega)_{min}} = \frac{2\pi}{E_{n_{max}} - E_{n_{max-1}}} \hbar = \frac{2\pi}{\omega_e - 2\omega_\chi n_{max}} \quad (2.11)$$

For estimating the highest bound energy level n_{max} in above Equation 2.11, it is supposed that n_{max} is the integer part of a real number n_{real} . Thus, by substituting this real number n_{real} into the energy Equation 2.4, the resulted energy $E_{n_{real}}$ will be exactly equal to the dissociative limit D given by Equation 2.2. This equivalent relation is expressed as

$$E_{n_{real}} = \hbar\omega_e\left(n_{real} + \frac{1}{2}\right) - \hbar\omega_\chi\left(n_{real} + \frac{1}{2}\right)^2 = D = \frac{\omega_e^2}{4\omega_\chi} \hbar \quad (2.12a)$$

This is a perfect square equation with one root given by

$$n_{real} = \frac{\omega_e}{2\omega_\chi} - \frac{1}{2} \quad (2.12b)$$

The integer part of n_{real} (the floor of n_{real}) is the highest Morse quantum number n_{max} (For Figure 2.1, this is $n_{max} = 8$).

$$n_{max} = \text{Floor}[n_{real}] = \text{Floor}\left[\frac{w_e}{2\omega_\chi} - \frac{1}{2}\right] \quad (2.12c)$$

The following fractional part δ_N of n_{real} is called the quantum deviation between the dissociative limit D and the highest bound energy level.

$$\delta_N = n_{real} - n_{max} \quad (2.12d)$$

As illustrated in Figure 2.2(b), δ_N is proportional to energy gap between D and the highest bound energy level.

Then, the fundamental period $T_{max-beat}$ in Equation 2.11 can be expressed in term of δ_N as:

$$\begin{aligned} T_{max-beat} &= \frac{2\pi}{\omega_e - 2\omega_\chi n_{max}} = \frac{2\pi}{\omega_e - 2\omega_\chi(n_{real} - \delta_N)} = \frac{2\pi}{\omega_e - 2\omega_\chi\left(\frac{\omega_e}{2\omega_\chi} - \frac{1}{2} - \delta_N\right)} \\ &= \frac{\pi}{\omega_\chi\left(\delta_N + \frac{1}{2}\right)} \end{aligned} \quad (2.13a)$$

By applying the fact of $T_{min-rev} = \pi/\omega_\chi$ given by Equation 2.8b, above Equation 2.13a can be rewritten as

$$T_{max-beat} = \frac{\pi}{\omega_\chi\left(\delta_N + \frac{1}{2}\right)} = T_{min-rev} \frac{1}{\left(\delta_N + \frac{1}{2}\right)} \quad (2.13b)$$

Thus, the relationship between these two fundamental building blocks of a complete Morse revival period is given by

$$\frac{T_{min-rev}}{T_{max-beat}} = \delta_N + \frac{1}{2} \quad (2.14a)$$

And based on the statements from Equation 2.8a and Equation 2.9, a perfect quantum revival period of the Morse oscillator T_{rev} is composed of integer numbers of the fundamental periods as following

$$T_{rev} = T_{min-rev}\mathbb{M} = T_{max-beat}\mathbb{N} \quad (2.14b)$$

As a direct result of above Equation 2.14a and Equation 2.14b, the ratio of those undetermined integer coefficients satisfy

$$\frac{\mathbb{N}}{\mathbb{M}} = \delta_N + \frac{1}{2} \quad (2.14c)$$

Therefore, in the approach of beat-period way, a perfect quantum revival time T_{rev} of the Morse oscillator can be expressed in terms of $T_{max-beat}$ and δ_N as following

$$T_{rev} = T_{max-beat}\mathbb{N} = T_{max-beat}Numerator[\delta_N + \frac{1}{2}] \quad (2.15a)$$

At the same time, in the approach of semiclassical-trajectory-profile way, T_{rev} can also be expressed in terms of $T_{min-rev}$ and δ_N as following

$$T_{rev} = T_{min-rev}\mathbb{M} = T_{min-rev}Denominator[\delta_N + \frac{1}{2}] \quad (2.15b)$$

Thus, either $T_{min-rev}$ or $T_{max-beat}$ can be served as the fundamental building block of T_{rev} . A useful dairy life analogy to this fact is that one product can be paid by two basic monetary units in the world market. If these two fundamental periods are symbolized by two basic monetary units: American dollar and Chinese yuan, as marked by the double-arrow in the bottom of Figure 2.2, then some immediate questions will be coming up, such as “When these two currencies are used in the quantum world, what will be the exchange rate between them?” For answering such interesting question, the consequent results and analysis of these two fundamental periods are discussed in the following section.

2.2 Fibonacci Sequence and Exchange Rate of $\frac{T_{min-REV}}{T_{max-beat}}$

The Morse complete revival period T_{rev} appears complex because of the anharmonicity of Morse oscillators. For a simple illustration without losing the generality, as shown in Figure 2.3 (a) through (c), the value of T_{rev} was increased step by step from the very beginning of the minimum revival period $T_{min-REV}$.

By keeping the same anharmonic frequency $w_\chi/2\pi c = 1(cm^{-1})$, the occurring one complete revival time of Morse oscillator with $w_e/2\pi c = 18(cm^{-1})$ as shown in Figure 2.3 (a) was exactly equal to the minimum revival period $T_{min-REV}$. Here, one complete revival period is $T_{rev} = T_{max-beat} = T_{min-REV}$, and the ratio of this minimum revival period to this maximum beat period was $T_{min-REV}/T_{max-beat} = 1/1$.

Meanwhile, as shown in Figure 2.3 (b), the appearing one complete revival time of Morse oscillator with $w_e/2\pi c = 17(cm^{-1})$ was exactly twice as longer as the minimum revival period $T_{min-REV}$. Here, one complete revival period is $T_{rev} = T_{max-beat} = 2T_{min-REV}$, and the ratio of this minimum revival period to this maximum beat period was $T_{min-REV}/T_{max-beat} = 1/2$. Interestingly, this appearing revival time $T_{rev} = 2T_{min-REV} = 2\pi/w_\chi$ is exactly equal to T_{approx} in the Equation 2.16. According to a semiclassical treatment for general anharmonic oscillators [26, 27, 28, 29], the complete revival time for Morse oscillator would be approximated by the following Equation 2.16 assuming large quantum numbers n close to their average \bar{n} .

$$T_{approx} = \frac{2\pi}{\frac{1}{2} \left| \frac{d^2 E_n}{dn^2} \right|_{n=\bar{n}}} = \frac{2\pi}{w_\chi} \quad (2.16)$$

Moreover, as shown in Figure 2.3 (c), the presenting one complete revival period of Morse oscillator with $w_e/2\pi c = 17 + \frac{1}{3}(cm^{-1})$ was exactly triple as longer as of the minimum revival period $T_{min-REV}$. Here, one complete revival period was $T_{rev} = 2T_{max-beat} = 3T_{min-REV}$, and the ratio of this minimum revival period to this maximum beat period was $T_{min-REV}/T_{max-beat} = 2/3$.

Remarkably, one complete revival period T_{rev} was composed of a whole integer number of the fundamental period $T_{min-REV}$ (or $T_{max-beat}$), and the ratio $T_{min-REV}/T_{max-beat}$ was able to form

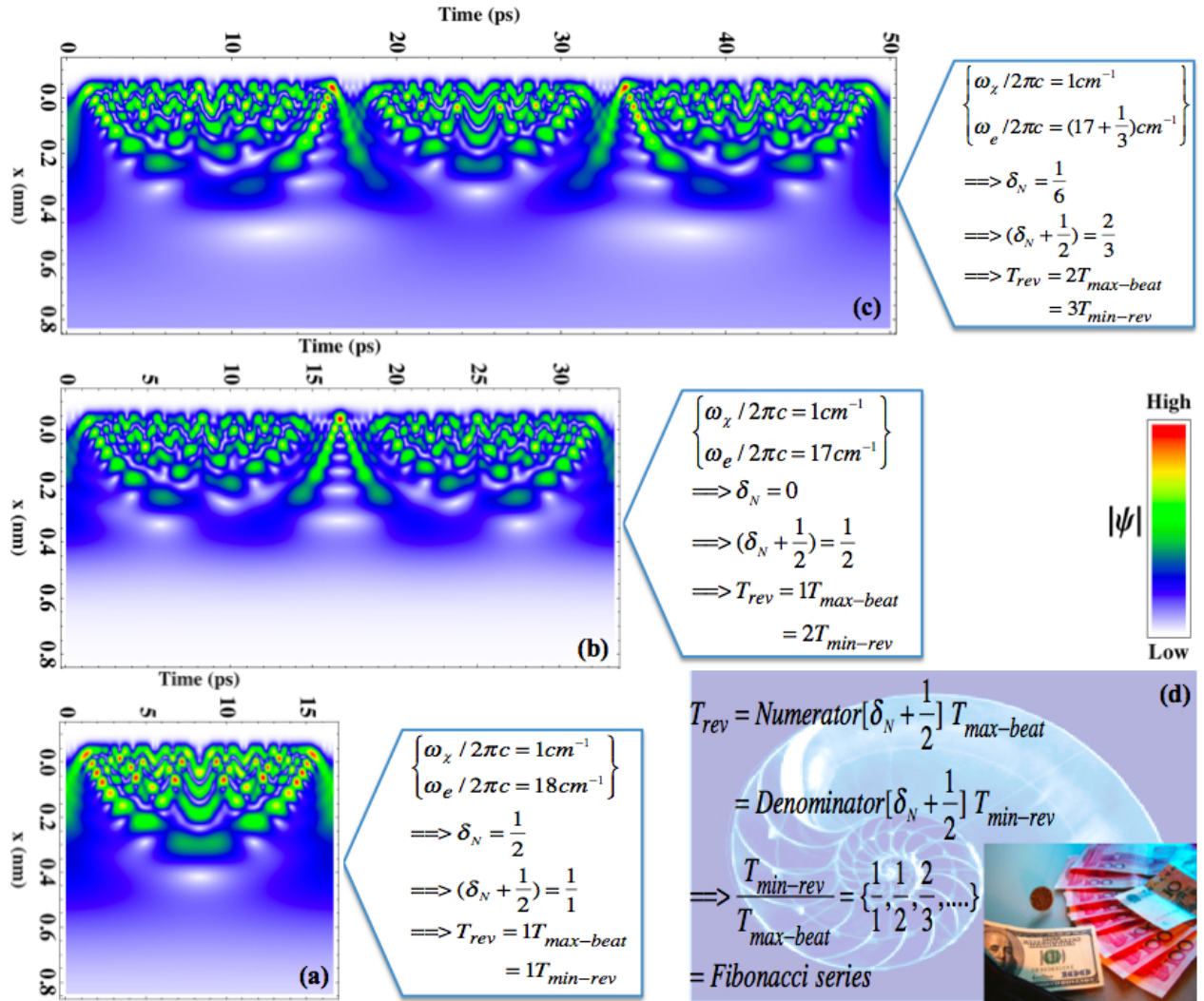


Figure 2.3: Fibonacci sequence and exchange rate. (a) When $\delta_N = 1/2$, the T_{rev} is composed of one $T_{max-beat}$ and one $T_{min-rev}$. (b) When $\delta_N = 0$, the T_{rev} is composed of $1T_{max-beat}$ and $2T_{min-rev}$. (c) When $\delta_N = 1/6$, the T_{rev} is composed of $2T_{max-beat}$ and $3T_{min-rev}$. (d) The ratio of $T_{min-rev}$ to $T_{max-beat}$ are forming the the Fibonacci sequence (symbolized by the spiral shell background). The inserted monetary picture symbolizes the ratio of $T_{min-rev}/T_{max-beat}$ as the exchange rate of currency.

the Fibonacci sequence $\{1/1, 1/2, 2/3, 3/5, 5/8, \dots\}$. In other word, the Fibonacci sequence is the subset of the ratio $T_{min-rev}/T_{max-beat}$. A useful analogy for describing the alternative ratio of $T_{min-rev}/T_{max-beat}$ in various revival periods is the currency exchange rate, such as exchange rate between U.S. dollar and Chinese yuan is varying with economic circles.

Furthermore, as shown in Figure 2.4 (a), the presenting one complete revival time of Morse oscillator with $w_e/2\pi c = 17.5(cm^{-1})$ is exactly four times of the minimum revival time $T_{min-rev}$. And in Figure 2.4 (b), the presenting one complete revival time of Morse oscillator with $w_e/2\pi c = 17.2(cm^{-1})$ is exactly five times of the minimum revival time $T_{min-rev}$. Therefore, it was indicated that any completely revival time T_{rev} of the Morse oscillators was made of the minimum revival time $T_{min-rev}$ integrally. This quantized period concept is a restatement of the Equation 2.15a and Equation 2.15b.

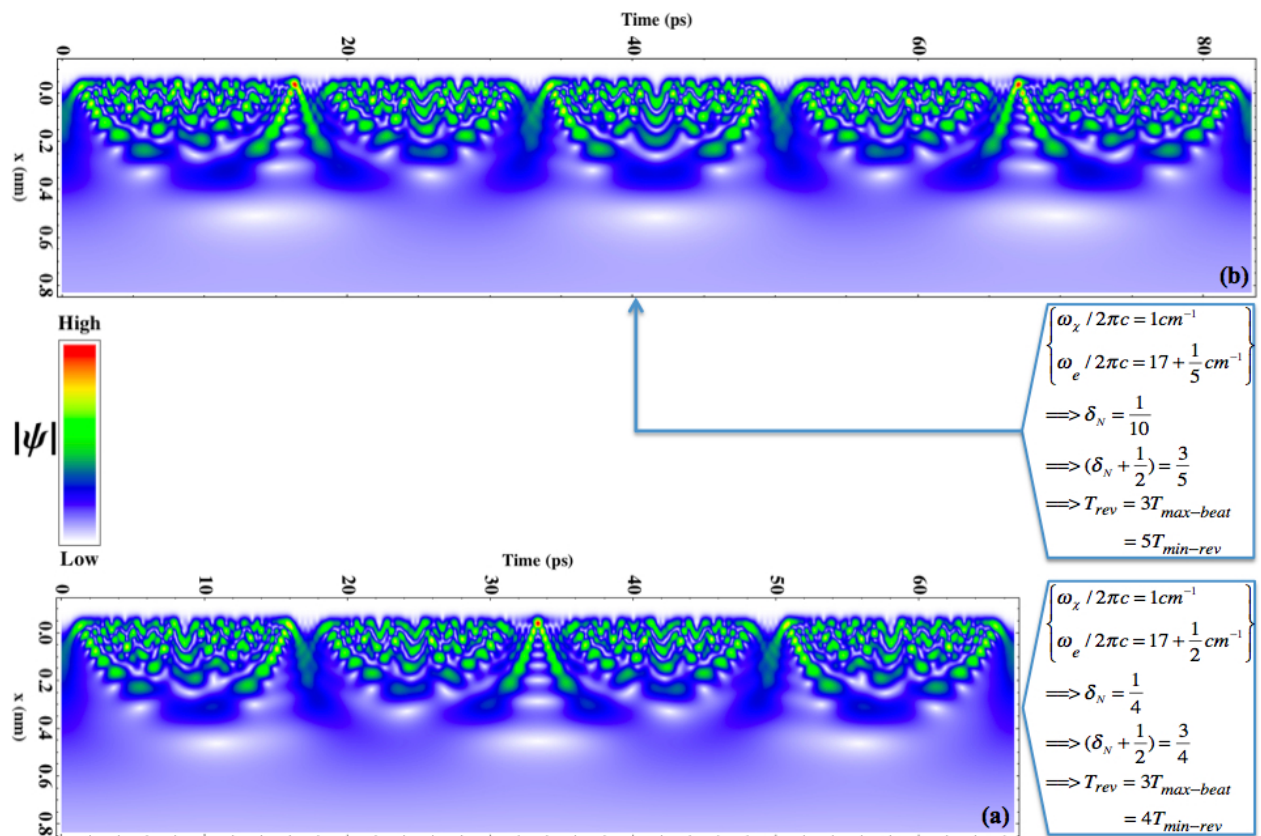


Figure 2.4: A complete revival time T_{rev} of the Morse oscillators is a quantized by fundamental period. (a) When $\delta_N = 1/4$, the T_{rev} is composed of $3T_{max-beat}$ and $4T_{min-rev}$. (b) When $\delta_N = 1/10$, the T_{rev} is composed of $3T_{max-beat}$ and $5T_{min-rev}$.

2.3 Farey Sequence and Ford Circles within a Perfect Minimum Revival Period

From previous section, a highly symmetric revival structure within a perfect minimum revival period ($T_{min-rev}/T_{max-beat} = 1$) was observed in Figure 2.3 (a). For analyzing such symmetric revival pattern in detail, a sample Morse oscillator potential with $\omega_e/2\pi c = 42(cm^{-1})$ and $\omega_x/2\pi c = 1(cm^{-1})$ was introduced. Then, according to Equation 2.12c for the maximum bound eigen states, a total of 21 bound eigenfunctions ($n_{max} = 20$) was allowed in this sample potential as illustrated in Figure 2.5. The superposition of these bound wave functions would form a probability-wave-packet ($\psi^*\psi$) oscillating in this potential well.

Importantly, according to Equation 2.15b for exact revival period, the complete revival period of this Morse wave packet was exactly equal to a minimum revival period: $T_{rev} = 1T_{min-rev} = 1T_{max-beat} = 1/(2c(cm)^{-1}) \approx 16.7(picosecond)$. For illustrating the symmetric beauty of such perfect minimum revival period (denoted as $T_{min-rev}/T_{max-beat} = 1$), the space-time maps composed of two complete revival periods were plotted in Figure 2.6 for comparison.

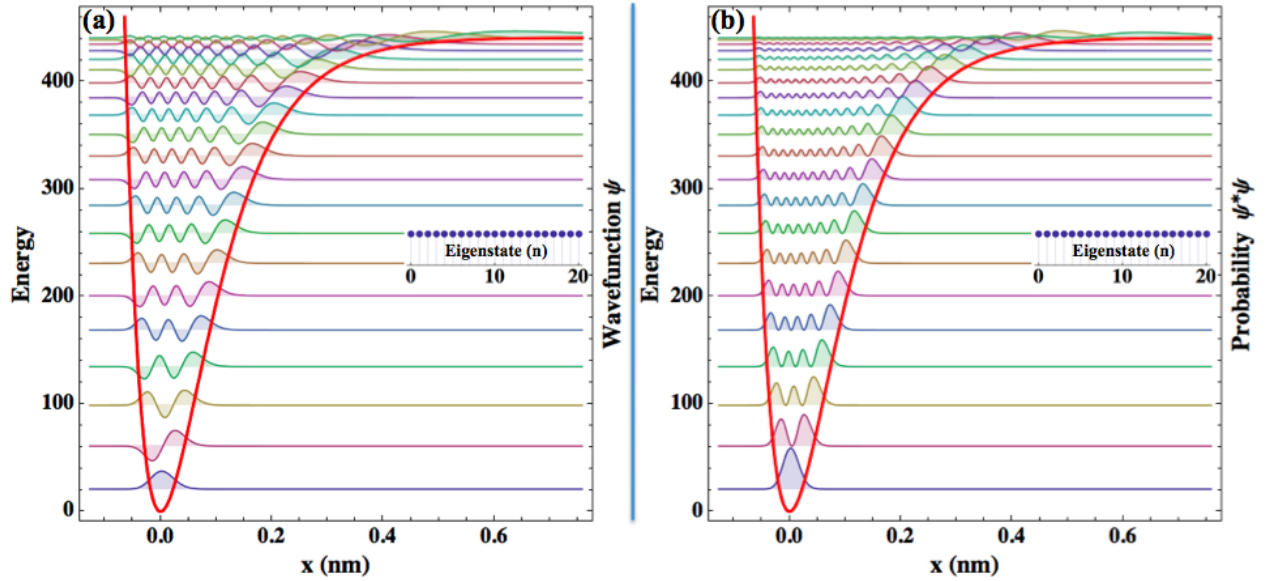


Figure 2.5: A sample Morse oscillator with harmonic frequency $\omega_e/2\pi c = 42(cm^{-1})$ and anharmonic frequency $\omega_x/2\pi c = 1(cm^{-1})$. (a) A total of 21 bound stationary states is listed along the corresponding energy level in the potential well (red-color-line), these wave functions are normalized (indicated by the same-height dotted-line). (b) The probability distributions of these stationary states are listed along the corresponding energy level in the potential well.

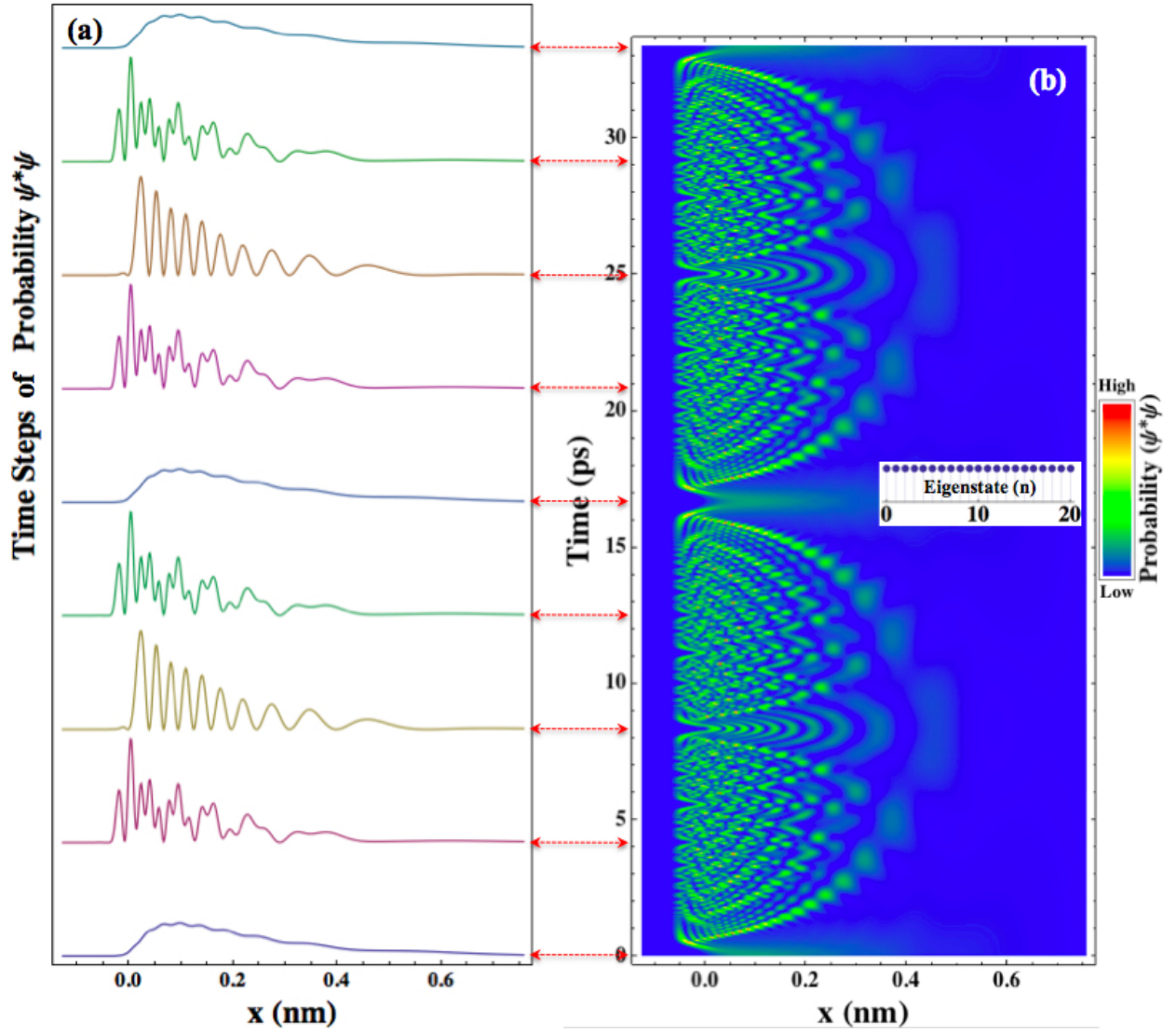


Figure 2.6: Space-time map in 2 complete revival periods. (a) The Morse wave packet composed of 21 bound states was propagated along the time-step. (b) The probability density map of the wave packet as a function of space and time. The double arrows connecting (a)-(b) indicate the corresponding time events.

2.3.1 Autocorrelation Function and Farey-sum Sequence

For finding the periodic footprints in this kind of dynamic quantum systems, an autocorrelation-function is often useful a sharp tool [27]. According to the time-evolution in Equation 2.6, an autocorrelation-function is expressed as Equation 2.17, where ω_n is the eigen-frequency.

$$A(t) = \sum_{n=0}^{n_{max}} e^{-i\frac{E_n t}{\hbar}} = \sum_{n=0}^{n_{max}} e^{-i\omega_n t} \quad (2.17)$$

Consider above dynamic wave packet in Figure 2.6 , the corresponding autocorrelation function was composed of 21 eigen-frequencies. As illustrated in Figure 2.7 (a), the norm $|A(t)| = \sqrt{A(t)^* A(t)}$ was plotted from $t = 0$ to $t = 1T_{rev}$. Meanwhile, as shown in Figure 2.7 (b), the norm of wave packet $|\psi| = \sqrt{\psi^* \psi}$ was plotted as a function of space and time. Here, the reason for plotting $|\psi| = \sqrt{\psi^* \psi}$ instead of the usual $|\psi|^2 = \psi^* \psi$ is due to the fact that the plot of $|\psi|$ is sharper than the plot of $|\psi|^2$, while both $|\psi|$ and $|\psi|^2$ contain the physical meaning of probability. For instance, the revival plot in Figure 2.7 (b) is sharper and clearer in comparison to the revival plot of Figure 2.6 (b), while both plots share the same essential information of wave packet dynamics.

By comparing these two plots in Figure 2.7 (a) and (b), a periodic correlation was clearly indicated. This closer examination of fractional revival in Figure 2.7 leads to a remarkable discovery that the quantum revival structure was nearly perfect match with the Farey-sum sequence $\{\frac{1}{2}, \frac{1}{3}, \frac{1}{4}, \frac{2}{7}, \frac{2}{5}, \frac{3}{7}\}$, as denoted by the vertical dashed lines in Figure 2.7 (a). In mathematic number theory, the Farey-sum-tree or Farey-sum sequence is the sequence of irreducible rational numbers between 0 and 1, the Farey sequence starts with the value 0/1, and ends with the value 1/1 [30]. The simple Farey-sum rule for adding fractions is illustrated in Figure 2.8 (a) .

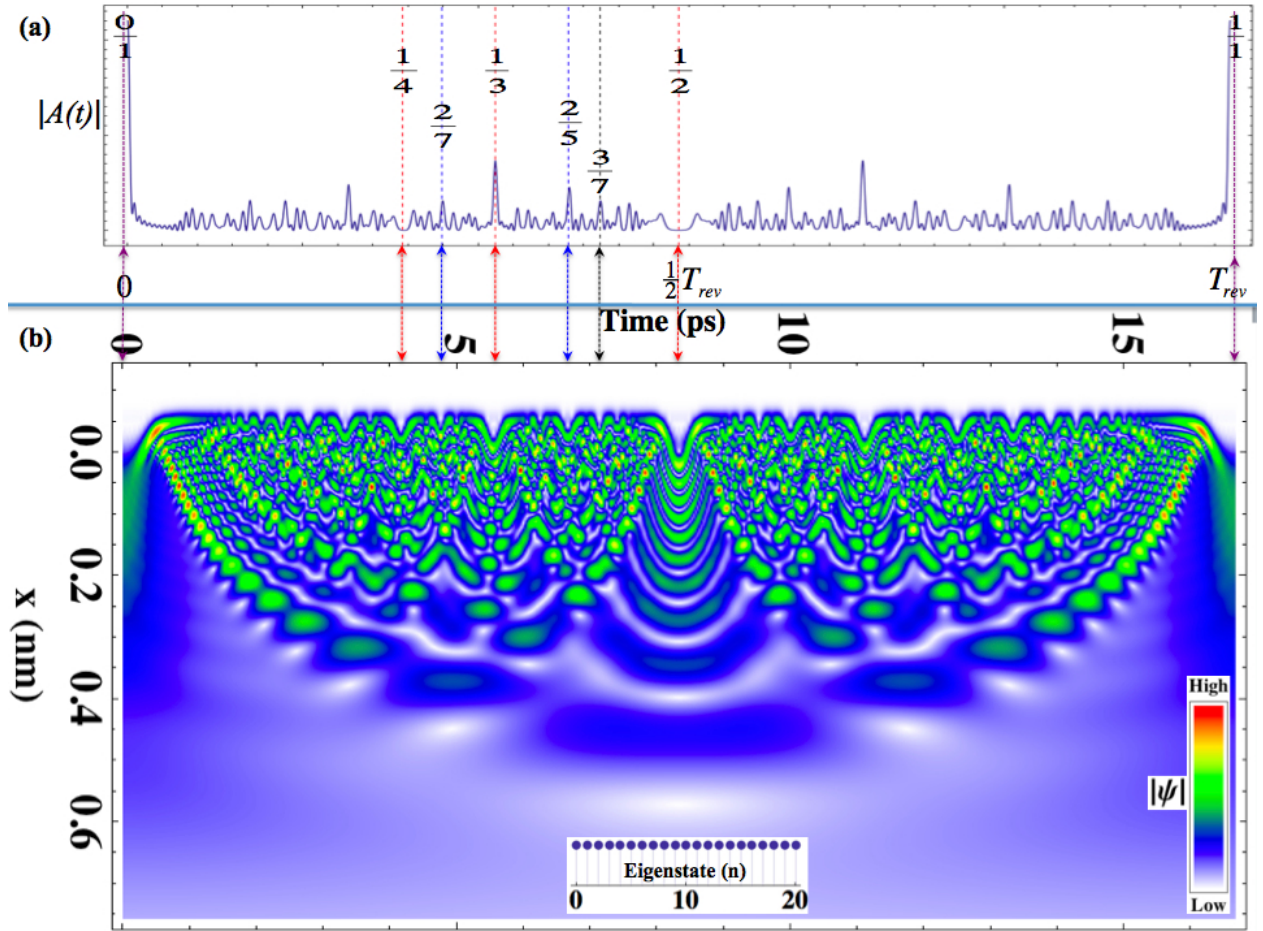


Figure 2.7: The Farey-sum sequence structure appearing in quantum dynamic pattern in the Morse oscillator with parameters $w_e/2\pi c = 42(cm^{-1})$ and $w_x/2\pi c = 1(cm^{-1})$. (a) The norm of auto-correlation function ($|A(t)|$ with $n_{max} = 20$) is plotted in one complete revival period T_{rev} whose fractions $\{\frac{1}{2}, \frac{1}{3}, \frac{1}{4}, \frac{2}{7}, \frac{2}{5}, \frac{3}{7}\}$ are denoted by the vertical dashed lines. (b) One complete revival period plot of the wave packet ($|\Psi(x, t)|$ with $n_{max} = 20$), the color denotes the probability density of the wave packet. The double dashed arrows connecting (a)-(b) indicate the corresponding time events.

2.3.2 Ford Circles Geometry for Quantum Revivals

There is an interesting connection between Farey-sum sequence and Ford circles [31]. For instance, a Farey-sum sequence of $\frac{1}{7}$ depth $\{\frac{0}{1}, \frac{1}{7}, \frac{1}{6}, \frac{1}{5}, \frac{1}{4}, \frac{2}{7}, \frac{1}{3}, \frac{2}{5}, \frac{3}{7}, \frac{1}{2}, \frac{4}{7}, \frac{3}{5}, \frac{2}{3}, \frac{5}{7}, \frac{3}{4}, \frac{4}{5}, \frac{6}{7}, \frac{1}{1}\}$ was displayed by a total of 19 mutually tangent circles in Figure 2.8 (b), and the fractional number was sitting inside of each circle. If the base line distance between two biggest circles $\{\frac{0}{1}, \frac{1}{1}\}$ is defined as one unit length, then the tangential position of each circle to the horizontal base line was a fraction of the unit length, which was marked by the red-arrow in Figure 2.8 (b-c). Thus, the fractional number inside of each circle was to denote its tangential position of the base line.

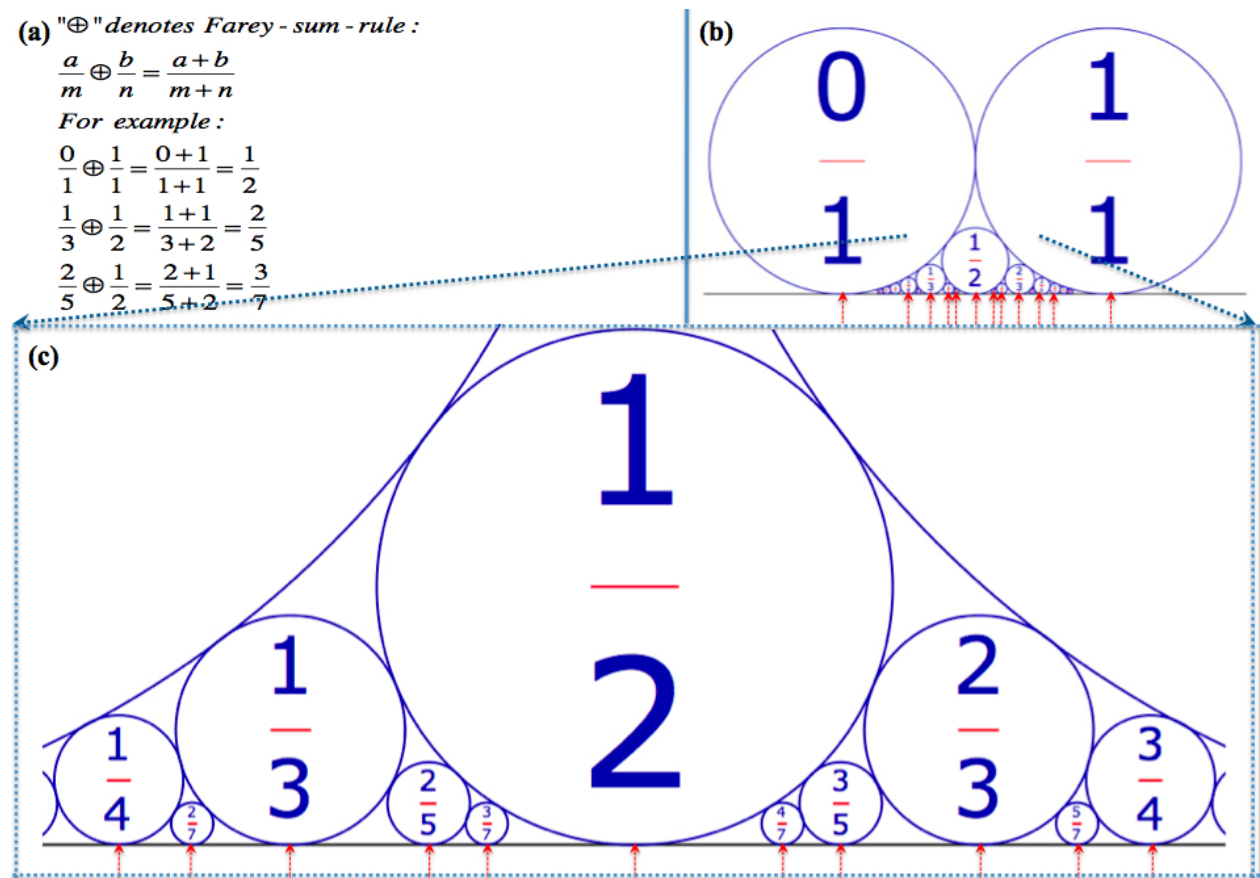


Figure 2.8: A simple relationship between Ford circles and Farey-sum sequence. (a) Some examples of the Farey-sum-rule for irreducible fractions. (b) Ford circles corresponding to Farey-sum sequence of $\frac{1}{7}$ depth $\{\frac{0}{1}, \frac{1}{7}, \frac{1}{6}, \frac{1}{5}, \frac{1}{4}, \frac{2}{7}, \frac{1}{3}, \frac{2}{5}, \frac{3}{7}, \frac{1}{2}, \frac{4}{7}, \frac{3}{5}, \frac{2}{3}, \frac{5}{7}, \frac{3}{4}, \frac{4}{5}, \frac{6}{7}, \frac{1}{1}\}$. (c) Ford circles of (a) are zoomed in to denote that each circle is tangential to the horizontal base line and its neighboring circles.

For building the Ford circles associating with Farey-sum sequence, consider a (x, y) area that

contains all rational fractions a/b each with a vector $\mathbf{V}_{\frac{a}{b}} = \begin{pmatrix} x = a \\ y = b \end{pmatrix}$. Vectors $\mathbf{V}_{\frac{0}{1}} = \begin{pmatrix} 0 \\ 1 \end{pmatrix}$ and $\mathbf{V}_{\frac{1}{1}} = \begin{pmatrix} 1 \\ 1 \end{pmatrix}$ for fractions $\frac{0}{1}$ and $\frac{1}{1}$ pointing from original point $(0, 0)$ of the x, y coordinate system. A remarkable fact discovered by Ford [31] is that each such $x = a/b$ point is a tangent point for one of an infinite number of mutually tangent circles hanging below the top-horizontal-line ($x = 1$) and each one of the circles having diameter $1/b^2$. The first such Ford-circle is the $b = 1$ case that is a single unit diameter circle cut in half to fill $\Delta x = 1$. The second case for $b = 2$ is drawn in Figure 2.9 that belongs to the vector sum of $\mathbf{V}_{\frac{0}{1}}$ and $\mathbf{V}_{\frac{1}{1}}$,

$$\mathbf{V}_{\frac{0}{1}} + \mathbf{V}_{\frac{1}{1}} = \begin{pmatrix} 0 \\ 1 \end{pmatrix} + \begin{pmatrix} 1 \\ 1 \end{pmatrix} = \begin{pmatrix} 1 \\ 2 \end{pmatrix} = \mathbf{V}_{\frac{1}{2}} \quad (2.18a)$$

Here its vector $\mathbf{V}_{\frac{1}{2}}$ points to a circle of diameter $1/2^2$ that is perfectly tangent to its “parent” unit Ford circles for fractions $\frac{0}{1}$ and $\frac{1}{1}$. Similarly, Figure 2.9 also shows a $b = 3$ vector $\mathbf{V}_{\frac{1}{3}}$ that is sum of $\mathbf{V}_{\frac{0}{1}}$ and $\mathbf{V}_{\frac{1}{2}}$ as following

$$\mathbf{V}_{\frac{0}{1}} + \mathbf{V}_{\frac{1}{2}} = \begin{pmatrix} 0 \\ 1 \end{pmatrix} + \begin{pmatrix} 1 \\ 2 \end{pmatrix} = \begin{pmatrix} 1 \\ 3 \end{pmatrix} = \mathbf{V}_{\frac{1}{3}} \quad (2.18b)$$

This kind of vector sum is named a Farey-sum after geologist John Farey [30] who used it to compute tidal beats. Continuing on these sums between vectors gave rise a series of shrinking circles belonging to vectors $\{\mathbf{V}_{\frac{1}{4}}, \mathbf{V}_{\frac{1}{5}}, \mathbf{V}_{\frac{1}{6}}, \mathbf{V}_{\frac{1}{7}}, \mathbf{V}_{\frac{2}{5}}, \dots, \mathbf{V}_{\frac{6}{7}}\}$. As illustrated in Figure 2.9, these circles sit in the area between their Farey “parents” circles $\mathbf{V}_{\frac{0}{1}}$ and $\mathbf{V}_{\frac{1}{1}}$.

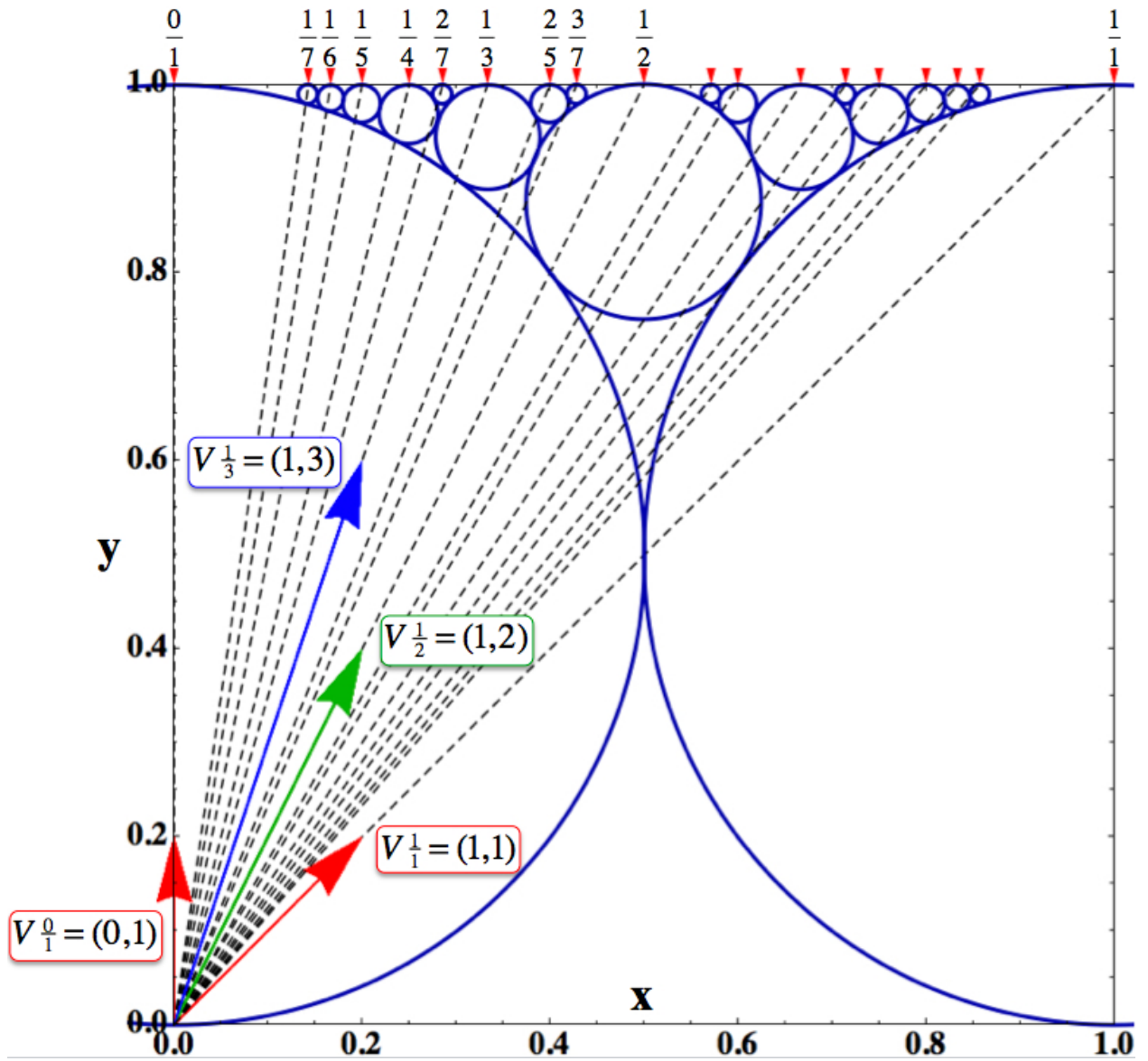


Figure 2.9: Building the Ford circles by vector associating with Farey-sum sequence

2.4 Conclusion of Morse Oscillator

In conclusion, the exact analytical wavefunctions of the Morse oscillator allowed an unprecedented detailed analysis of the rich and diverse behavior of the quantum dynamics. Based on the key parameter δ_N relating with the gap between the highest bound eigenstate and the dissociation energy, a concise way for searching the exact revival time T_{rev} of the Morse oscillator was given for the first time. The applications of two fundamental periods $T_{max-beat}$ and $T_{min-rev}$ allowed the discovery of the relationship between Fibonacci sequence and the Morse complete revival time. The applications of two fundamental periods $T_{max-beat}$ and $T_{min-rev}$ allows the discovery of the relationship between Fibonacci sequence and the Morse complete revival time. Particularly, the minimum period $T_{min-rev}$ suggested a quantized period concept that the complete period is made of integer numbers of the fundamental period in the quantum world of the Morse oscillator. A closer examination leads to a discovery that the quantum resonance and revival structure had a curious connection with the Farey-sum structure, which was illustrated with the classical Ford circles. This Fibonacci-Farey-Ford geometry should provide a further step towards a systematic understanding of the quantum wave packet dynamics, and such a quantum dynamic system may eventually lead to applications for quantum information processing and computing.

Chapter 3

Double-Morse Oscillator

From the study of previous chapter, it was clear that when Morse oscillators are considered as isolated regions, their revival patterns were in perfect symmetry of Farey-sum structure, as shown in Figure 3.1. But, when two Morse oscillators are in contact, a double-well potential is formed. A remarkable feature of a double-well or bistable-well is that quantum tunneling occurs within the barrier of two oscillators, and unique quantum dynamics are expected to occur in the double-well potential.

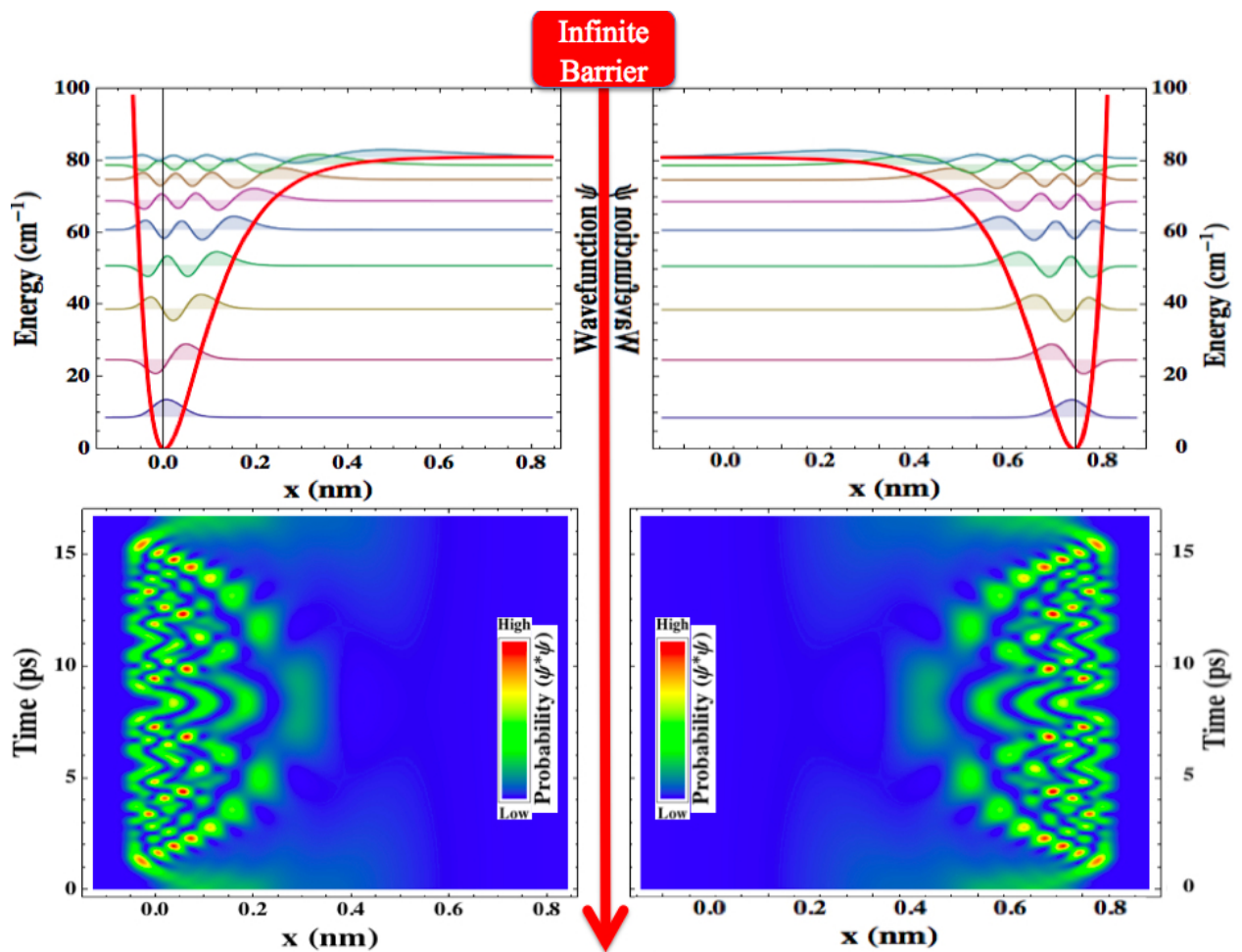


Figure 3.1: Two Morse oscillators with reflective symmetry are sitting on both sides, and isolated by infinite barrier (indicated by the thick-red-arrow). Their revival patterns are in perfect symmetry when both of them are living in their isolated kingdoms.

However, completely analytical solutions of double-well potentials are very rare. For instance, the double-square-well potential provides an analytical solution but its allowed eigenvalues are determined implicitly by solving a transcendental equation. A few of partially analytical (quasi-exactly solvable) double-well potentials are available in the literature, including sextic double-well potential, ϕ^4 potential, and the Razavy bistable potential. Furthermore, a striking feature of quantum tunneling in double wells is the extremely sensitivity to perturbations, which makes numerical techniques and approximation methods very difficult and requires a very careful control of the asymptotic behavior of tails of wave functions. This is one reason why a new method to determine exact solutions of double wells is desired and valuable.

It is worthwhile to introduce a partially analytical double-well potential from Caticha [32, 33]. Even though, only the ground state and first excited state are known analytically in this potential, the striking beating dynamics from two tunneling states is clearly observed in Figure 3.2 (d-f).

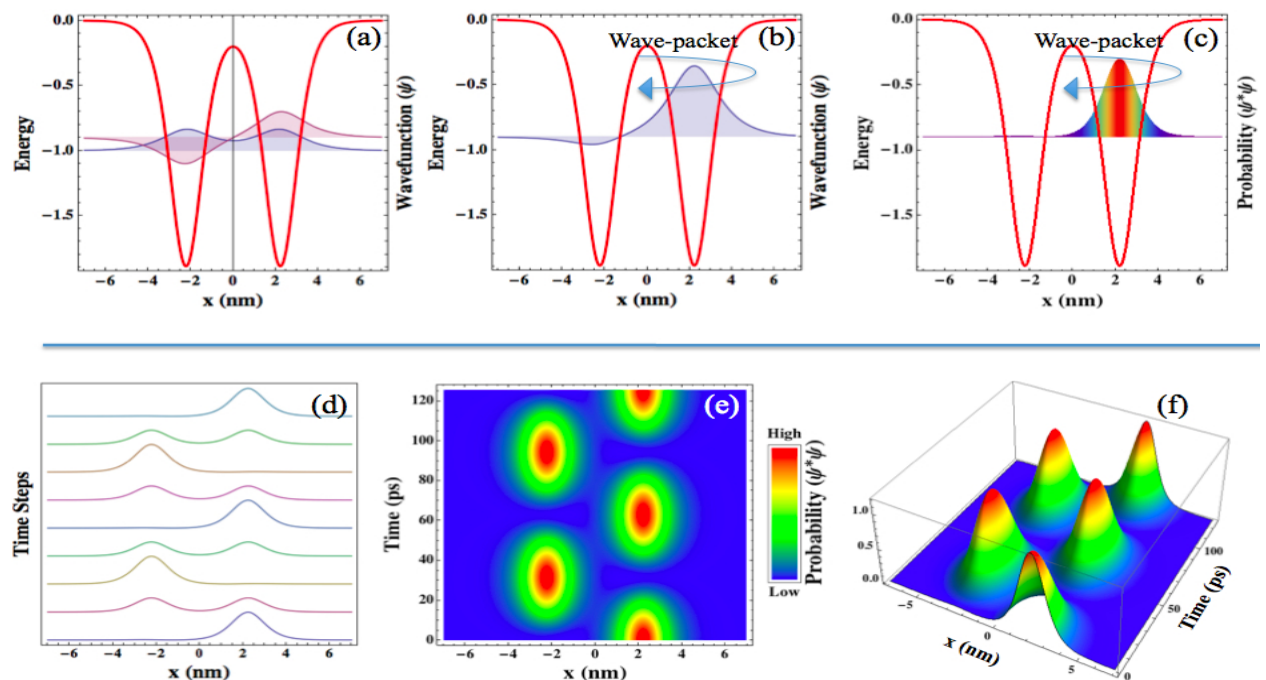


Figure 3.2: Quantum beating state in the Caticha double well potential. (a) The analytical ground state and the first excited state are listed along the corresponding energy level in the potential well (red-color-line). (b) The wavepacket is formed by the superposition of these eigenstates at $t = 0$. (c) The probability-wavepacket is formed by the superposition of these bound eigenstates at $t = 0$. (d) The wavepacket is propagated along the time-steps. (e) The probability density map of the wavepacket as a function of space and time. (f) 3D plot of the probability density map of (e).

3.1 A Genuine Double-Morse Potential

At first, according to the identity of hyperbolic function: $e^x = \cosh(x) + \sinh(x)$, the Morse potential in Equation 2.1 were expressed in terms of hyperbolic function:

$$V_M(x) = D(1 - e^{-\alpha x})^2 = D[1 - \cosh(-\alpha x) - \sinh(-\alpha x)]^2 \quad (3.1)$$

Then, a pair of Morse potentials equations were created by $\pm\alpha$ and $\pm x_0$:

$$V_{M+}(x) = D[1 - \cosh(-\alpha(x + x_0)) - \sinh(-\alpha(x + x_0))]^2 \quad (3.2a)$$

$$V_{M-}(x) = D[1 - \cosh(\alpha(x - x_0)) - \sinh(\alpha(x - x_0))]^2 \quad (3.2b)$$

These two Morse Potentials had a reflective symmetry as shown in Figure 3.3 (a). A simple sum of these two Morse potentials gave rise a genuine symmetric Double Morse Potential:

$$V_{MM}(x) = V_{M+}(x) + V_{M-}(x) + \text{constant} \quad (3.2c)$$

where the *constant* was for vertical translation of the Double Morse potential so that its minimum was the same as its parent potentials: $V_{MM}(x)|_{\text{minimum}} = V_{M+}(x)|_{\text{minimum}} = V_{M-}(x)|_{\text{minimum}} = 0$, as shown in Figure 3.3(b).

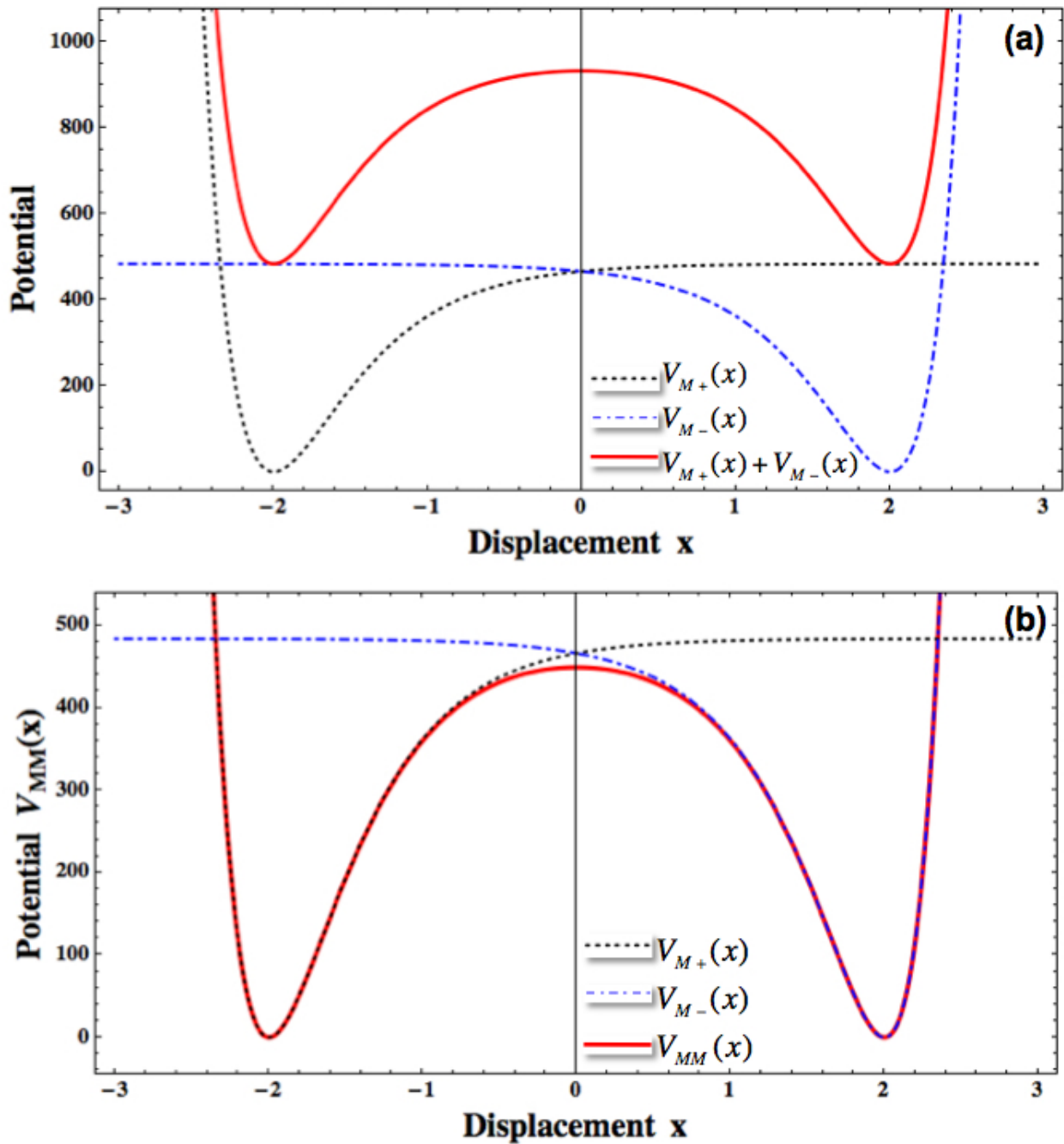


Figure 3.3: Building a genuine Double Morse Potential by a pair of Morse potentials. (a) $V_{M+}(x)$ potential sits on the left side as indicated by the black-dotted line, while $V_{M-}(x)$ potential sits on the right side as indicated by the blue-dashed line, a simple sum of these two potentials results a double-Morse potential $V_{M+}(x) + V_{M-}(x)$ as indicated by the red thick line. (b) Then, moves the red double-Morse potential down vertically by a *constant* of Equation 3.2c so that its minimum is the same as its parent potentials.

3.1.1 High Fidelity between a Razavy Potential and a Specified Double-Morse potential

At the time of this research, there was no exact analytical eigenfunctions of the genuine symmetric double Morse potential in Equation 3.2c. However, there was a special type of hyperbolic double-well potential whose low-lying energy states was exactly solvable, and it is known as Razavy potential [34][35] as

$$V_R(x) = [\zeta \cosh(2x) - n]^2 \quad (3.3)$$

where n is a positive integer for the desired energy levels, and ζ is determined by the minimum potential condition. For instance, if the desired minimum of the Razavy potential is occurring at $(x = \pm x_0)$, such as

$$V_R(x_0) = [\zeta \cosh(2x_0) - n]^2 = 0 \quad (3.4a)$$

Then, the parameter ζ is specified as

$$\zeta = n \operatorname{sech}(2x_0) \quad (3.4b)$$

Thus, the Razavy potential can be expressed in a concrete form of (x_0, n)

$$V_R(x) = [n \operatorname{sech}(2x_0) \cosh(2x) - n]^2 = 0 \quad (3.4c)$$

Noteworthy, the lowest n energy levels of this quantum potential are exactly solvable, and their energy eigenvalues and eigenfunctions can be computed and expressed analytically in terms of a finite number of certain common functions [34][36][35]. In 1979, Razavy was the first to develop these exact energy levels of $(n = 1, 2, 3, 4)$ for studying a bistable potential [34]. After nearly two decades, in 1998, Habib became the first to extend these exact energy levels up to $(n = 5, 6)$ for studying statistical mechanics of double sinh-Gordon Kinks [36]. Since the exactly solvable eigenfunctions of a Razavy potential are all the low-lying eigenfunctions, a deeper double-well means more exactly solvable eigenfunctions can be found.

For instance, as illustrated in Figure 3.4, in a shallow Razavy potential, only four stationary wave functions ($n = 1, 2, 3, 4$) can be computed exactly, while in a deeper Razavy potential, up to six stationary wave functions ($n = 1, 2, 3, 4, 5, 6$) can be computed exactly.

Using methods developed in this work, the exact energy levels were extended up to ($n = 21, 22$) in Razavy potential, and also a specified Double-Morse potential was developed to match a Razavy potential nearly perfectly.

To build up a best-fitting Double-Morse potential, its three parameters (α, x_0, D) were specified with best-fit values step by step. The first key step was to set ($\alpha = 2$) so that the Double-Morse $V_{MM}(x)$ of Equation 3.2c was simplified and expressed in terms of $\cosh(2x)$ as

$$V_{MM}(x) = D[2 - 4e^{-2x_0}\cosh(2x) + 4e^{-4x_0}\cosh^2(2x) - 2e^{-4x_0}] + \text{constant} \quad (3.5a)$$

which was the best $V_{MM}(x)$ form one can get among various α value for a matching Razavy equation (because $\cosh(2x)$ is the main term of Razavy equation as shown in Equation 3.4c). Then, the second step was searching for the best-fit value of x_0 by assuming the minimum of both Double-Morse potential and Razavy potential were located at $x = \pm R_0$. This reasonable assumption $\{V_{MM}(\pm R_0) = \text{minimum}, V_R(\pm R_0) = \text{minimum}\}$ led x_0 to be determined by

$$x_0 = \text{arccosh}\left(\frac{-1 + 4\cosh^2(R_0)}{\sqrt{-8 + 16\cosh^2(R_0)}}\right) \quad (3.5b)$$

The last step was estimating the best-fit value of D by the condition that $V_{MM}(0) = V_R(0) = \text{local-maximum}$. This fitting condition led D to be determined by

$$D = \frac{n^2 e^{4x_0} \sinh^2(R_0) \text{sech}^2(2R_0)}{4e^{x_0} \sinh(x_0) - 2\cosh(2R_0)} \quad (3.5c)$$

Based on above best-fit parameters searching scheme, a high fidelity match between the Razavy potential and a specified Double-Morse potential was determined.

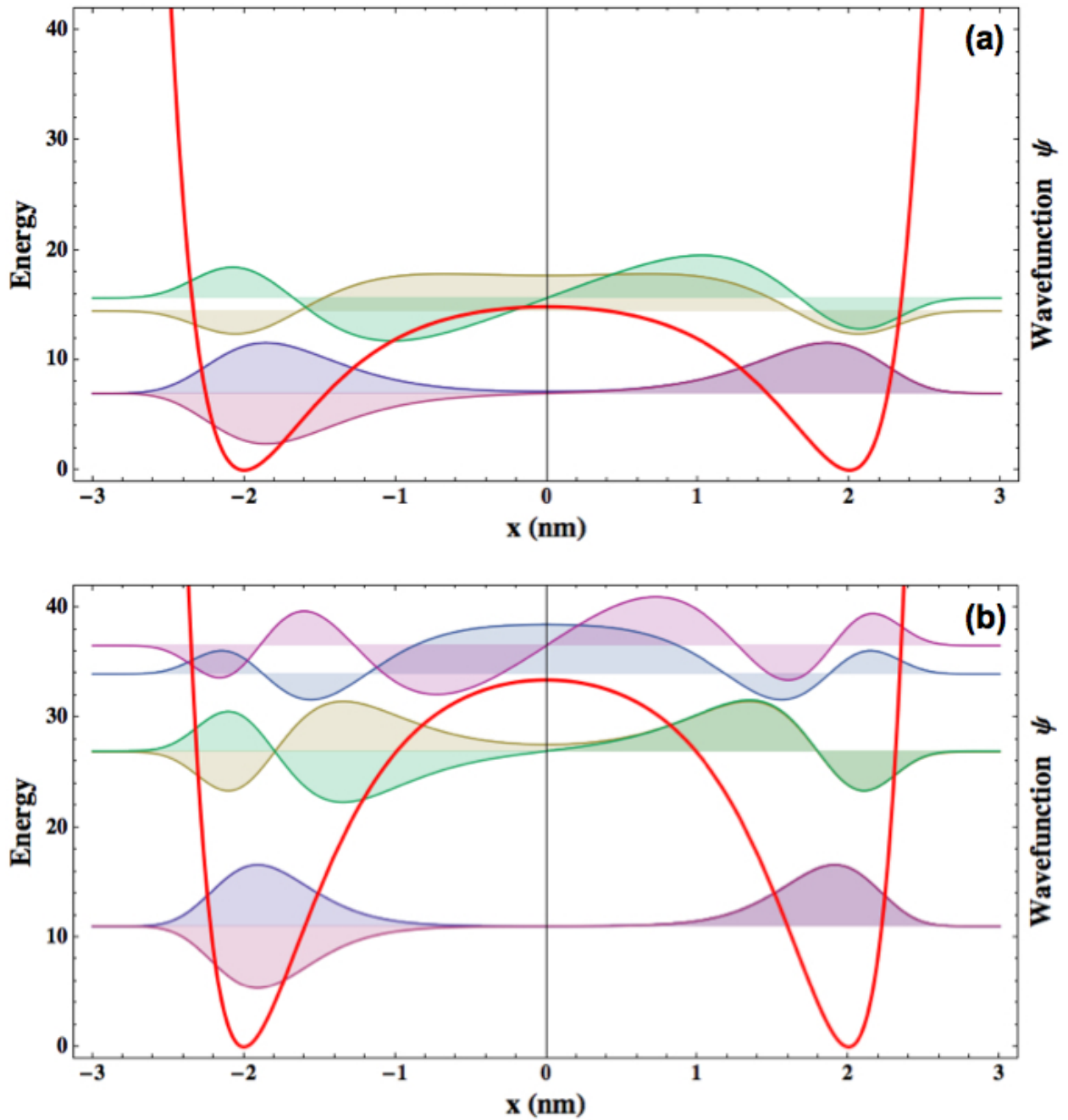


Figure 3.4: The exactly solvable eigenfunctions are relevant with the depth of double-well. (a) Up to four stationary wave functions ($n = 1, 2, 3, 4$) are exactly-computed in a shallow Razavy potential well (indicated by red-color-line), and listed along their energy levels. (b) Up to six stationary wave functions ($n = 1, 2, 3, 4, 5, 6$) are exactly-computed in a deeper Razavy potential well (indicated by red-color-line), and listed along their energy levels.

For a clear picture of the quality of their match or similarity, a close look at a deep Razavy potential with 22 exactly-computed eigenfunctions (which will be used frequently in the coming sections) was required for this research. For a Razavy potential of ($n = 22, R_0 = 2$), a best-fit Double-Morse potential was of parameter values ($\alpha = 2, x_0 = 2.000167, D = 484$) which were calculated by Equation 3.5a, Equation 3.5b and Equation 3.5c,

Algebraically, the tiny difference between a Razavy potential of ($n = 22, R_0 = 2$) and a Double-Morse potential of ($\alpha = 2, x_0 = 2.000167, D = 484$) was limited to a few parts per million, as indicated by the following underlines

$$V_R(x) = 484 - 35.44718568 \cosh(2x) + 0.649020130 \cosh^2(2x) \quad (3.6a)$$

$$V_{MM}(x) = 484 - 35.44718997 \cosh(2x) + 0.649020209 \cosh^2(2x) \quad (3.6b)$$

Graphically, the local-maximum in the middle of the double wells was zoomed in by 1000 times, but no difference was observed as shown in Figure 3.5 (b1). When the bottoms of the double wells were zoomed in by 1000 times, only ($\frac{0.0001}{500} = 0.2ppm$) potential-deviation was observed in Figure 3.5 (b2). Therefore, based on above graphical and algebraical analyses, the deviation between a Razavy potential and a genuine Double-Morse potential can be approached to a ppm (part per million) level in this case. Theoretically, the deviation between $V_{MM}(x)$ and $V_R(x)$ is subject to exponential decay when the distance ($2R_0$) between two bottoms of double-well is extended linearly. They are not exactly the same, but are similar enough for many applications. Hereinafter, a Razavy potential will refer to a specified Double-Morse potential with best-fit parameters.

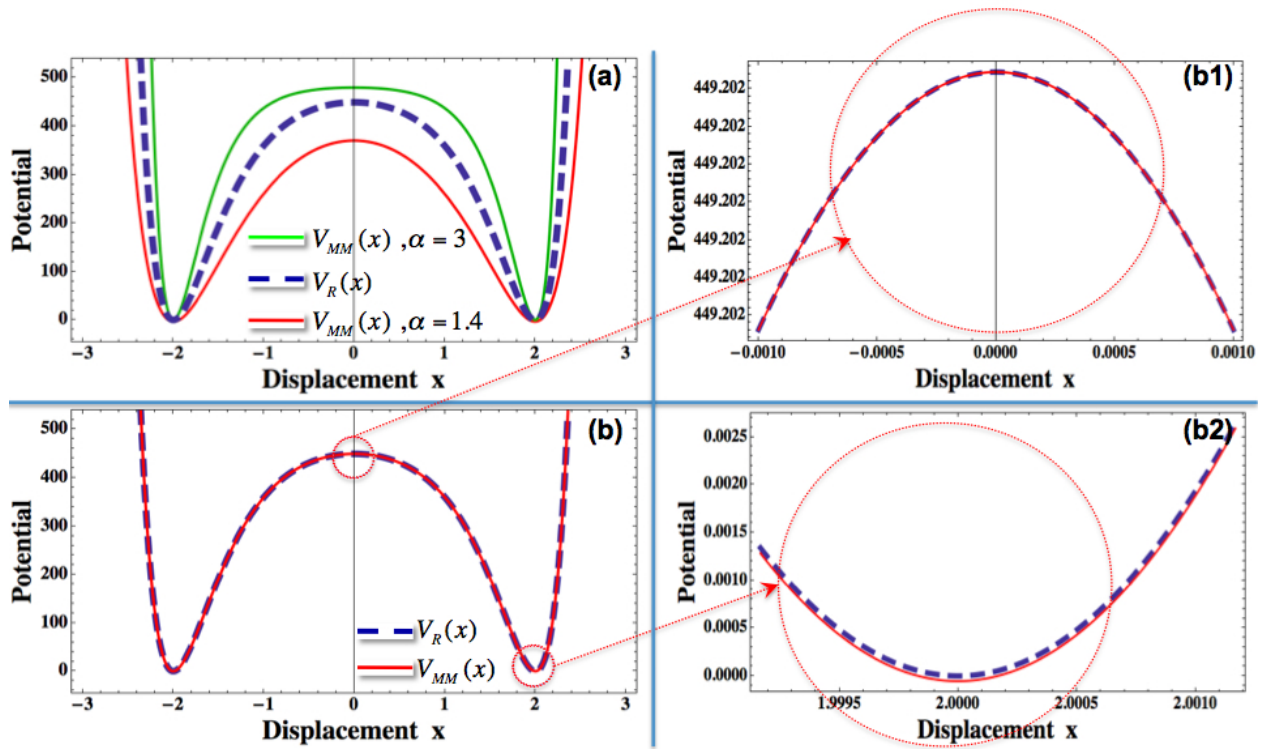


Figure 3.5: Graphically analysis on the deviation of a genuine Double-Morse-Potential from a Razavy potential. (a) A Razavy potential is sitting between two Double-Morse potentials with various α . (b) A good match between a Razavy potential of ($n = 22, R_0 = 2$) and a Double-Morse potential of ($\alpha = 2, x_0 = 2.000167, D = 484$). (b1) The tops in the middle of the double wells are zoomed in by 3 order of magnitude, no difference is observed. (b2) The bottoms of the double wells are zoomed in by 3 order of magnitude, only ($\frac{0.0001}{500} = 0.2 \text{ ppm}$) potential-deviation is observed in maximum.

3.1.2 Exact Eigenfunctions and Eigenvalues of a Deep Double-Morse Potential

In quantum mechanics, consider the one dimensional time-independent Schrodinger equation of potential $V_{MM}(x)$ and energy E

$$\frac{d^2}{dx^2}\phi(x) - \frac{2m}{\hbar^2}[V_{MM}(x) - E]\phi(x) = 0 \quad (3.7)$$

This partial differential equation is exactly solvable for certain energy levels, but not for all the energy spectrums. The solutions of $\phi(x)$ for n low-lying energy levels are exact and simply given in closed form as[34][36][35]

$$\phi_{even}(x) = e^{\frac{-n}{2} \operatorname{sech}(2x_0) \cosh(2x)} \sum_{j=0}^{(n-2)/2} C_{2j+1} \cosh((2j+1)x) \quad (3.8a)$$

$$\phi_{odd}(x) = e^{\frac{-n}{2} \operatorname{sech}(2x_0) \cosh(2x)} \sum_{j=0}^{(n-2)/2} S_{2j+1} \sinh((2j+1)x) \quad (3.8b)$$

where C_{2j+1} and S_{2j+1} are coefficients.

The above eigenfunctions of even and odd states are simple, however the challenge is how to obtain the values of C_{2j+1} and S_{2j+1} efficiently. In this work, a matrix scheme was developed for getting the coefficients as quickly as possible. For a clear interpretation of this matrix scheme, the coefficient C_{2j+1} was taken as an example. The basic procedure was as follows.

Firstly, by substituting the polynomial form $\psi_{even}(x)$ into the Schrodinger Equation 3.7, the 2nd-order derivative of this equation gave rise a complex polynomial hyperbolic equation by

$$\begin{aligned} [-E + n^2 - 2(n-1)\zeta \cosh(2x)] \sum_{j=0}^{(n-2)/2} \cosh((2j+1)x) C_{2j+1} \\ - \sum_{j=0}^{(n-2)/2} (2j+1)^2 \cosh((2j+1)x) C_{2j+1} \\ + 2\zeta \sinh(2x) \sum_{j=0}^{(n-2)/2} (2j+1) \sinh((2j+1)x) C_{2j+1} = 0 \end{aligned} \quad (3.9a)$$

where parameter $\zeta = n \operatorname{sech}(2x_0)$.

Then it was important to expand the hyperbolic trigonometric functions of above Equation 3.9a into terms of hyperbolic function $\cosh(2x)$, so that this polynomial equation could be sorted by terms of $\cosh^j(2x)$, and expressed by a matrix form

$$\begin{pmatrix} \sum_{j=0}^{(n-2)/2} (a_{j0} + b_{j0}\zeta + c_{j0}\zeta^2 + d_{j0}E)C_{2j+1} \\ \vdots \\ \sum_{j=0}^{(n-2)/2} (a_{jk} + b_{jk}\zeta + c_{jk}\zeta^2 + d_{jk}E)C_{2j+1} \\ \vdots \\ \sum_{j=0}^{(n-2)/2} (a_{j\frac{n-2}{2}} + b_{j\frac{n-2}{2}}\zeta + c_{j\frac{n-2}{2}}\zeta^2 + d_{j\frac{n-2}{2}}E)C_{2j+1} \end{pmatrix}^{\mathbf{T}} \times \begin{pmatrix} \cosh^0(2x) \\ \vdots \\ \cosh^j(2x) \\ \vdots \\ \cosh^{\frac{(n-2)}{2}}(2x) \end{pmatrix} = 0 \quad (3.9b)$$

where $\{a_{jk}, b_{jk}, c_{jk}, d_{jk}\}$ were constants whose indexes $\{j, k\}$ were integers and ranged from 0 to $(n-2)/2$. The first column in this matrix was a collection of coefficients. For nontrivial solutions of C_{2j+1} , it was required that each element in the first column equal to zero

$$\sum_{j=0}^{(n-2)/2} (a_{jk} + b_{jk}\zeta + c_{jk}\zeta^2 + d_{jk}E)C_{2j+1} = 0 \quad (3.9c)$$

Thus, this coefficient column gave rise the recurrence relations which were expressed as a $\frac{n}{2} \times \frac{n}{2}$ matrix form as

$$\begin{pmatrix}
(a_{00} + b_{00}\zeta + c_{00}\zeta^2 + d_{00}E) & \dots & (a_{j0} + b_{j0}\zeta + c_{j0}\zeta^2 + d_{j0}E) & \dots \\
\vdots & \vdots & \vdots & \vdots \\
(a_{0j} + b_{0j}\zeta + c_{0j}\zeta^2 + d_{0j}E) & \dots & (a_{jj} + b_{jj}\zeta + c_{jj}\zeta^2 + d_{jj}E) & \dots \\
\vdots & \vdots & \vdots & \vdots \\
(a_{0\frac{n-2}{2}} + b_{0\frac{n-2}{2}}\zeta + c_{0\frac{n-2}{2}}\zeta^2 + d_{0\frac{n-2}{2}}E) & \dots & (a_{j\frac{n-2}{2}} + b_{j\frac{n-2}{2}}\zeta + c_{j\frac{n-2}{2}}\zeta^2 + d_{j\frac{n-2}{2}}E) & \dots
\end{pmatrix}
\times
\begin{pmatrix}
C_1 \\
\vdots \\
C_{2j+1} \\
\vdots \\
C_{(n-2)/2}
\end{pmatrix}
= 0
\tag{3.9d}$$

Here, the determinant of this square matrix gave rise to a $\frac{1}{2}n$ -degree polynomial equation of unknown E . Therefore, the roots of this polynomial equation were the eigenvalues of energy in even state $\psi_{even}(x)$. Finally, by substituting the known E into Equation 3.9c, the coefficients C_{2j+1} were given directly.

Therefore, by applying the above computing scheme, a total of 22 exactly-computed eigenfunctions and eigenvalues were obtained smoothly, as indicated in Figure 3.6. During the computation of the exact eigenvalues in such a deep double well, in order to gain sufficient precision the computation program had to do computations with 48-decimal-digit of precision, as shown in Figure 3.7.

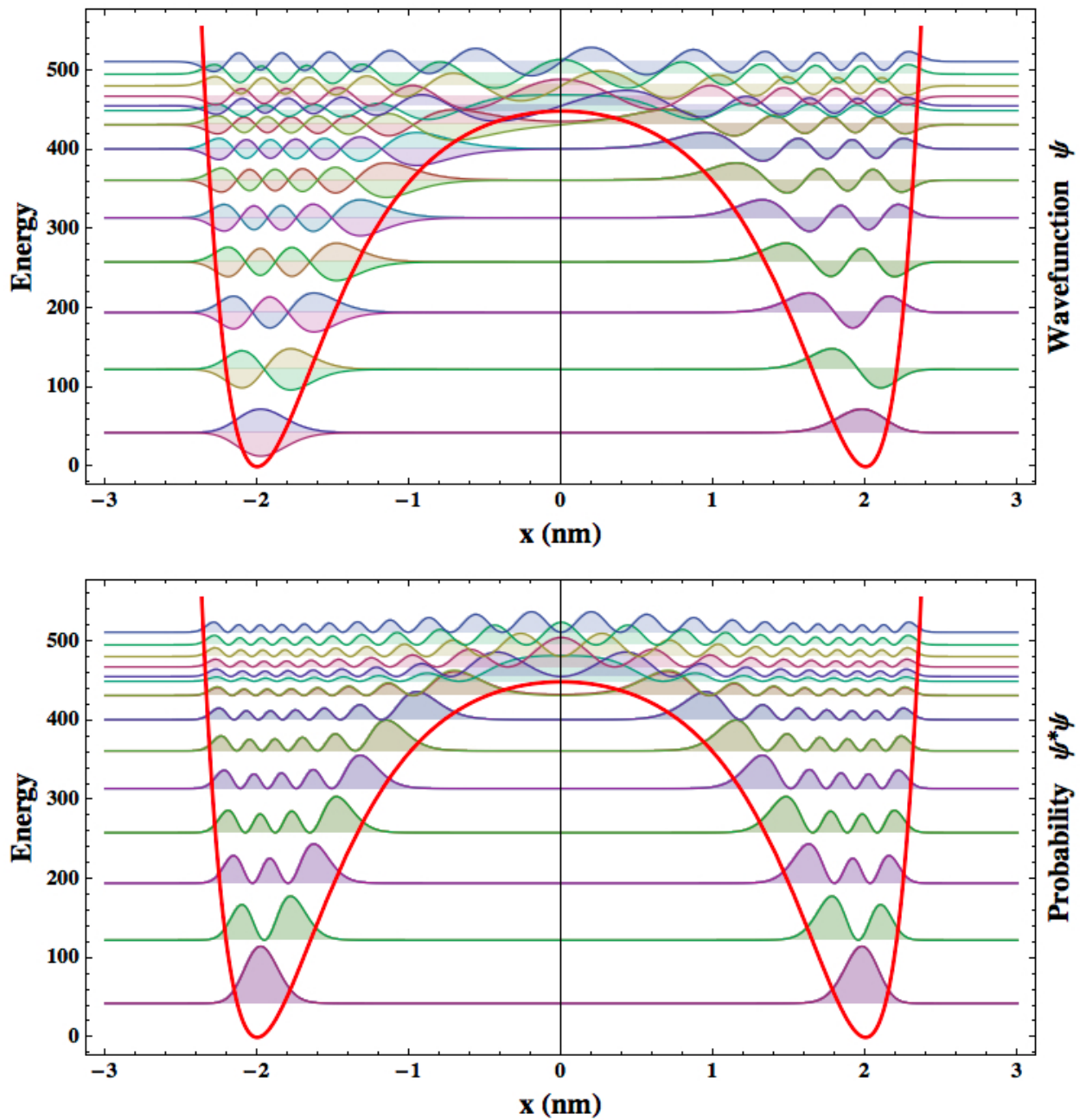


Figure 3.6: On the top plot, 22 exactly-computed eigenfunctions are listed along their eigenvalues of energy. On the bottom plot, the corresponding probability distribution functions $\psi^*\psi$ are listed along energy level. The energy level splitting due to quantum tunneling are too small to distinguished.

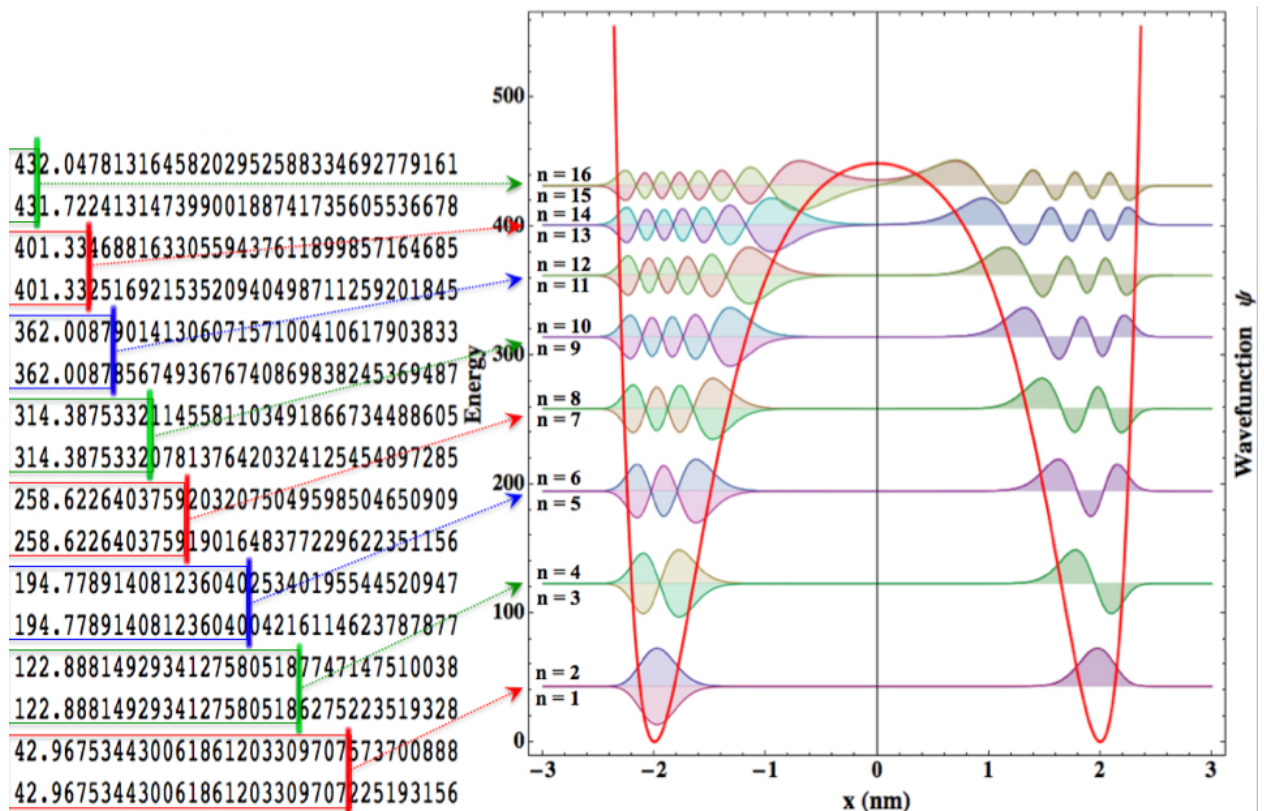


Figure 3.7: A total of 8 pairs wave-functions of energy-level-splitting due to quantum tunneling is listed on the right-hand side, while the corresponding energy values are listed on the left-hand side. The energy splitting of the fundamental level ($n = 1, 2$) is extremely small that their significant figures are going down to at least 24 digits after decimal point.

3.2 Resonant beats and Revivals from Tunneling States

In case of the wave packet composed of 16 tunneling states as shown in above Figure 3.7, billion years of evolution of the wave packet was required to plot for investigating the whole picture of revivals. As shown in Figure 3.8 (b), the resonant beating and revival structure of the Double-Morse oscillator was very complex, and no complete revival was observed in spite of such long propagating time ($t = 10^{25}ps$). Remarkably, the revival structure in Figure 3.8 (c) was similar with the revival of single Morse oscillator. The unusual phenomenon could be easily understood by observing the initial eigenstates ($t = 0$) shown in Figure 3.7 or Figure 3.8 (a): the eigenfunctions in the left-hand-side well were out of phase so that they cancelled each other, while the eigenfunctions in the right-hand-side well were in phase so that they enhanced each other.

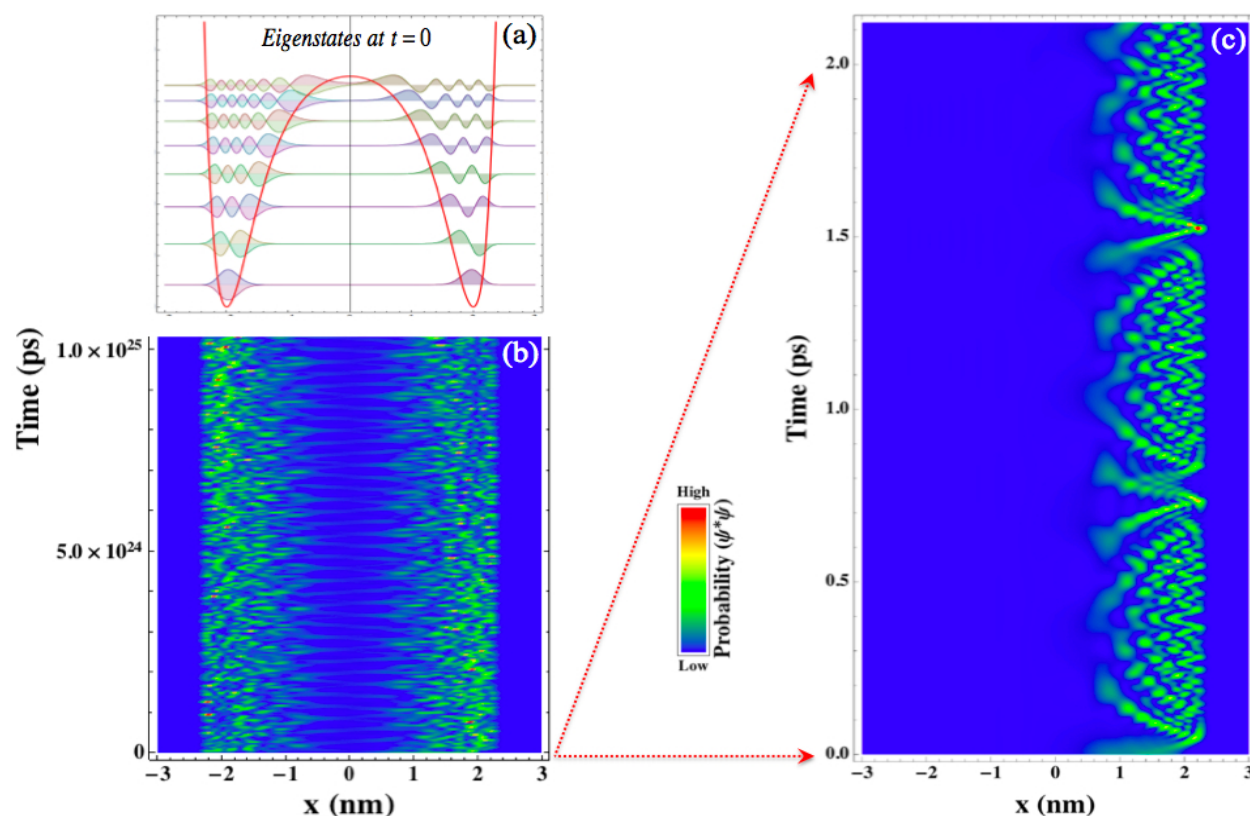


Figure 3.8: Resonant beats and revivals in the Double-Morse well. (a) A total of 8 pairs wavefunctions of energy-level-splitting due to quantum tunneling is listed on the top of left-hand side. (b) The corresponding wave packet propagation of long time ($t = 10^{25}ps$) is plotted on the bottom of left-hand side. (c) The very beginning moment ($t = 2ps$) during a long time wave packet propagation is captured and plotted.

3.3 Tsunami-like Resonant Beats and Revivals from Non-tunneling States

In case of the wave packet composed of 6 non-tunneling states as shown in Figure 3.9, the evolution of the wave packet appeared special kinds of order. At the well regions, the wave packet propagation was of dashed-line shape along the time direction. Meanwhile, at the local top region, the wave packet was of random large-dotted shape along the time direction. A useful analogy for describing this kind of striking wave packet dynamics at the local top is the tsunami wave at a coastal beach. Further analysis of this remarkable dynamics is expected in the future work.

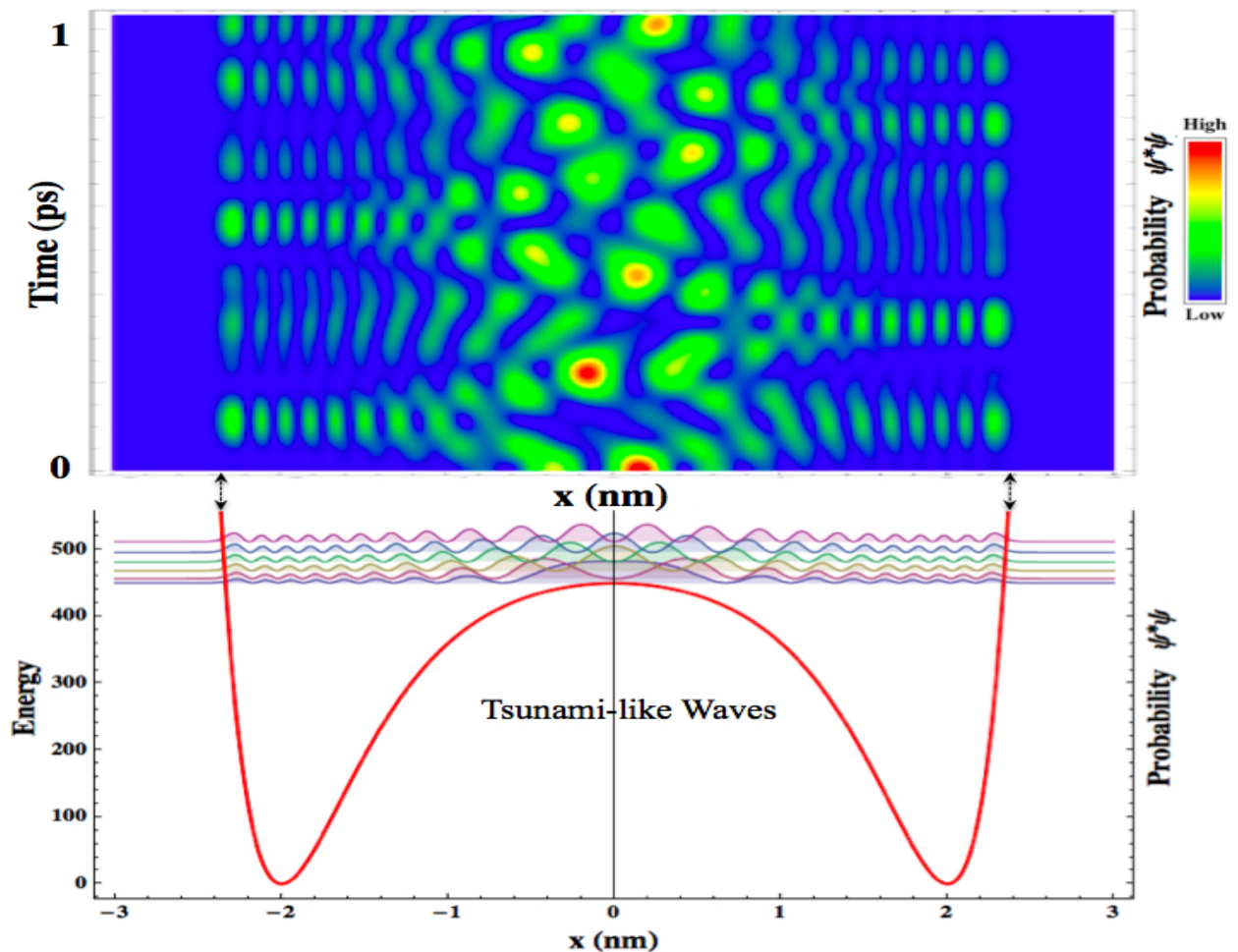


Figure 3.9: Tsunami-like waves at the local top (coastal beach) of a deep Double-Morse well. A total of 6 non-tunneling wave functions from the $n = 22$ deep Double-Morse well (indicated by red line) is listed on the bottom. On the top, the corresponding wave packet propagation is plotted as a function of time and space.

3.4 Conclusion of Double-Morse Oscillator

In conclusion, with a best-fit parameters scheme developed in this work, a specified double-Morse potential was developed to have a high fidelity solution of the quasi-solvable Razavy potential. Exact analytical eigenfunctions and eigenvalues up to $n = 22$ energy levels of the double-well potential were achieved for the first time. Through an efficient matrix scheme, detail of energy splitting analysis is available for the study of the rich and diverse behavior of quantum dynamics involving tunneling. A closer examination led to a discovery that the non-tunneling wave functions had a significant tsunami-like wave effect, which is relevant with the beach-like landscape at the local top in the double-well potential. This exact computed energy in a deep double-Morse potential is desired for many applications, because exact solutions of the unperturbed model will make the perturbation effect easy to handle in practical problems and provide a solid basis for stepping into the future study for quantum interference and entanglement.

Chapter 4

Quantum Rotor

The rotation of normal molecules are able to actively radiate far-infrared light or microwave. Conversely, modern infrared lasers or masers are the powerful tools used to rotate molecular motors. For instance, recently developed ultra-fast laser pulses have demonstrated impressive capability to spin up molecular rotors to extreme rotational states [37] [38]. The controllability of this new optical centrifuge for quantum scale rotors is extending the frontiers of science and technology. The quantum rotor described in this work is a quantum mechanical model for describing the rotational energy of molecular or atomic particles.

4.1 Symmetric Rigid Rotor

For the purposes of investigating basic rotational dynamics, the study scope of this chapter was focused on rigid quantum rotors in which vibrational and deformation were neglected. Then the corresponding Hamiltonian of quantum rotor was given simply as:

$$H = \frac{J_x^2}{2I_x} + \frac{J_y^2}{2I_y} + \frac{J_z^2}{2I_z} \quad (4.1)$$

where $\{I_x, I_y, I_z\}$ were the principal moments of inertia of the rotor body and $\{J_x, J_y, J_z\}$ were rotational angular momentum operators in a body-fixed frame. Due to the fact that the Hamiltonian of an asymmetric rotor ($I_x \neq I_y \neq I_z$) was not exactly solvable, and many conventional molecules are symmetric rotors which have two equal moments of inertia ($I_x = I_y$), such as CO_2 and NH_3 , the corresponding Hamiltonian in Equation 4.1 was further simplified as [39]:

$$\begin{aligned} H &= \frac{J_x^2}{2I_x} + \frac{J_y^2}{2I_x} + \frac{J_z^2}{2I_z} = \frac{J_x^2 + J_y^2 + J_z^2}{2I_x} - \frac{J_z^2}{2I_x} + \frac{J_z^2}{2I_z} \\ &= \frac{1}{2I_x} J \cdot J + \left(\frac{1}{2I_z} - \frac{1}{2I_x} \right) J_z^2 \end{aligned} \quad (4.2)$$

This indicated that the rotational eigen energy states could be simply described by $|j_{m_L, m_B}\rangle$,

where the quantized number j was given by the relationship: $J^2\Psi = \hbar^2 j(j+1)\Psi$, the quantized number m_L was given by the relationship in the Lab-frame: $J_z\Psi = \hbar m_L\Psi$, and the quantized number m_B was given by the relationship in the Body-frame: $J_z\Psi = \hbar m_B\Psi$. In a nut shell, $|^j_{m_L, m_B}\rangle$ was a simultaneous eigenfunction of $J \cdot J$ and J_z , and both the quantized z -component number m_L and m_B are in the range from $-j$ to $+j$ in quantized steps of integer one. Therefore, there were a total of $(2j+1)(2j+1)$ eigenfunctions for a symmetric rotor with given j -value. The energy value of each eigen energy states was given by

$$E(j, m_B) = \frac{\hbar^2}{2I_x} j(j+1) + \left(\frac{\hbar^2}{2I_z} - \frac{\hbar^2}{2I_x} \right) m_B^2 \quad (4.3)$$

4.1.1 Wigner-D Matrix — a Rotation Matrix for Any Spin

In quantum mechanics, an arbitrary rotation action of eigenfunction is described by a quantum rotation operator $\mathbf{R}(\alpha, \beta, \gamma)$, where three angles are defined as the Euler angles. The newly rotated wave function can be expressed under the angular momentum basis $\{j, m\}$ as:

$$|\Psi_r\rangle = \mathbf{R}(\alpha, \beta, \gamma) |^j_m\rangle = \sum_{m_r=-j}^{+j} |^j_{m_r}\rangle \langle^j_{m_r} | \mathbf{R}(\alpha, \beta, \gamma) |^j_m\rangle \quad (4.4)$$

The term $\langle^j_{m_r} | \mathbf{R}(\alpha, \beta, \gamma) |^j_m\rangle$ in this equation is the powerful Wigner-D matrix which was introduced in 1927 by Eugene Wigner [40]:

$$\mathbf{D}^j_{m_r, m}(\alpha, \beta, \gamma) \equiv \langle^j_{m_r} | \mathbf{R}(\alpha, \beta, \gamma) |^j_m\rangle \quad (4.5)$$

The Wigner-D matrix is the general rotation matrix for any spin system with a total angular momentum j . So the rotational transformation Equation 4.4 can be written as:

$$|\Psi_r\rangle = \mathbf{R}(\alpha, \beta, \gamma) |^j_m\rangle = \sum_{m_r=-j}^{+j} |^j_{m_r}\rangle \mathbf{D}^j_{m_r, m}(\alpha, \beta, \gamma) \quad (4.6)$$

The detail result of Wigner-D matrix for rotor is as the following:

$$\begin{aligned} D_{m_r, m}^j(\alpha, \beta, \gamma) &= e^{-i(m_r \alpha + m \gamma)} \sqrt{(j + m_r)! (j - m_r)!} \sqrt{(j + m)! (j - m)!} \\ &\times \sum_k \frac{(-1)^k (\cos \frac{\beta}{2})^{2j + m_r - m - 2k} (\sin \frac{\beta}{2})^{m - m_r + 2k}}{(j + m_r - k)! (j - m - k)! (m - m_r + k)! k!} \end{aligned} \quad (4.7)$$

where the k value is running over all values in which all factorials should be non negative.

For illustrating the dynamic feature of the elements in the Wigner-D matrix with various quantum number m_r and m , a value of $j = 10$ was chosen so that an array of $(2j + 1)^2 = 21 \times 21$ elements was plotted in each picture of Figure 4.1. Here, the value of each element equaled to the norm $|D_{m_r, m}^j(0, \beta, 0)|$ which was exactly the probability of transforming m to m_r . Moreover, the rotational feature of the Wigner-D matrix was vividly illustrated by the three sequential pictures of Figure 4.1.

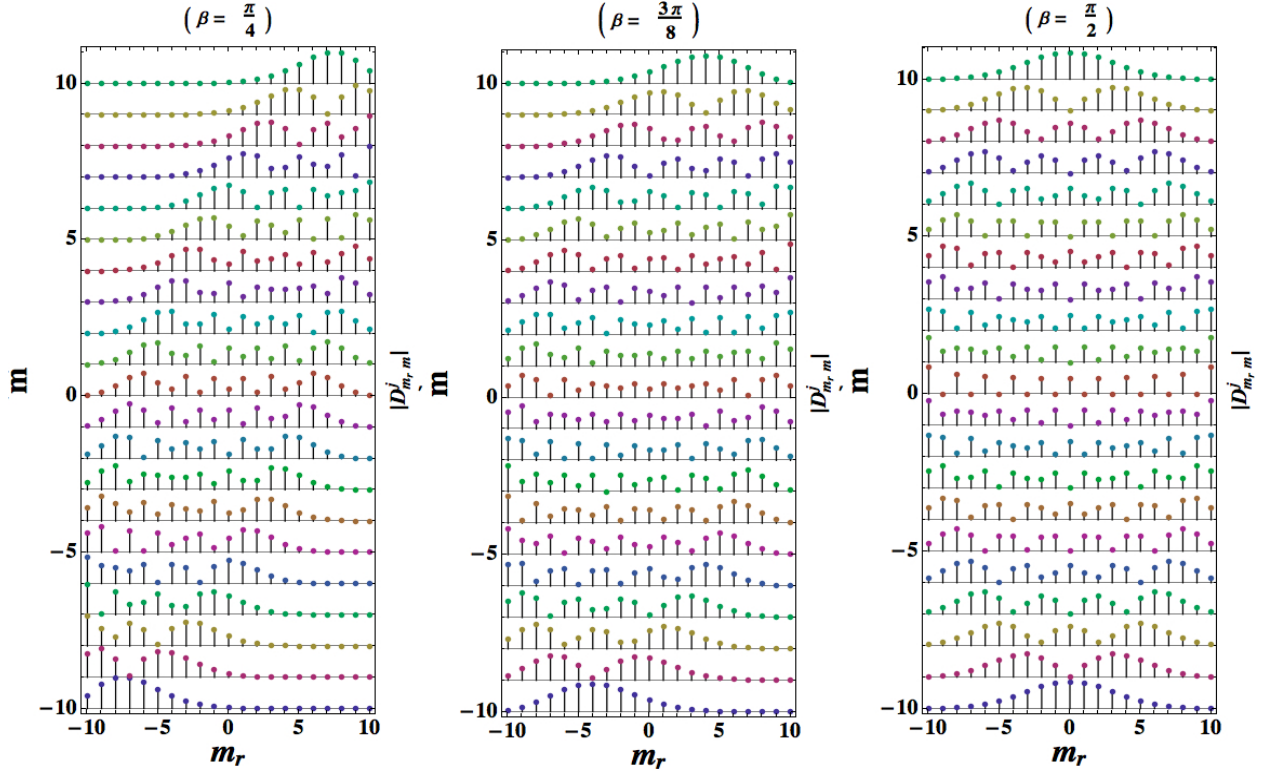


Figure 4.1: List-point-plottings of Wigner-D matrix with $j = 10$. A total of $(2j + 1) = 21$ lists is plotted, while each list contains a total of $(2j + 1) = 21$ points. The amplitude of each point is the value of the norm $|D_{m_r, m}^j(0, \beta, 0)|$ with corresponding quantum number m_r and m . The three pictures from left to right are corresponding to various angles: $\beta = \frac{2\pi}{8}, \frac{3\pi}{8}, \frac{4\pi}{8}$.

For a better observation of rotational dynamics of the Wigner-D matrix, a higher value of $j = 30$ was chosen, and a smooth density plotting method was applied as shown in Figure 4.2. As β rotated from $\frac{2\pi}{8}$ to $\frac{4\pi}{8}$, the density profiles in Figure 4.2 changed from an ellipse to a circle shape.

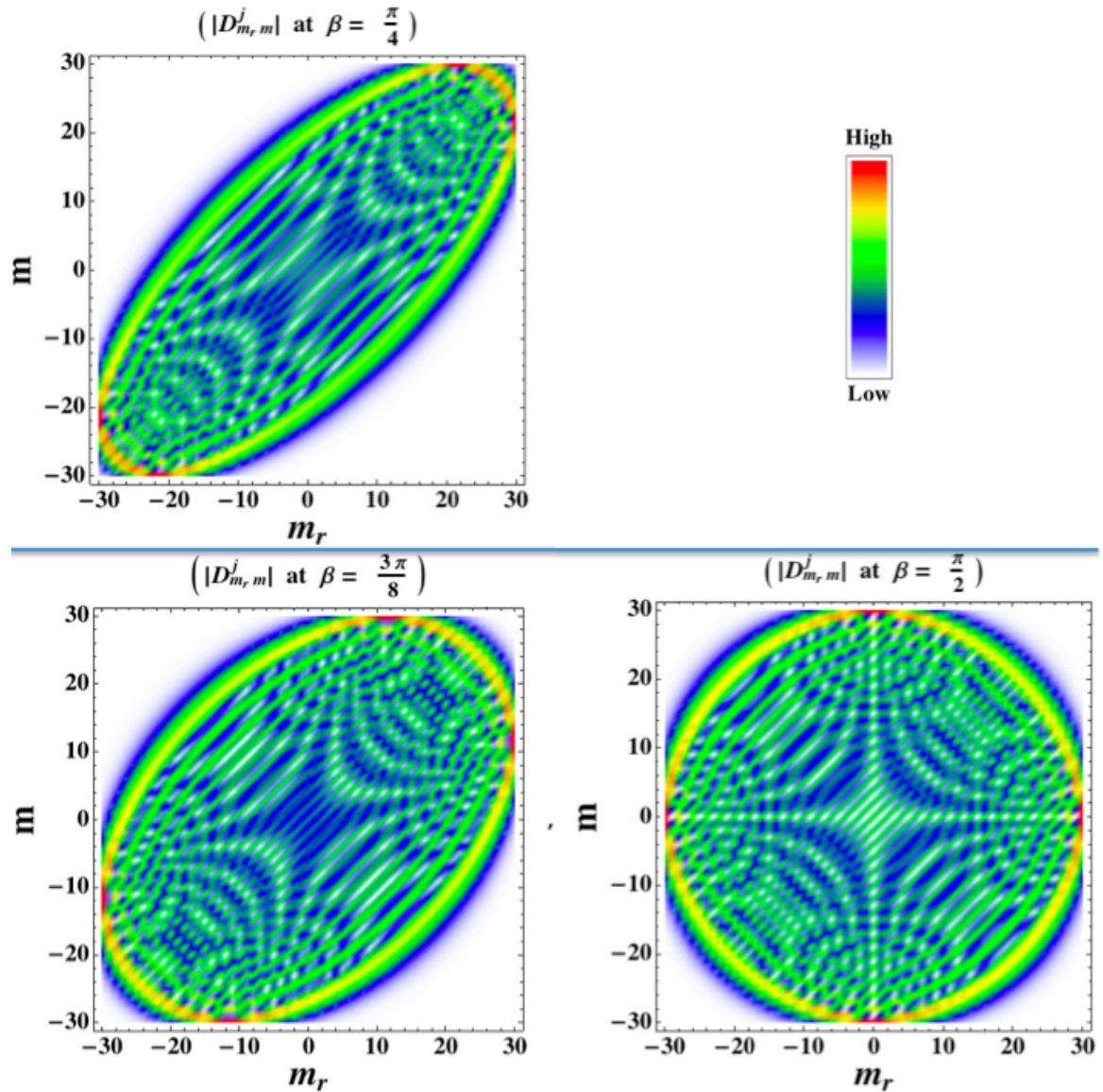


Figure 4.2: List-density-plotting of Wigner-D matrix with $j = 30$. A total of $(2j + 1) = 61$ lists is plotted, while each list contains a total of $(2j + 1) = 61$ points. The magnitude of each point is the value of the norm $|D_{m_r, m}^j(0, \beta, 0)|$ with corresponding quantum number m_r and m . The three pictures from left to right are corresponding to various angles: $\beta = \frac{2\pi}{8}, \frac{3\pi}{8}, \frac{4\pi}{8}$.

4.1.2 Quantum Rotor Wave Function

Due to the fact of quantum uncertainty, a quantum rotor is simultaneously precessing along two z -axes: one z -axis is of the lab frame and another z -axis is of its body frame. This means that a rotor in eigen energy state $|^j_{m_L, m_B}\rangle$ would be found in many different rotational position states $|\alpha, \beta, \gamma\rangle$, where α is the azimuth angle along lab- z -axis, β is the polar angle of body- z -axis, and γ is the azimuth angle along lab- z -axis. Therefore, in order to describe the quantum dynamics of rotor, it is necessary to know the probability of observing $|^j_{m_L, m_B}\rangle$ in the position state $|\alpha, \beta, \gamma\rangle$.

For building up the formula between $|^j_{m_L, m_B}\rangle$ and $|\alpha, \beta, \gamma\rangle$, an initial position state $|0, 0, 0\rangle$ ($|\alpha = 0, \beta = 0, \gamma = 0\rangle$) was considered, in which a rotor body frame was automatically lined up with the lab frame. During the coincident moment that the body frame and lab frame shared the same coordinates, the action of the projector operator $P^j_{m_L, m_B}$ projecting to this initial state $|0, 0, 0\rangle$ resulted in exactly an eigen energy state: $|^j_{m_L, m_B}\rangle = P^j_{m_L, m_B} |0, 0, 0\rangle$. Then the powerful Wigner-D matrix stepped in to act as a key role in formula formation, as shown in Equation 4.8:

$$\begin{aligned} |^j_{m_L, m_B}\rangle &= \frac{P^j_{m_L, m_B} |0, 0, 0\rangle}{\sqrt{2j+1}} = \frac{1}{N} \int d(\alpha, \beta, \gamma) \mathbf{D}^j_{m_L, m_B}^*(\alpha, \beta, \gamma) \mathbf{R}(\alpha, \beta, \gamma) |0, 0, 0\rangle \\ &= \frac{\sqrt{2j+1}}{8\pi^2} \int_0^{2\pi} d\alpha \int_0^\pi \sin\beta d\beta \int_0^{2\pi} d\gamma \mathbf{D}^j_{m_L, m_B}^*(\alpha, \beta, \gamma) |\alpha, \beta, \gamma\rangle \quad (4.8) \end{aligned}$$

where the term $D^j_{m_L, m_B}^*(\alpha, \beta, \gamma)$ was the complex conjugate of the Wigner-D matrix, and the rotational position state was $|\alpha, \beta, \gamma\rangle \equiv R(\alpha, \beta, \gamma) |0, 0, 0\rangle$. The amplitude $\sqrt{2j+1} D^j_{m_L, m_B}^*(\alpha, \beta, \gamma)$ are quantum eigenfunctions of a rigid rotor, and also known as Quantum Rotor Wave Function [41]

$$\begin{aligned} \psi_{rotor}(j, m_L, m_B, \alpha, \beta, \gamma) &= \langle \alpha, \beta, \gamma | ^j_{m_L, m_B} \rangle = \langle 0, 0, 0 | R^*(\alpha, \beta, \gamma) | ^j_{m_L, m_B} \rangle \\ &= \sqrt{2j+1} D^j_{m_L, m_B}^*(\alpha, \beta, \gamma) \quad (4.9) \end{aligned}$$

Its squared norm $|\psi_{rotor}|^2 = \psi_{rotor}^* \psi_{rotor}$ yielded the probability for an observation that a rigid rotor in a eigen energy state $|^j_{m_L, m_B}\rangle$ would be found in rotational position state $|\alpha, \beta, \gamma\rangle$ [41].

4.2 Resonances and Revivals in Quantum Rotor

The wave packet of Equation 4.10 is a superposition of $(2j + 1)$ stationary rotor waves of m_B values is in the range from $-j$ to $+j$

$$\begin{aligned}\Psi(j, m_L, \alpha, \beta, \gamma, t) &= \sum_{m_B=-j}^{+j} \psi_{rotor}(j, m_L, m_B, \alpha, \beta, \gamma) e^{-i\frac{E(j, m_B)}{\hbar}t} \\ &= \sqrt{2j + 1} \sum_{m_B=-j}^{+j} D_{m_L, m_B}^j(\alpha, \beta, \gamma) e^{-i\frac{E(j, m_B)}{\hbar}t}\end{aligned}\quad (4.10)$$

where the eigen energy $E(j, m_B)$ is given in Equation 4.3. Here, for studying the essential feature of quantum dynamics, the initial condition of $(\alpha = 0, \beta = \frac{\pi}{2})$ was applied in the whole chapter. In quantum mechanics, there are two kind of angular momentum j : orbital angular momentum $j_{orbital}$ and spin angular momentum j_{spin} . Orbital angular momentum is corresponding to the rotating trajectory of quantum object, such as electron orbits the nuclear axis. While spin angular momentum is an intrinsic quantum mechanical form of angular momentum observed in quantum object only, such as the intrinsic spin of electron is characterized by quantum number $\frac{1}{2}$. It is noteworthy that spin has no analog in classical mechanics. So that the total angular momentum ($j = j_{orbital} + j_{spin}$) in quantum rotor will be falling into two classes: integer spin system and half-integer spin system.

4.2.1 Integer Spin — Boson System

4.2.1.1 Spin $j = 3$

For illustrating the properties of integer-spin rotor waves, a simple $j = 3$ rotor was considered. In case of the list-plot of quantum rotor waves, as indicated in Figure 4.3, each $\psi = D_{3, m_B}^3(0, \frac{\pi}{2}, \gamma)$ was plotted as a function of angle γ in a range of 2π . For $j = 3$, a total of $(2j + 1) = 7$ different m_B values was used, so that there were 7 wave functions listed along m_B values in each list plotting graph. The three graphs from left to right corresponded to the real part of rotor wave $Re[\psi]$, the

imaginary part of the rotor wave $Im[\psi]$, and the probability of rotor position $\psi^*\psi$. At the same time, as indicated in Figure 4.4, the energy-value-based list-plot of quantum rotor waves with $\psi = D_{3,m_B}^3(0, \frac{\pi}{2}, \gamma)$ were plotted as a function of angle γ . A total of 7 wave functions was listed along their energy values in each list plotting graph (only 4 waves are observed because of energy degeneracy). The three graphs from left to right corresponded to the real part of rotor wave $Re[\psi]$, the imaginary part of rotor wave $Im[\psi]$, and the probability of rotor position $\psi^*\psi$.

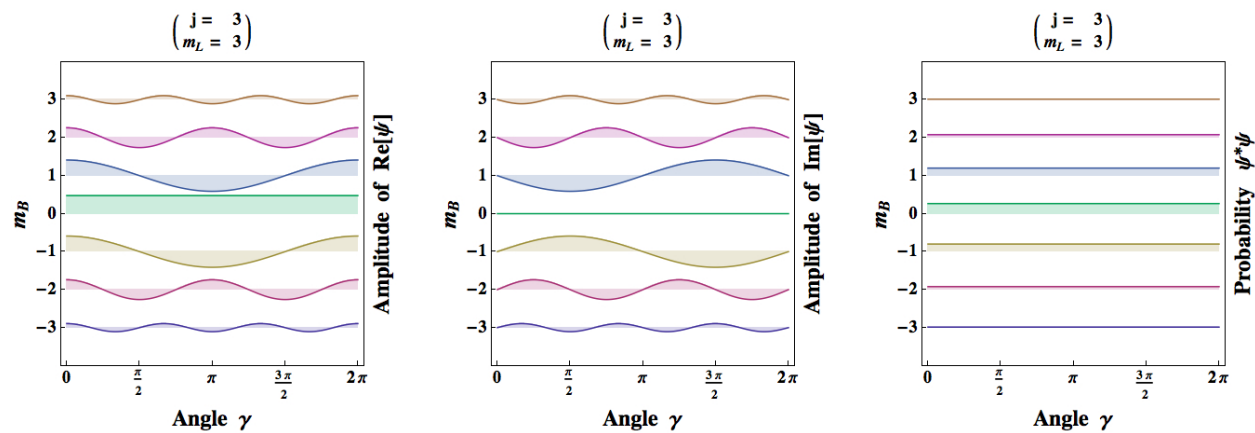


Figure 4.3: The m_B -value-based list-plot of quantum rotor waves that each $\psi = D_{3,m_B}^3(0, \frac{\pi}{2}, \gamma)$ is plotted as a function of angle γ . A total of 7 wave functions are listed along m_B values in each list plotting graph. The three graphs from left to right are corresponding to the real part of rotor wave $Re[\psi]$, the imaginary part of rotor wave $Im[\psi]$, and the probability of rotor position $\psi^*\psi$.

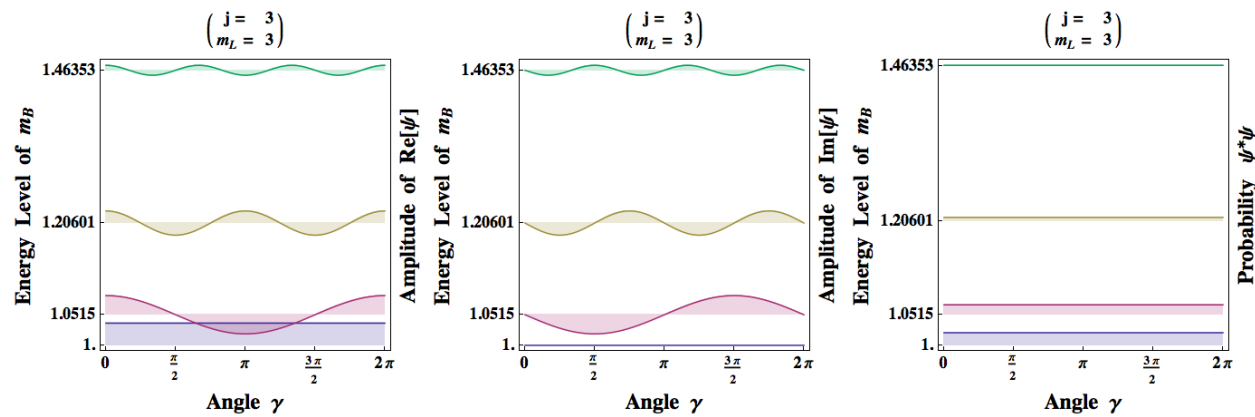


Figure 4.4: The energy-value-based list-plot of quantum rotor waves that each $\psi = D_{3,m_B}^3(0, \frac{\pi}{2}, \gamma)$ is plotted as a function of angle γ . A total of 7 wave functions are listed along their energy values in each list plotting graph (only 4 waves are observed because of energy degeneracy). The three graphs from left to right are corresponding to the real part of rotor wave $Re[\psi]$, the imaginary part of rotor wave $Im[\psi]$, and the probability of rotor position $\psi^*\psi$.

In case of the polar plot of quantum rotor waves, as indicated in Figure 4.5, each $\psi = D_{3,m_B}^3(0, \frac{\pi}{2}, \gamma)$ was plotted as a function of angle γ in a range of 2π . For $j = 3$, there was a total of $(2j + 1) = 7$ different m_B values, the 7 wave functions in the polar plot were listed along with m_B values in each row of graph-list. The three rows from top to bottom corresponded to the real part of rotor wave $Re[\psi]$, the imaginary part of rotor wave $Im[\psi]$, and the probability of rotor position $\psi^*\psi$. The dashed circle in each polar plot symbolized the rotor body itself.

It was clearly shown in the bottom row of Figure 4.5 that the probability of rotor position in each level of m_B was a perfect circle. It should be noted that the symmetry of rotor was exactly equivalent to the situation of quantum wave in a ring.

For illustration purposes, all the quantum rotor waves were polar plotted together in one single graph, as shown in Figure 4.6. The radial axis in each graph of Figure 4.6 was the energy level of rotor wave, but was not in exact energy scale.

The wave packet function $\Psi(j = 3, m_L = 3, \alpha = 0, \beta = \frac{\pi}{2}, \gamma, t)$ was then plotted as function of angle γ and time t , as illustrated in Figure 4.7. The propagation of wave packet was a symmetric pattern.

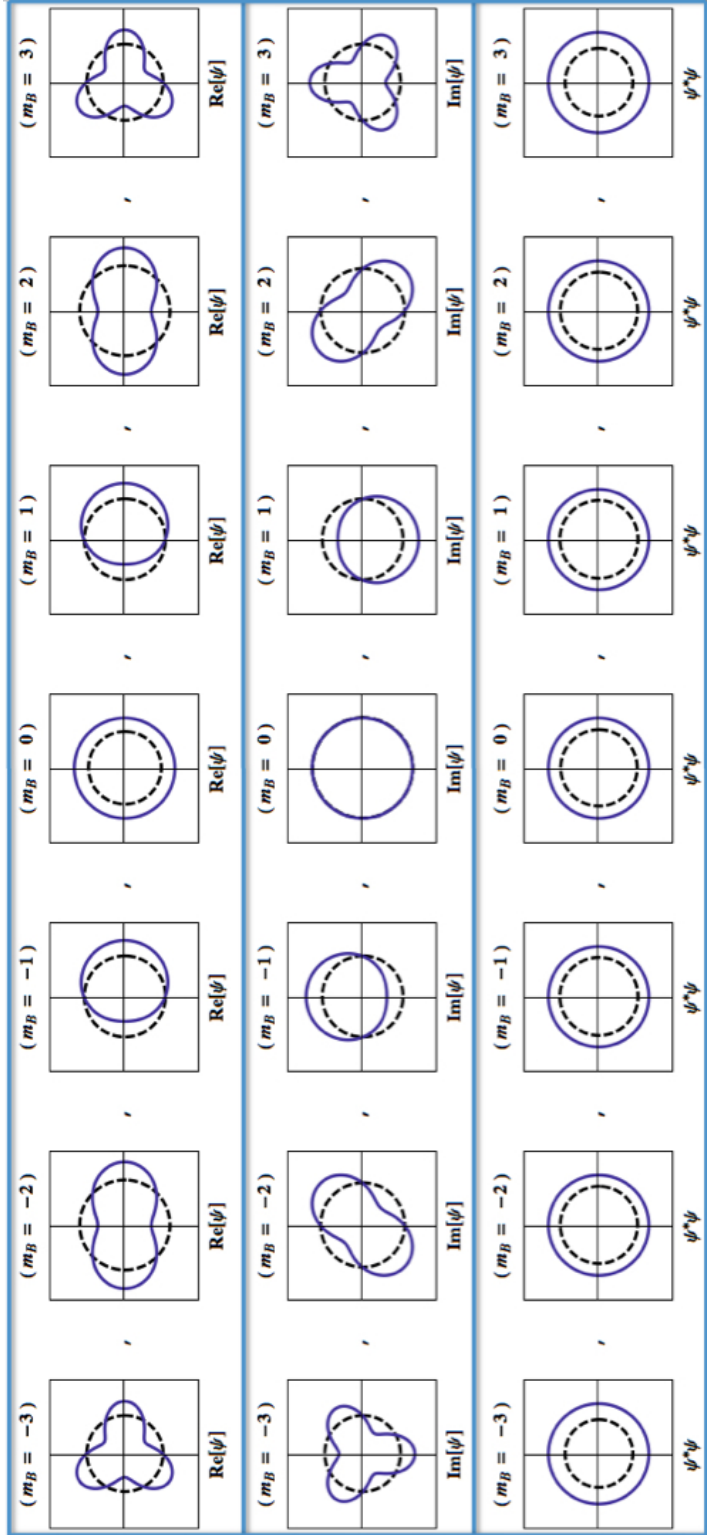


Figure 4.5: Polar plot of quantum rotor waves that each $\psi = D_{3,m_B}^{3,*}(0, \frac{\pi}{2}, \gamma)$ is plotted as a function of angle γ in a range of 2π . A total of 7 wave functions in polar plot are listed along m_B values in each row of graph-list. The three rows from top to bottom are corresponding to the real part of rotor wave $Re[\psi]$, the imaginary part of rotor wave $Im[\psi]$, and the probability of rotor position $\psi^*\psi$. The dashed circle in each polar plot symbolizes the rotor body itself.

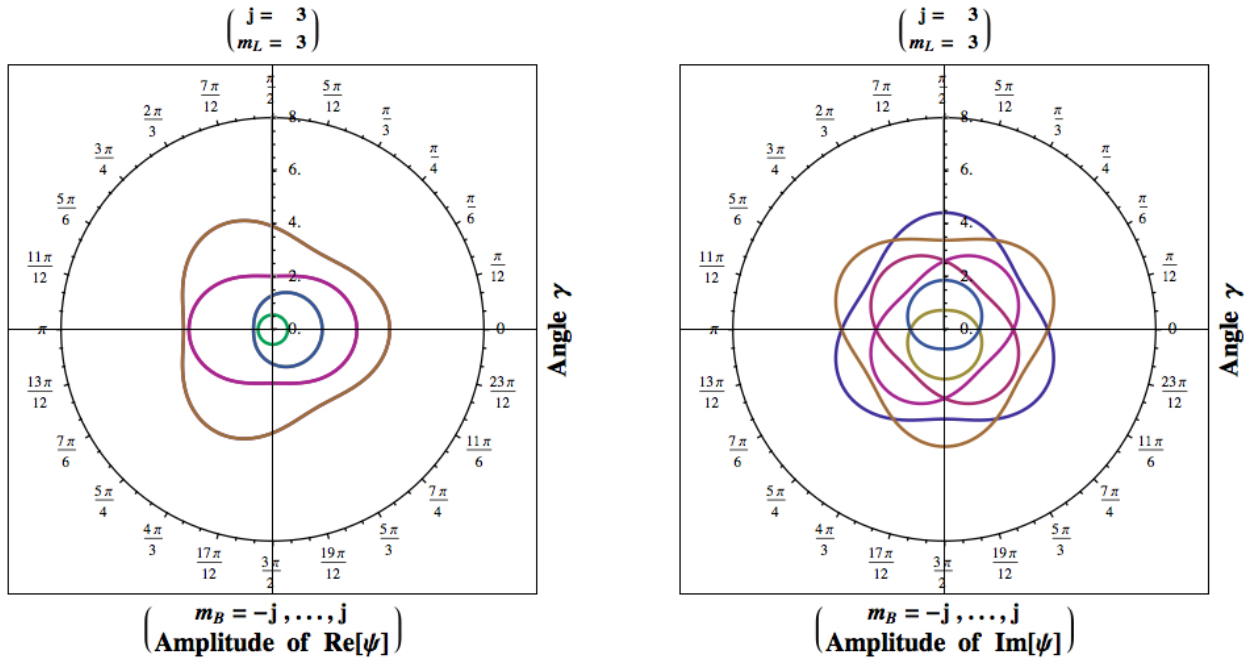


Figure 4.6: Graph on the left is a collection of all the real part of rotor waves $Re[\psi]$ that polar plotted in Figure 4.5, while graph on the right is a collection of all the imaginary part of quantum rotor waves $Im[\psi]$ that polar plotted in Figure 4.5. The radial axis in each graph is referred to as the energy level of rotor wave (not in exact energy scale).

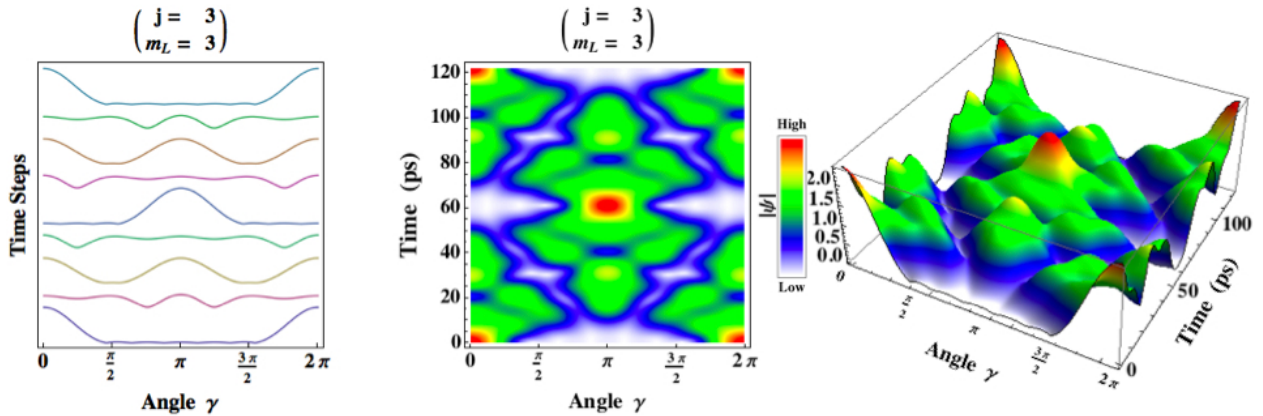


Figure 4.7: The propagation of rotor wave packet of $\Psi(j = 3, m_L = 3, \alpha = 0, \beta = \frac{\pi}{2}, \gamma, t)$. (a) The wave packet $|\Psi|$ is propagated along the time-steps. (b) The density map of the wave packet $|\Psi|$ as a function of angle and time. (c) The 3D plot of the wavepacket $|\Psi|$ as a function of angle and time.

4.2.1.2 Spin $j = 10$

In case of higher j systems, such as the $j = 10$ spin system, a richer quantum dynamic picture was expected. As indicated in Figure 4.8, each $\psi = D_{10,m_B}^{10*}(0, \frac{\pi}{2}, \gamma)$ was list-plotted as a function of angle γ in a range of 2π . For $j = 10$, there were a total of $(2j+1) = 21$ different m_B values, so that there were 21 wave functions listed along m_B values in each list plotting graph. The three graphs from left to right corresponded to real part of rotor wave $Re[\psi]$, the imaginary part of rotor wave $Im[\psi]$, and the probability of rotor position $\psi^*\psi$. At the same time, as indicated in Figure 4.9, the energy-value-based list-plot of quantum rotor waves with $\psi = D_{10,m_B}^{10*}(0, \frac{\pi}{2}, \gamma)$ was plotted as a function of angle γ . A total of 21 wave functions were listed along their energy values in each list plotting graph (only 11 waves are observed because of energy degeneracy). The three graphs from left to right corresponded to the real part of rotor wave $Re[\psi]$, the imaginary part of rotor wave $Im[\psi]$, and the probability of rotor position $\psi^*\psi$.

In case of the polar plot of quantum rotor waves, as indicated in Figure 4.10, each $\psi = D_{10,m_B}^{10*}(0, \frac{\pi}{2}, \gamma)$ was plotted as a function of angle γ in a range of 2π . For $j = 10$, there were a total of $(2j + 1) = 21$ different m_B values, so that there were 21 wave functions in polar plot listed along m_B values. The number of nodes of the rotor wave was proportional to the m_B value.

For illustration purposes, all the quantum rotor waves were polar plotted together in one single graph, as shown in Figure 4.11. The radial axis in each graph of Figure 4.11 was referred to as the energy level of rotor wave, but was not in exact energy scale.

The wave packet function $\Psi(j = 10, m_L = 10, \alpha = 0, \beta = \frac{\pi}{2}, \gamma, t)$ was plotted as a function of angle γ and time t , as illustrated in Figure 4.12. The propagation of wave packet was a symmetric pattern. The propagation of the wave packet was in symmetric pattern. A closer examination of fractional revival in Figure 4.12 led to a remarkable discovery that the quantum revival structure was nearly perfect match with the Farey-sum sequence $\{\frac{0}{1}, \frac{1}{10}, \frac{1}{8}, \frac{1}{6}, \frac{1}{5}, \frac{1}{4}, \frac{3}{10}, \frac{1}{3}, \frac{1}{2}, \frac{3}{8}, \frac{2}{5}\dots\}$, as denoted in the symmetric resonant beats in Figure 4.13.

The complete revival time of integer-spin rotor wave packet is given simply by

$$T_{rev} = \frac{2\pi}{\Delta\omega} = \frac{2\pi}{E(j, 1) - E(j, 0)} \hbar \quad (4.11)$$

where $\Delta\omega$ means the minimum beat frequency between any two eigen frequencies of the rotor states. According to the eigen energy Equation 4.3, the minimum energy gap occurs between the $m_B = 0$ and $m_B = 1$ energy levels, so that the minimum $\Delta\omega = \frac{E(j,1)-E(j,0)}{\hbar}$, as shown in bottom of Figure 4.9.

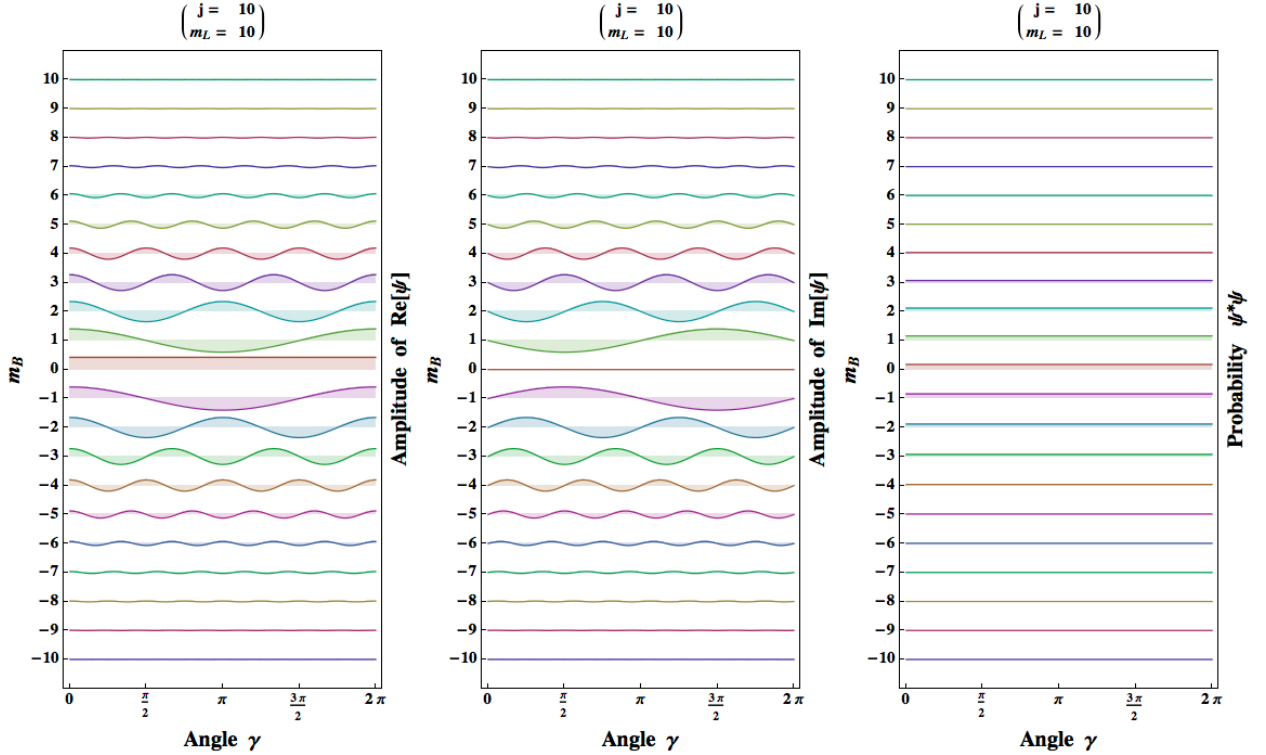


Figure 4.8: The m_B -value-based list-plot of quantum rotor waves that each $\psi = D_{10,m_B}^{10*}(0, \frac{\pi}{2}, \gamma)$ is plotted as a function of angle γ . A total of 21 wave functions are listed along m_B values in each list plotting graph. The three graphs from left to right are corresponding to the real part of rotor wave $Re[\psi]$, the imaginary part of rotor wave $Im[\psi]$, and the probability of rotor position $\psi^*\psi$.

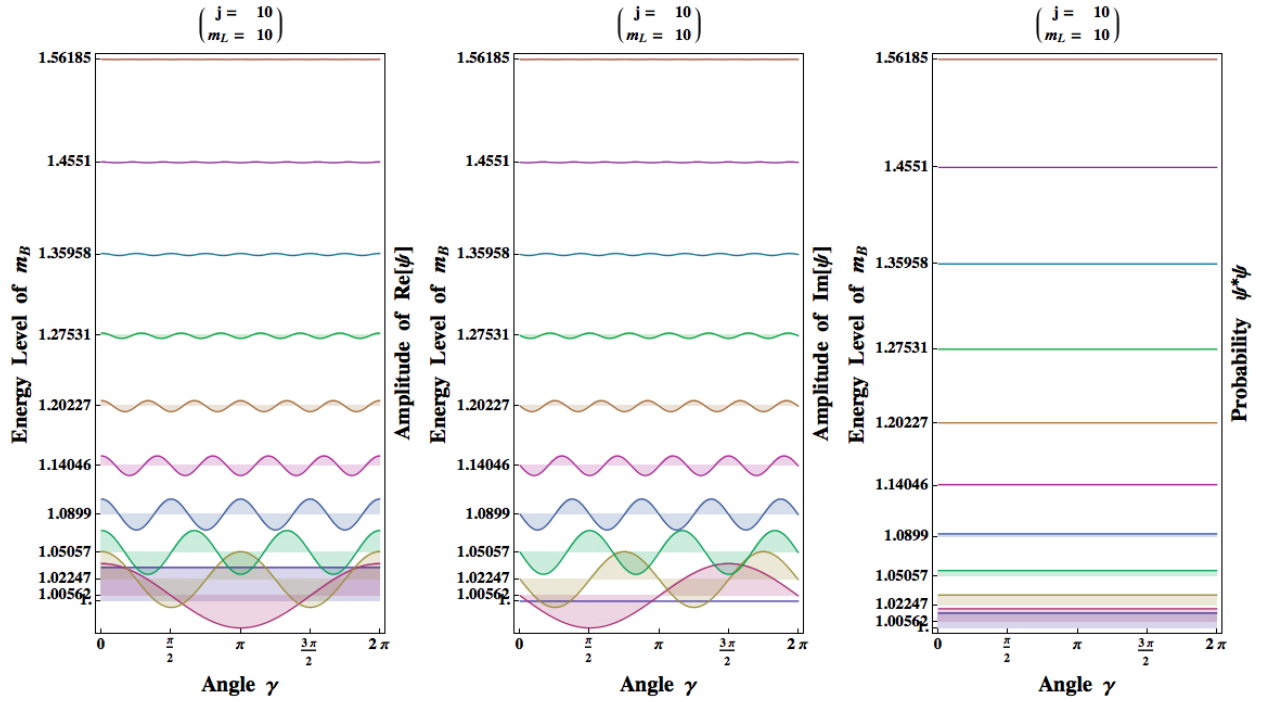


Figure 4.9: The energy-value-based list-plot of quantum rotor waves that each $\psi = D_{10, m_B}^{10} (0, \frac{\pi}{2}, \gamma)$ is plotted as a function of angle γ . A total of 21 wave functions are listed along their energy values in each list plotting graph (only 11 waves are observed because of energy degeneracy). The three graphs from left to right are corresponding to the real part of rotor wave $Re[\psi]$, the imaginary part of rotor wave $Im[\psi]$, and the probability of rotor position $\psi^* \psi$.

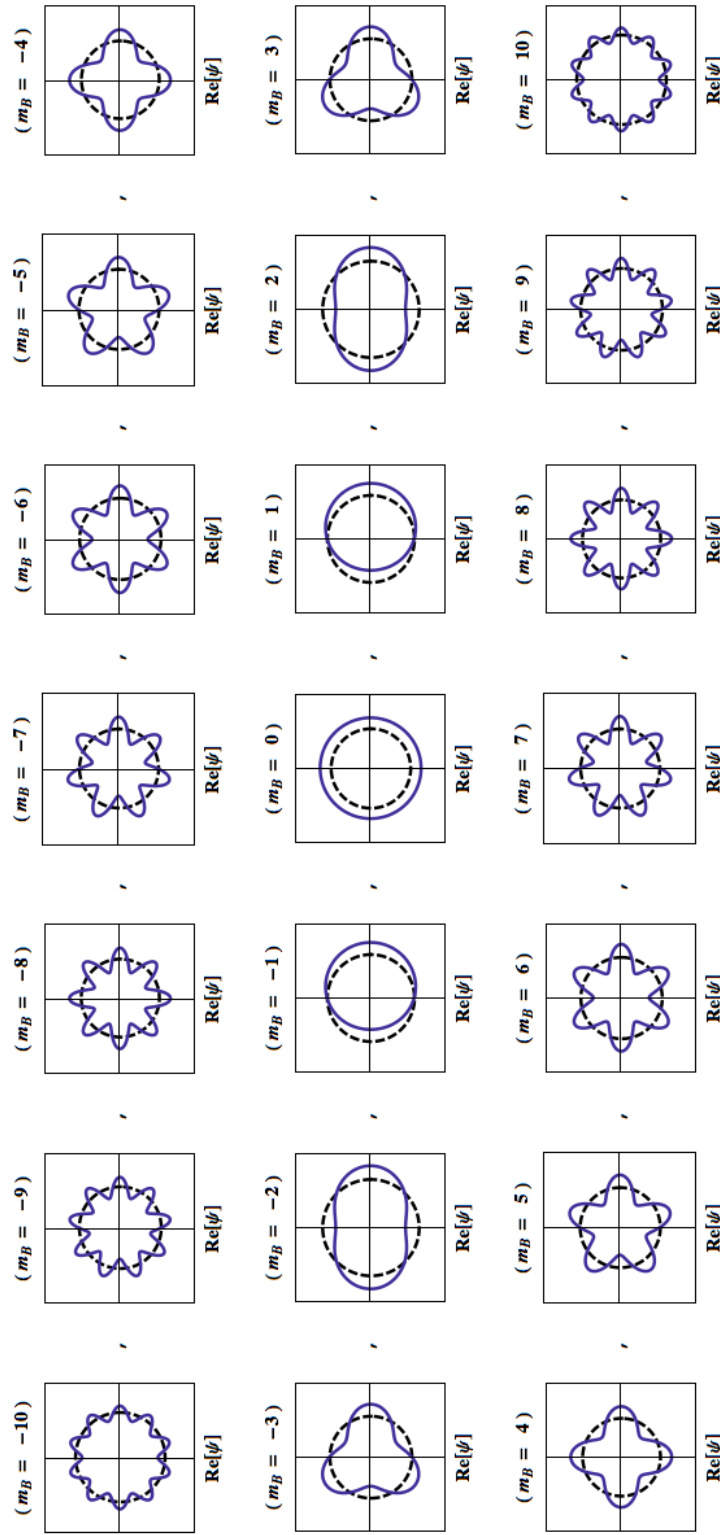


Figure 4.10: Polar plot of quantum rotor waves that each $\psi = D_{10, m_B}^{10} (0, \frac{\pi}{2}, \gamma)$ is plotted as a function of angle γ in a range of 2π . A total of 21 polar plots are listed along m_B values. Each polar plot is corresponding to the real part of rotor wave $Re[\psi]$. The dashed circle in each polar plot symbolizes the rotor body itself.

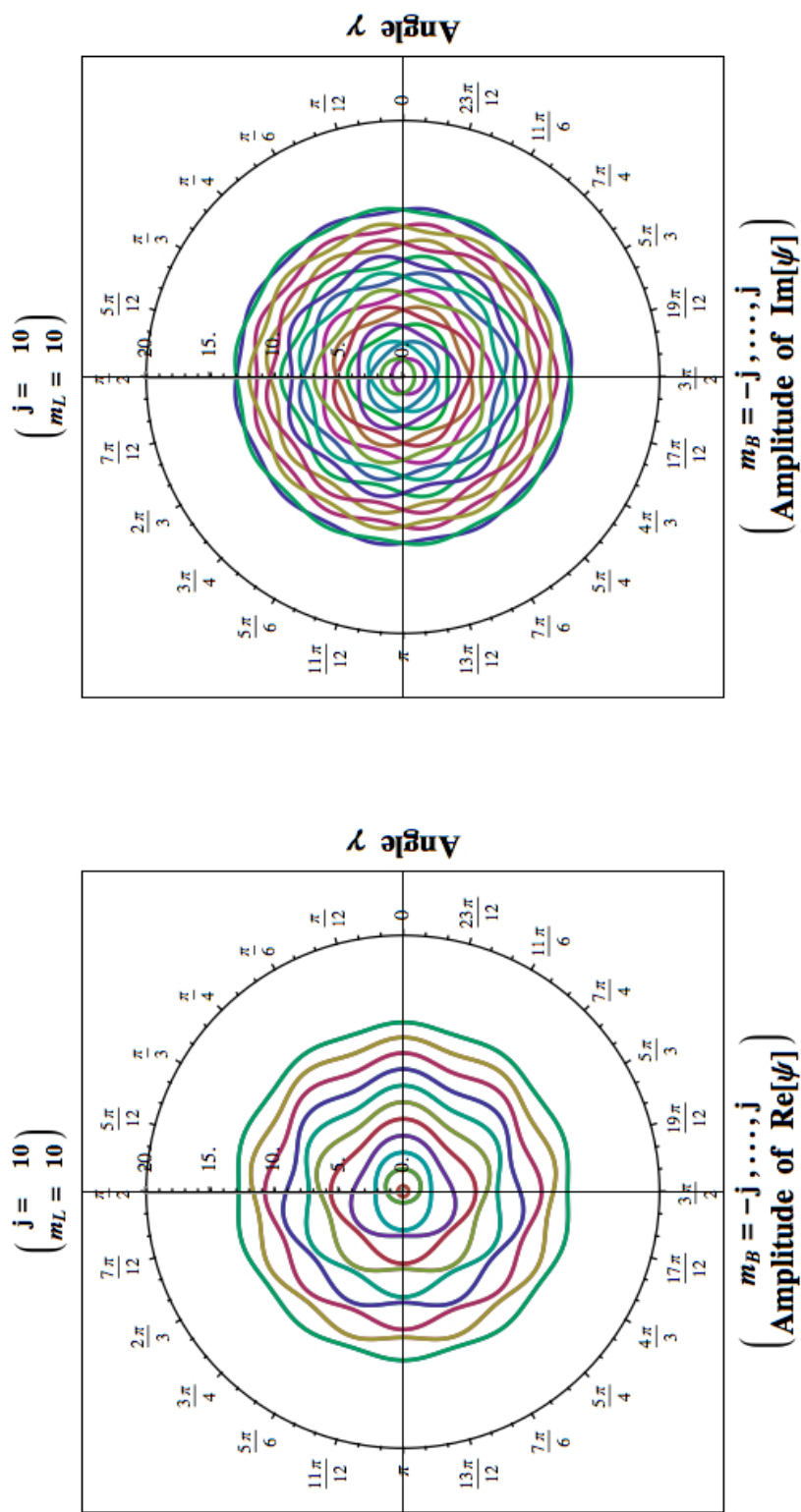


Figure 4.11: Graph on the left is a collection of all the real part of rotor waves $Re[\psi]$ that polar plotted in Figure 4.10, while graph on the right is a collection of all the imaginary part of quantum rotor waves $Im[\psi]$ that polar plotted in Figure 4.10. The radial axis in each graph is referred to as the energy level of rotor wave.

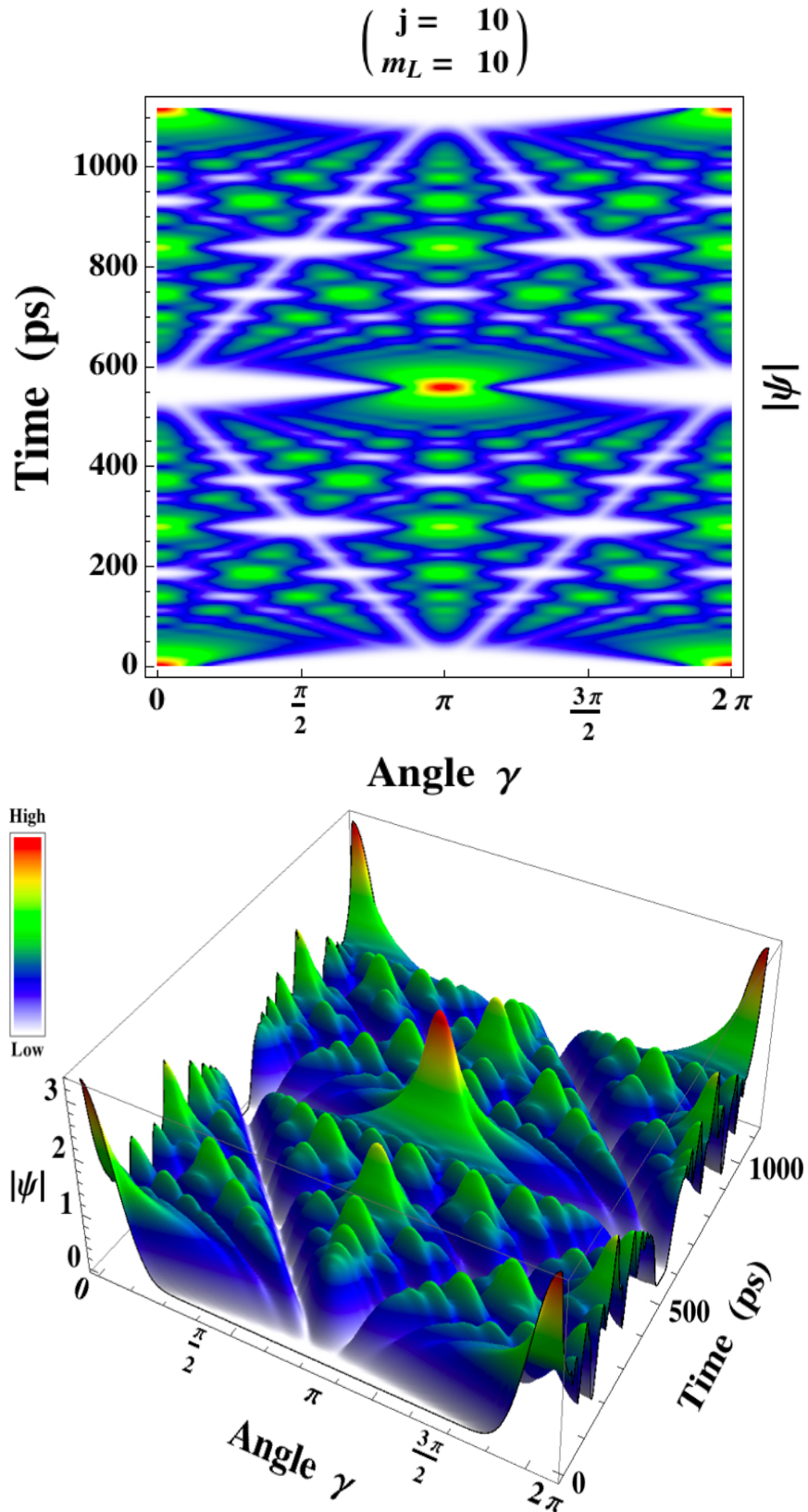


Figure 4.12: The propagation of wave packet $\Psi(j = 10, m_L = 10, \alpha = 0, \beta = \frac{\pi}{2}, \gamma, t)$. On the top is a 2D density plot of the norm $|\Psi|$. On the bottom, is a 3D plot of the norm $|\Psi|$.

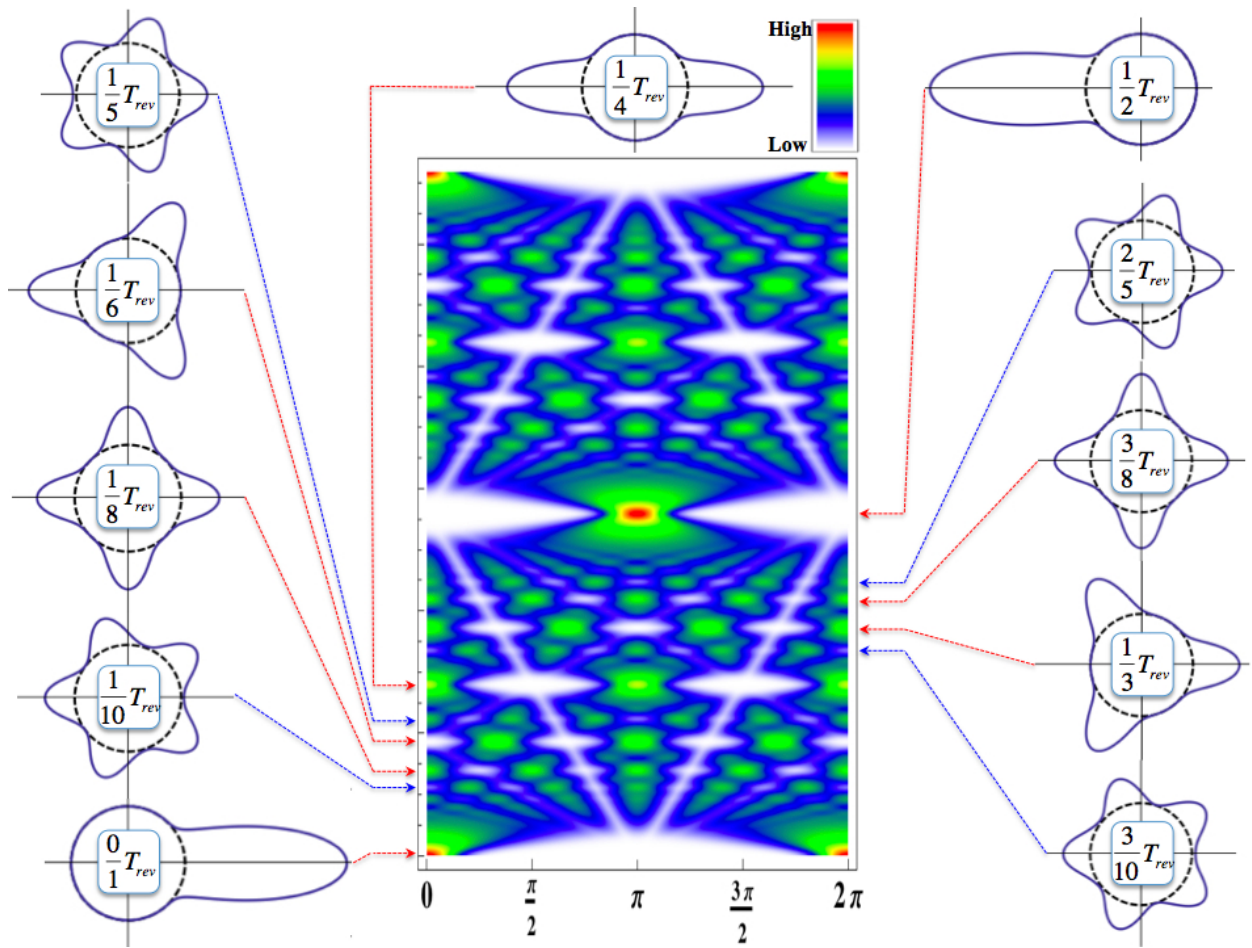


Figure 4.13: Various resonant beats during one complete revival period T_{rev} .

4.2.2 Half-integer Spin — Fermion System

For a half-integer spin system, one of its striking features is that its complete rotation in the range of 4π instead of the regular 2π of integer spin system. In order to build a concrete picture of the unusual 4π rotation, Figure 4.14 shows 4π rotation in sequential regular 2π rotations. The detail of a complete 4π rotation is distinguished by these two regular 2π rotations, as illustrated in Figure 4.14 (a-b).

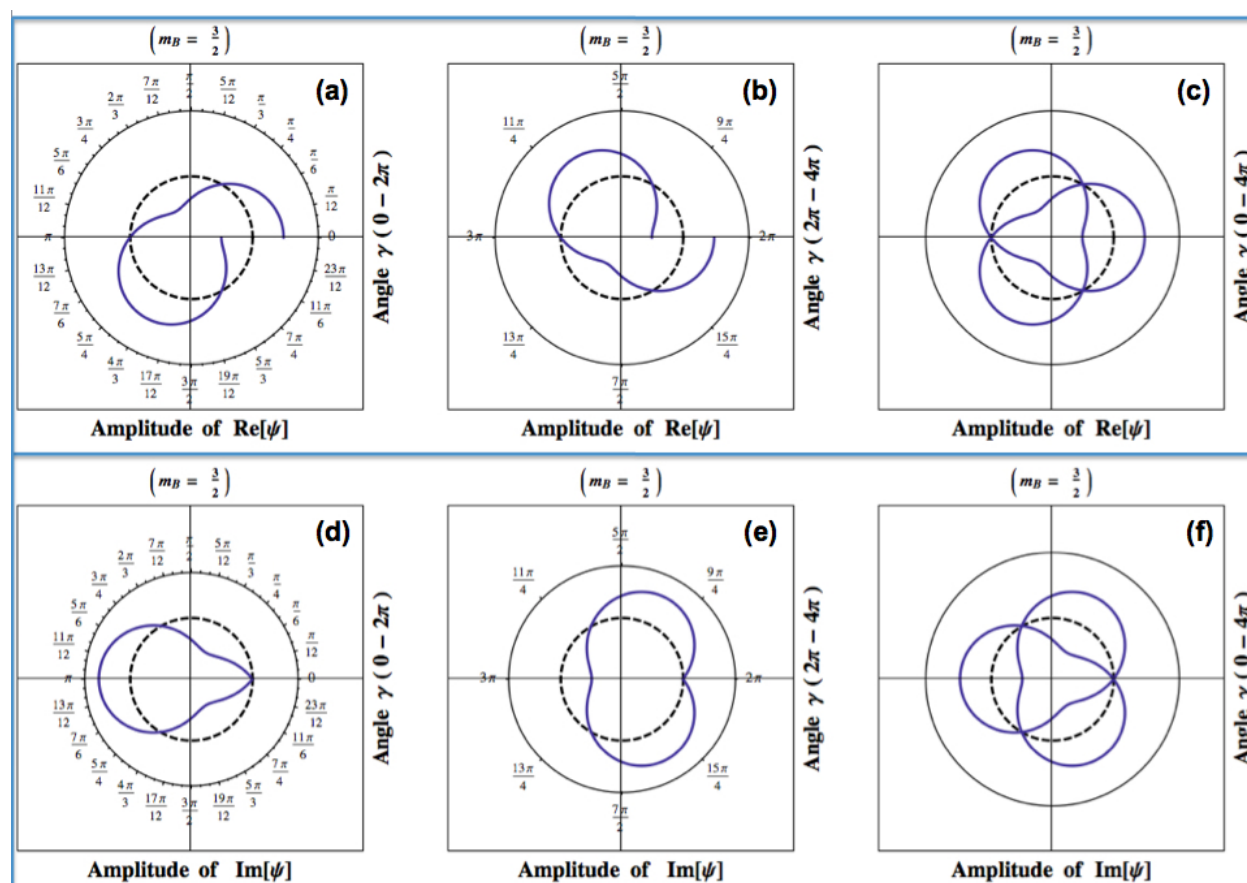


Figure 4.14: A sequential polar plots of quantum rotor wave of $j = 3/2$ ($\psi = D_{3/2, m_B}^{3/2} * (0, \frac{\pi}{2}, \gamma)$). On the top row: (a) The real part of rotor wave $Re[\psi]$ is plotted as function of γ in the range of $(0 - 2\pi)$. (b) The real part of rotor wave $Re[\psi]$ is plotted in the γ range of $(2\pi - 4\pi)$. (c) A complete rotation of the real part of rotor wave $Re[\psi]$ is plotted in a complete γ range of $(0 - 4\pi)$. On the bottom row: (d) The imaginary part of rotor wave $Im[\psi]$ is plotted as function of γ in the range of $(0 - 2\pi)$. (e) The imaginary part of rotor wave $Im[\psi]$ is plotted in the γ range of $(2\pi - 4\pi)$. (f) A complete rotation of the imaginary part of rotor wave $Im[\psi]$ is plotted in a complete γ range of $(0 - 4\pi)$. The dashed circle in each polar plot symbolizes the rotor body itself.

4.2.2.1 Spin $j = \frac{5}{2}$

For illustrating the properties of half-integer-spin rotor waves, a simple $j = \frac{5}{2}$ rotor is considered. In case of the listed plot of quantum rotor waves, as indicated in Figure 4.15, each $\psi = D_{5/2, m_B}^{5/2} (0, \frac{\pi}{2}, \gamma)$ was plotted as a function of angle γ in a range of 4π . For $j = \frac{5}{2}$, a total of $(2j + 1) = 6$ different m_B values, so that there were 6 wave functions are listed along with m_B values in each list plotting graph. The three graphs from left to right corresponded to the real part of rotor wave $Re[\psi]$, the imaginary part of rotor wave $Im[\psi]$, and the probability of rotor position $\psi^*\psi$.

At the same time, as indicated in Figure 4.16, the energy-value-based list-plot of quantum rotor waves $\psi = D_{5/2, m_B}^{5/2} (0, \frac{\pi}{2}, \gamma)$ were plotted as a function of angle γ . A total of 6 wave functions were listed along their energy values in each list plotting graph (only 3 waves are observed because of energy degeneracy). The three graphs from left to right corresponded to the real part of rotor wave $Re[\psi]$, the imaginary part of rotor wave $Im[\psi]$, and the probability of rotor position $\psi^*\psi$.

In case of the polar plot of quantum rotor waves, as indicated in Figure 4.17, each $\psi = D_{5/2, m_B}^{5/2} (0, \frac{\pi}{2}, \gamma)$ is plotted as a function of angle γ in a range of 4π . For $j = 5/2$, a total of $(2j + 1) = 6$ different m_B values, so that there are 6 wave functions in polar plot are listed along m_B values. The number of node of the rotor wave is proportional with the m_B value.

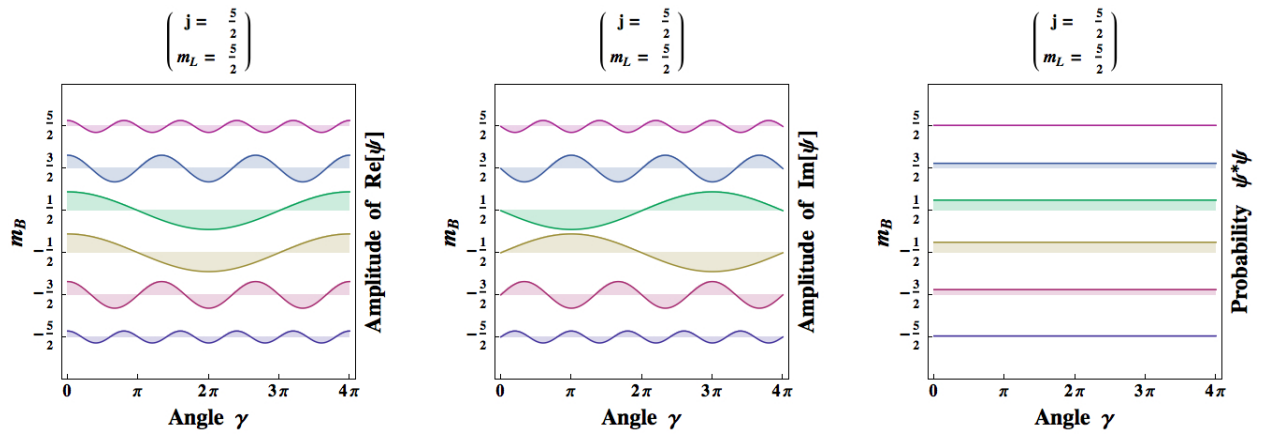


Figure 4.15: The m_B -value-based list-plot of quantum rotor waves that each $\psi = D_{5/2, m_B}^{5/2} * (0, \frac{\pi}{2}, \gamma)$ is plotted as a function of angle γ . A total of 6 wave functions are listed along m_B values in each list plotting graph. The three graphs from left to right are corresponding to the real part of rotor wave $Re[\psi]$, the imaginary part of rotor wave $Im[\psi]$, and the probability of rotor position $\psi^*\psi$.

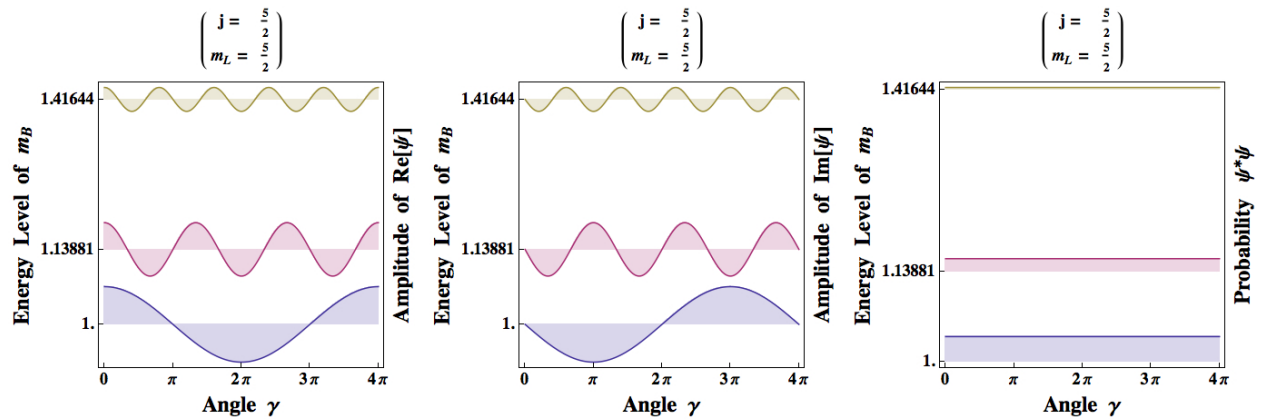


Figure 4.16: The energy-value-based list-plot of quantum rotor waves that each $\psi = D_{5/2, m_B}^{5/2} * (0, \frac{\pi}{2}, \gamma)$ is plotted as a function of angle γ . A total of 6 wave functions are listed along their energy values in each list plotting graph (only 3 waves are observed because of energy degeneracy). The three graphs from left to right are corresponding to the real part of rotor wave $Re[\psi]$, the imaginary part of rotor wave $Im[\psi]$, and the probability of rotor position $\psi^*\psi$.

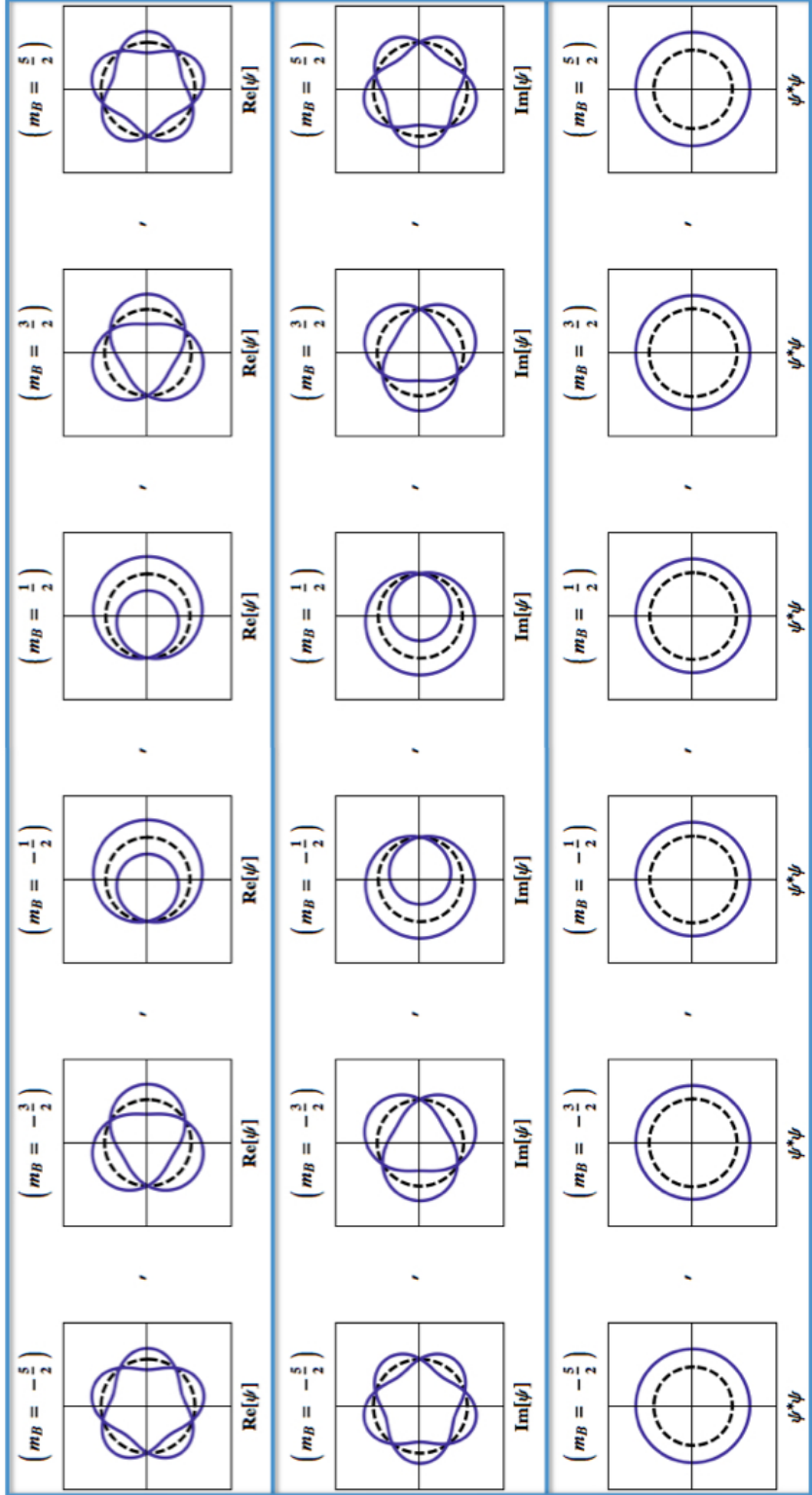


Figure 4.17: Polar plot of quantum rotor waves that each $\psi = D_{5/2, m_B}^{5/2}(0, \frac{\pi}{2}, \gamma)$ is plotted as a function of angle γ in a range of 4π . A total of 6 wave functions in polar plot are listed along m_B values in each row of graph-list. The three rows from top to bottom are corresponding to the real part of rotor wave $Re[\psi]$, the imaginary part of rotor wave $Im[\psi]$, and the probability of rotor position $\psi^*\psi$. The dashed circle in each polar plot symbolizes the rotor body itself.

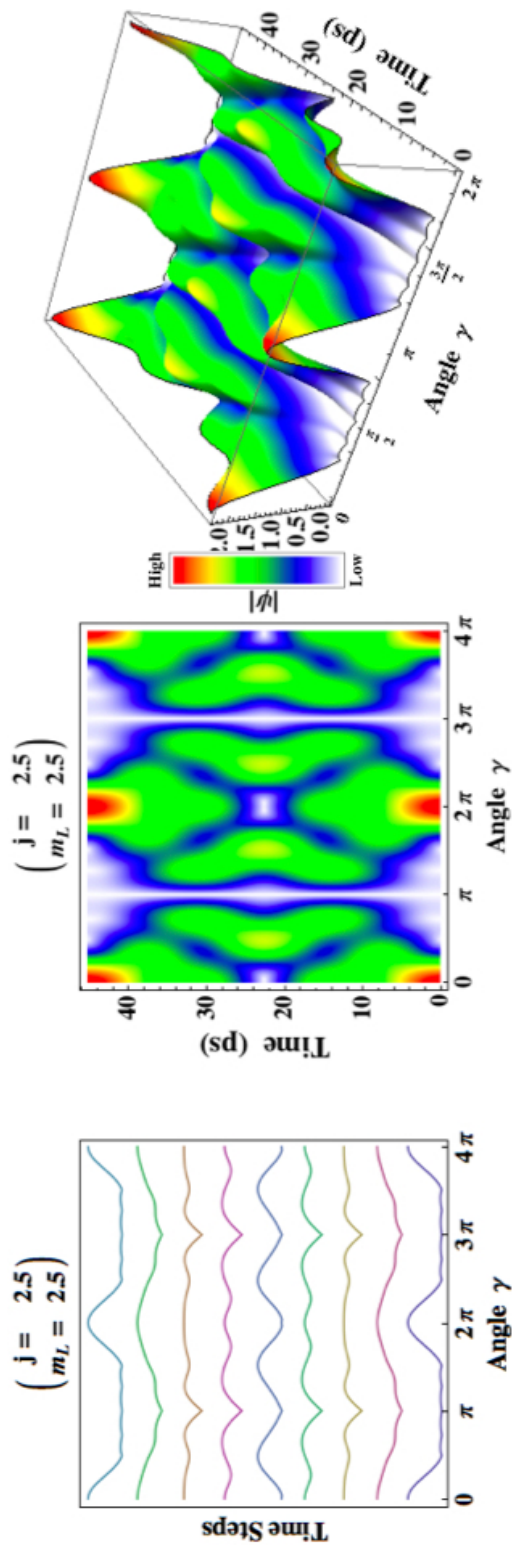


Figure 4.18: The propagation of rotor wave packet of $\Psi(j = 2.5, m_L = 2.5, \alpha = 0, \beta = \frac{\pi}{2}, \gamma, t)$. (a) The wave packet $|\Psi|$ is propagated along the time-steps. (b) The density map of the wave packet $|\Psi|$ as a function of angle and time. (c) The 3D plot of the wave packet $|\Psi|$ as a function of angle and time.

4.2.2.2 Spin $j = 9\frac{1}{2}$

In case of higher j systems, such as the $j = 9\frac{1}{2}$ spin system, a richer quantum dynamic picture was expected. As indicated in Figure 4.19, each $\psi = D_{10, m_B}^{10*}(0, \frac{\pi}{2}, \gamma)$ was list-plotted as a function of angle γ in a range of 2π . For $j = 9\frac{1}{2}$, there were a total of $(2j + 1) = 20$ different m_B values, so that there were 20 wave functions listed along with m_B values in each list plotting graph. The three graphs from left to right corresponded to the real part of rotor wave $Re[\psi]$, the imaginary part of rotor wave $Im[\psi]$, and the probability of rotor position $\psi^*\psi$. At the same time, as indicated in Figure 4.20, the energy-value-based list-plot of quantum rotor waves $\psi = D_{9.5, m_B}^{9.5*}(0, \frac{\pi}{2}, \gamma)$ was plotted as a function of angle γ . A total of 20 wave functions were listed along their energy values in each list plotting graph (only 10 waves were observed because of energy degeneracy). The three graphs from left to right corresponded to the real part of rotor wave $Re[\psi]$, the imaginary part of rotor wave $Im[\psi]$, and the probability of rotor position $\psi^*\psi$.

For illustration purposes, all the quantum rotor waves were polar plotted together in one single graph, as shown in Figure 4.22. The radial axis in each graph of Figure 4.22 was the energy level of the rotor wave, but was not in exact energy scale.

The wave packet function $\Psi(j = 9.5, m_L = 9.5, \alpha = 0, \beta = \frac{\pi}{2}, \gamma, t)$ was plotted as function of angle γ and time t , as illustrated in Figure 4.23. The propagation of the wave packet was in symmetric pattern. A closer examination of fractional revival in Figure 4.23 led to a remarkable discovery that the quantum revival structure was nearly perfect match with the Farey-sum sequence $\{\frac{0}{1}, \frac{1}{5}, \frac{1}{4}, \frac{1}{3}, \frac{2}{5}, \frac{1}{2}, \dots\}$, as denoted in the symmetric resonant beats in Figure 4.24.

The complete revival time of half-integer-spin rotor wave packet is given simply by

$$T_{rev} = \frac{2\pi}{\Delta\omega} = \frac{2\pi}{E(j, \frac{3}{2}) - E(j, \frac{1}{2})} \hbar \quad (4.12)$$

where $\Delta\omega$ means the minimum beat frequency between any two eigen frequencies of the rotor states. According to the eigen energy Equation 4.3, the minimum energy gap occurs between the $m_B = 1/2$ and $m_B = 3/2$ energy levels.

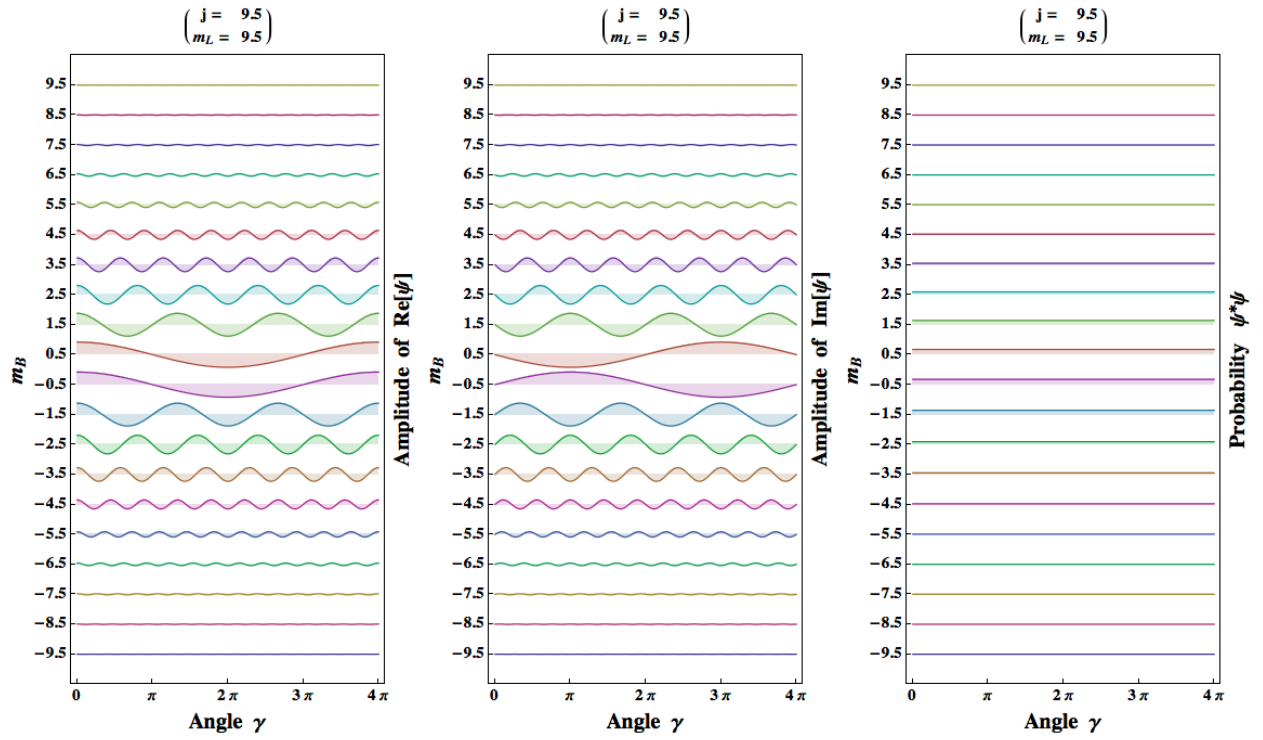


Figure 4.19: The m_B -value-based list-plot of quantum rotor waves that each $\psi = D_{9.5, m_B}^{9.5} * (0, \frac{\pi}{2}, \gamma)$ is plotted as a function of angle γ . A total of 20 wave functions are listed along m_B values in each list plotting graph. The three graphs from left to right are corresponding to the real part of rotor wave $Re[\psi]$, the imaginary part of rotor wave $Im[\psi]$, and the probability of rotor position $\psi^*\psi$.

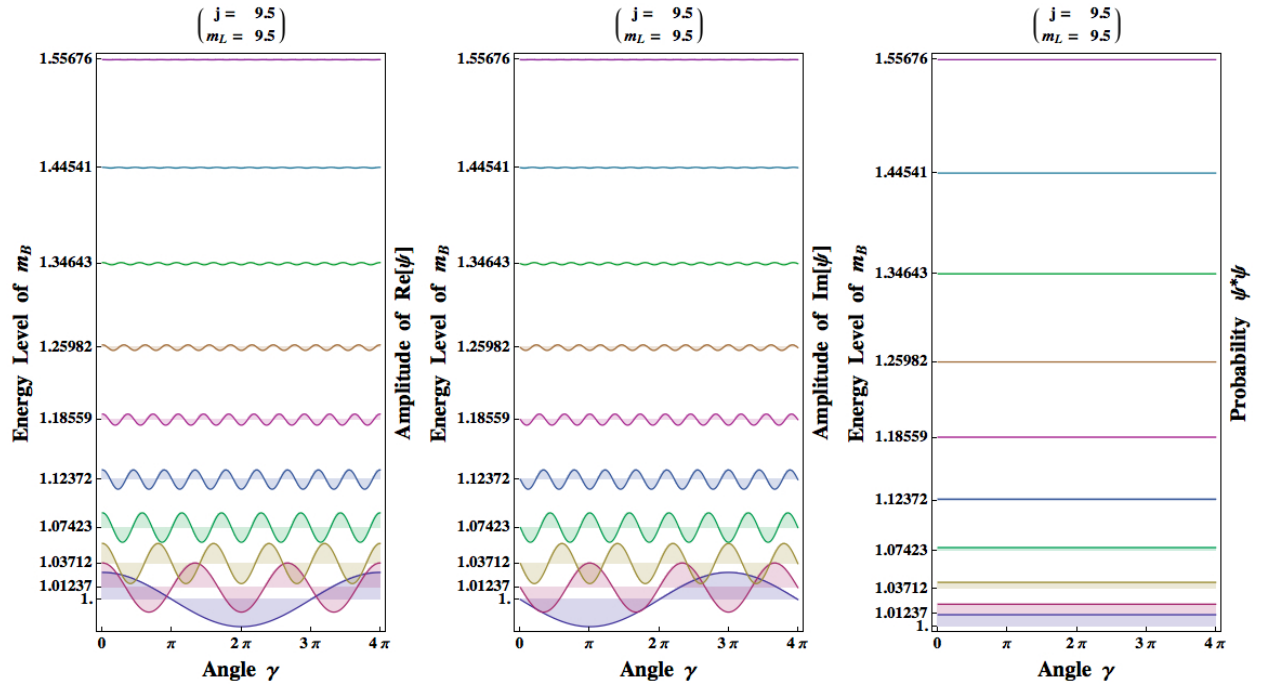


Figure 4.20: The energy-value-based list-plot of quantum rotor waves that each $\psi = D_{9.5, m_B}^{9.5} (0, \frac{\pi}{2}, \gamma)$ is plotted as a function of angle γ . A total of 20 wave functions are listed along their energy values in each list plotting graph (only 10 waves are observed because of energy degeneracy). The three graphs from left to right are corresponding to the real part of rotor wave $Re[\psi]$, the imaginary part of rotor wave $Im[\psi]$, and the probability of rotor position $\psi^* \psi$.

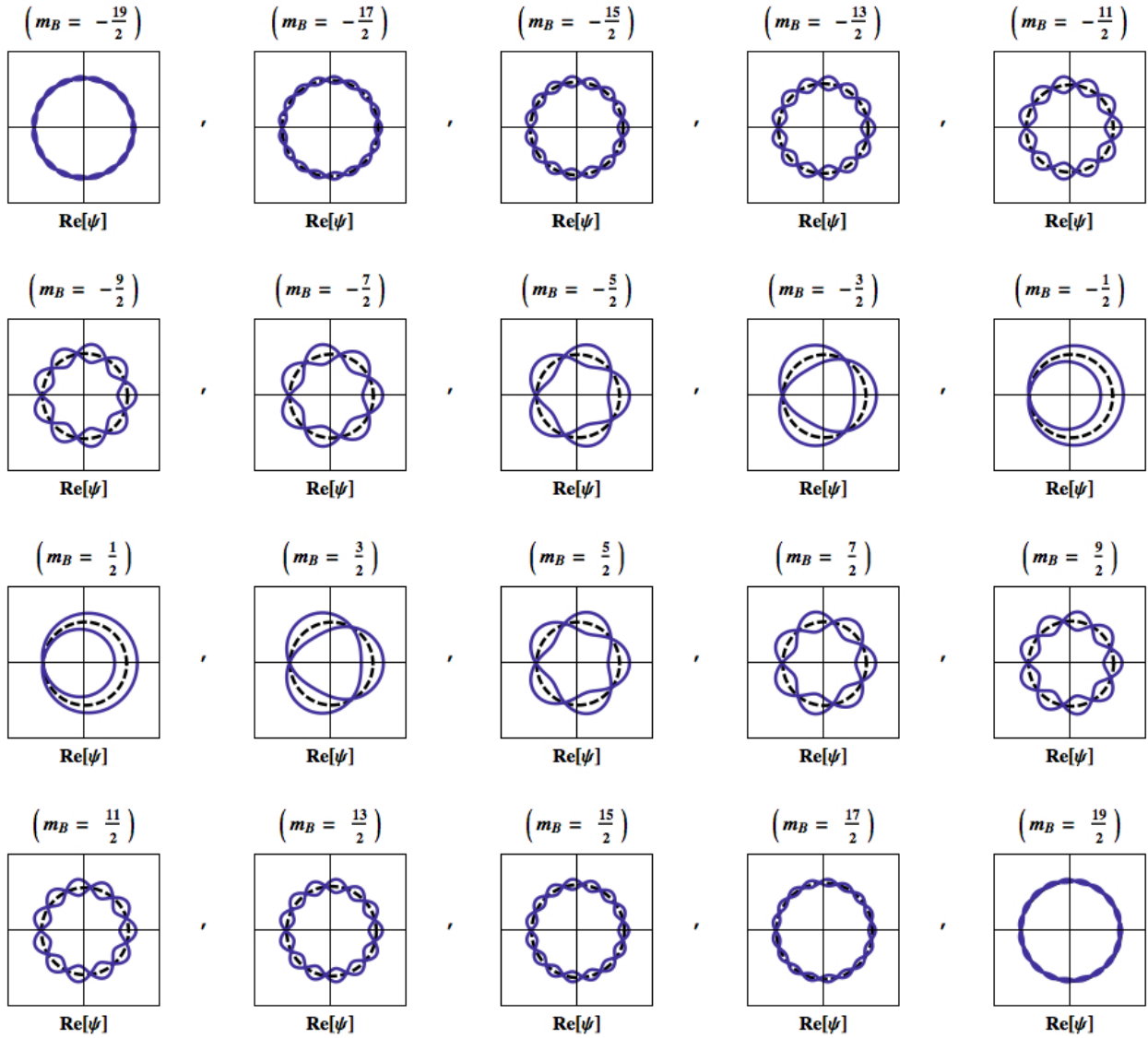


Figure 4.21: Polar plot of quantum rotor waves that each $\psi = D_{9.5, m_B}^{9.5} (0, \frac{\pi}{2}, \gamma)$ is plotted as a function of angle γ in a range of 4π . A total of 20 polar plots are listed along m_B values. Each polar plot is corresponding to the real part of rotor wave $Re[\psi]$. The dashed circle in each polar plot symbolizes the rotor body itself.

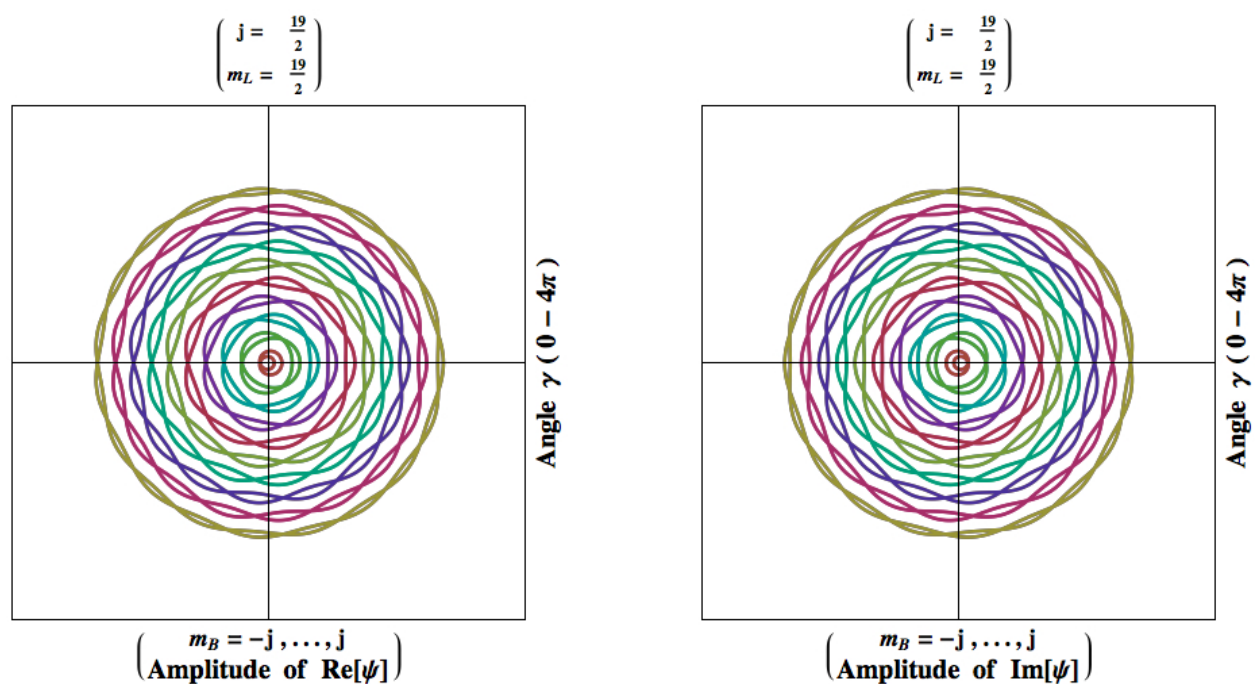


Figure 4.22: Graph on the left is a collection of all the real part of rotor waves $Re[\psi]$ that polar plotted in Figure 4.21, while graph on the right is a collection of all the imaginary part of quantum rotor waves $Im[\psi]$ that polar plotted in Figure 4.21. The radial axis in each graph is referred to as the energy level of rotor wave (not in exact energy scale).

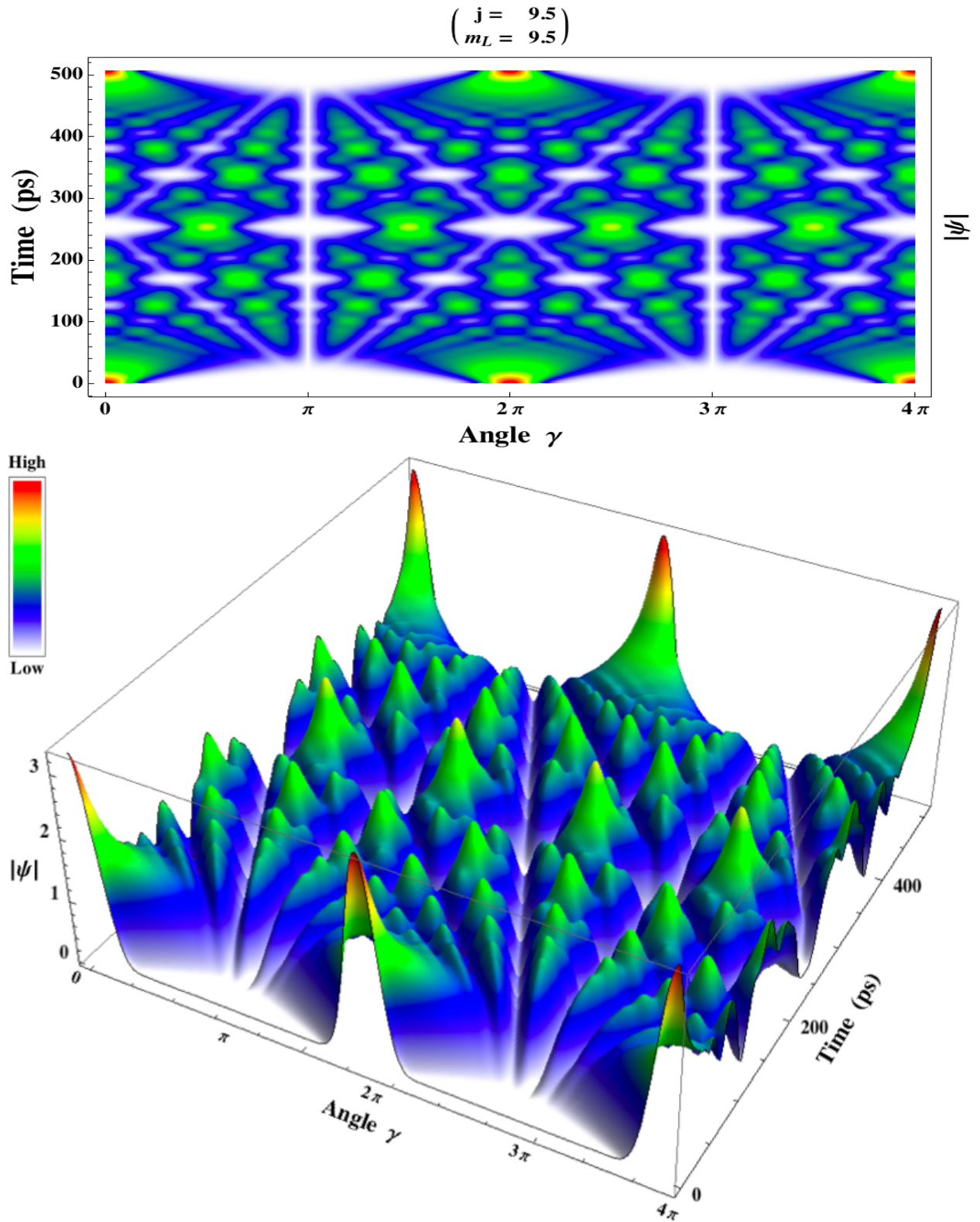


Figure 4.23: The propagation of wave packet $\Psi(j = 9.5, m_L = 9.5, \alpha = 0, \beta = \frac{\pi}{2}, \gamma, t)$. On the top is a 2D density plot of the norm $|\Psi|$. On the bottom, is a 3D plot of the norm $|\Psi|$.

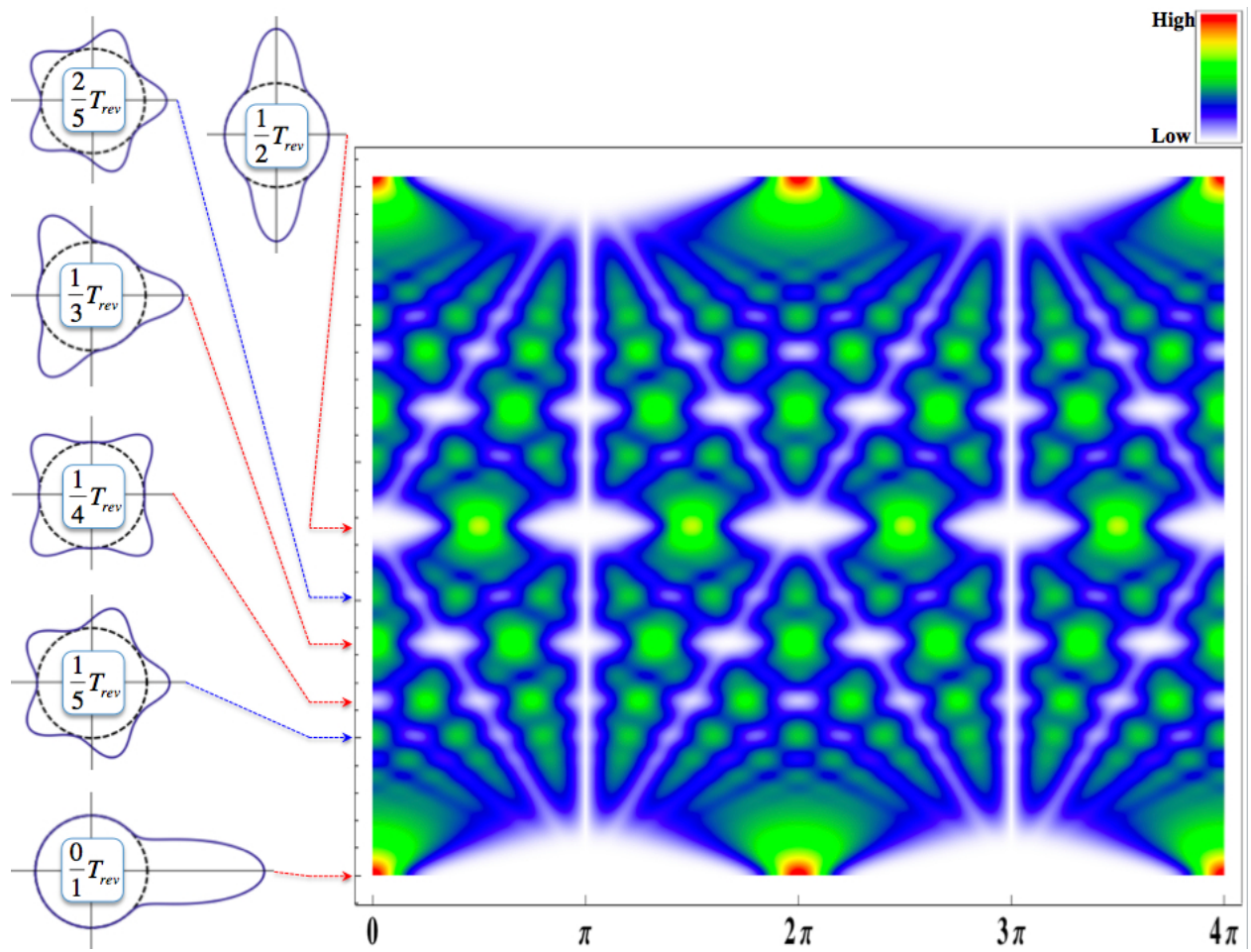


Figure 4.24: Various symmetric resonant beat during one complete revival period T_{rev} .

4.3 Conclusion of Rotor Dynamics

In conclusion, quantum rotor wave functions based upon Wigner-D matrix were applied to investigate the quantum resonance and revivals that occur in experimentally accessible spin systems. Interesting physical effects in quantum rotors between half-integer spin and integer spin systems was observed that showed effects of symmetry. This study will pave the way for more rich dynamic behaviors in asymmetric tops that include dynamic tunneling between various equivalent energy surface topography for asymmetric quantum rotors. A key point is that the quantum revivals in the rotor systems exhibited number-information aspects of surprisingly simple Farey-sum and Ford-circle geometry.

Chapter 5

Conclusion

This investigation of quantum resonant beats and revivals in Morse oscillators and Symmetric rotor was provided a deeper insight into the physical reality of quantum wave interference. Indeed, advanced analytical and numerical tools were developed to efficiently visualize and predict the phenomenon of interference beats and revivals in more detail than has been reported before.

For the Morse oscillator, the exact analytical wavefunctions of the Morse oscillator allowed an detailed analysis of the rich behavior of the quantum dynamics. Based on the key parameter δ_N relating with the gap between the highest bound eigenstate and the dissociation energy, a concise way for searching the exact complete revival time T_{rev} of the Morse oscillator was given for the first time. The applications of two fundamental periods $T_{max-beat}$ and $T_{min-rev}$ allowed the discovery of the relationship between Fibonacci sequence and the Morse complete revival time. Particularly, the minimum period $T_{min-rev}$ suggested a quantized period concept that the complete period is made of integer numbers of the fundamental period in the quantum world of the Morse oscillator. A closer examination led to a discovery that the quantum resonance and revival structure had a curious connection with the Farey-sum structure, which was illustrated with the classical Ford circles. This Fibonacci-Farey-Ford geometry should provide a further step towards a systematic understanding of the quantum wave packet dynamics.

For double-Morse oscillators, with a best-fit parameters scheme, a specified double-Morse potential was developed to have high fidelity of the quasi-solvable Razavy potential. So that exact analytical eigenfunctions and eigenvalues up to $n = 22$ energy levels of the double-well potential are achieved for the first time. Through an efficient matrix scheme, fine detail of an energy splitting analysis was available for the study of the diverse behavior of quantum dynamics involving tunneling. A closer examination led to a discovery that the non-tunneling wave functions had a significant tsunami-like wave effect, which is relevant on the local top (coastal beach landscape) in the double-well potential. This exact computed energy in a deep double-Morse potential is desired for many applications, because exact solutions of the unperturbed model will make the perturba-

tion effect easy to handle in practical problems, and has set up a solid basis for the future study of quantum interference and entanglement.

For quantum rotors, quantum rotor wave functions based upon Wigner-D matrix were applied to investigate the quantum resonance and revivals that occur in experimentally accessible spin systems. Interesting physical effects in quantum rotors between half-integer spin and integer spin systems was observed to show the effects of symmetry. This study will pave the way for understanding colorful dynamic behaviors in asymmetric tops that include dynamic tunneling between various equivalent energy surface topography for asymmetric quantum rotors. A key point was that the quantum revivals in the rotor systems exhibited number-information aspects of surprisingly simple Farey-sum and Ford-circle geometry.

Notably, the novel features of the resonant states emerging from these quantum models are leading to interesting findings, such as the possible universality of Farey-sum revival structures. Importantly, these simple quantum models will provide remarkable examples of naturally occurring and experimentally accessible systems, in which the resonance and revival of quantum matter wave may eventually lead to great applications for quantum information processing and computing.

References

- [1] E. Schrodinger, “The continuous transition from micro to macro mechanics,” *Naturwissenschaften*, vol. 14, pp. 664–666, 1926.
- [2] R. J. Glauber, “The quantum theory of optical coherence,” *Phys. Rev.*, vol. 130, p. 2529, 1963.
- [3] R. S. Academy, “Press release: the 2005 nobel prize in physics,” 2005.
- [4] A. H. Zewail, “Laser femtochemistry,” *Science*, vol. 242, p. 1645, 1988.
- [5] R. S. Academy, “Press release: the 1999 nobel prize in chemistry,” 1999.
- [6] J. H. Eberly, N. B. Narozhny, and J. J. Sanchez-Mondragon, “Periodic spontaneous collapse and revival in a simple quantum model,” *Phys. Rev. Lett.*, vol. 44, p. 1323, 1980.
- [7] E. J. Heller, “Time dependent approach to semiclassical dynamics,” *J. Chem. Phys.*, vol. 62, p. 1544, 1975.
- [8] R. S. McDowell, C. W. Patterson, and W. G. Harter, “The modern revolution in infrared spectroscopy,” *Los Alamos Science*, vol. 3, pp. 38–65, 1982.
- [9] B. Feuerstein and U. Thumm, “Mapping of coherent and decohering nuclear wave-packet dynamics in d2 with ultrashort laser pulses,” *Phys. Rev. A*, vol. 67, no. 063408, 2003.
- [10] A. Rudenko, T. Ergler, B. Feuerstein, K. Zrost, C. D. Schroter, R. Moshhammer, and J. Ullrich, “Real-time observation of vibrational revival in the fastest molecular system,” *Chem. Phys.*, vol. 329, pp. 193–202, 2006.
- [11] T. Niederhausen and U. Thumm, “Controlled vibrational quenching of nuclear wave packets in d2,” *Phys. Rev. A*, vol. 77, no. 013407, 2008.
- [12] K. Ohmori, “Wavepacket and coherent control dynamics,” *Annu. Rev. Phys. Chem.*, vol. 60, pp. 487–511, 2009.
- [13] W. G. Harter, “Quantum-fractal revival structure in cn quadratic spectra: Base-n quantum computer registers,” *Phys. Rev. A*, vol. 64, no. 012312, 2001.
- [14] W. G. Harter, “Wave node dynamics and revival symmetry in quantum rotors,” *J. Mol. Spectrosc.*, vol. 210, p. 166, 2001.
- [15] H. Mack, M. Bienert, F. Haug, M. Freyberger, and W. Schleich, “Wave packets can factorize numbers,” *phys. stat. sol. (b)*, vol. 233, no. 3, pp. 408–415, 2002.
- [16] M. Gilowski, T. Wendrich, T. Müller, C. Jentsch, W. Ertmer, E. M. Rasel, and W. P. Schleich, “Gauss sum factorization with cold atoms,” *Phys. Rev. Lett.*, vol. 100, no. 030201, 2008.
- [17] A. Z. Li and W. G. Harter, “The quantum revivals of the morse oscillator in position space and momentum space,” in *American Physical Society March Meeting 2012*, vol. 57, 2012.

- [18] P. M. Morse, "Diatomic molecules according to the wave mechanics. ii. vibrational levels," *Phys. Rev.*, vol. 34, p. 57, 1929.
- [19] V. P. Gutschick and M. M. Nieto, "Coherent states for general potentials. v. time evolution," *Phys. Rev. D*, vol. 22, p. 403, 1980.
- [20] J. P. Dahl and M. Springborg, "The morse oscillator in position space, momentum space, and phase space," *J. Chem. Phys.*, vol. 88, p. 4535, 1988.
- [21] S. Kais and R. D. Levine, "Coherent states for the morse oscillator," *Phys. Rev. A*, vol. 41, p. 2301, 1990.
- [22] M. Angelova and V. Hussin, "Generalized and gaussian coherent states for the morse potential," *J. Phys. A: Math. Theor.*, vol. 41, no. 304016, 2008.
- [23] Z. Wang and E. J. Heller, "Semiclassical investigation of the revival phenomena in a one-dimensional system," *J. Phys. A: Math. Theor.*, vol. 42, no. 285304, 2009.
- [24] A. B. McCoy, "Curious properties of the morse oscillator," *Chemical Physics Letters*, vol. 501, pp. 603–607, 2011.
- [25] S. Dong, R. Lemus, and A. Frank, "Ladder operators for the morse potential," *Int. J. Quantum Chem.*, vol. 86, p. 433, 2002.
- [26] I. S. Averbukh and N. F. Perelman, "Fractional revivals universality in the long-term evolution of quantum wave packets beyond the correspondence principle dynamics," *Phys. Lett. A*, vol. 139, p. 449, 1989.
- [27] R. W. Robinett, "Quantum wave packet revivals," *Phys. Rep.*, vol. 392, pp. 1–119, 2004.
- [28] T. Lohmuller, V. Engel, J. Beswick, and C. Meier, "Fractional revivals in the rovibrational motion of i_2 ," *J. Chem. Phys.*, vol. 120, no. 22, p. 10442, 2004.
- [29] V. V. Eryomin, S. I. Vetchinkin, and I. M. Umanskii, "Manifestations of wave packet fractional revivals in a morselike anharmonic system," *J. Chem. Phys.*, vol. 101, p. 10730, 1994.
- [30] G. H. Hardy and E. M. Wright, *An Introduction to the Theory of Numbers*. New York: Oxford University Press, 5 ed., 1979.
- [31] L. R. Ford, "Fractions," *The American Mathematical Monthly*, vol. 45, no. 9, pp. 586–601, 1938.
- [32] A. Caticha, "Construction of exactly soluble double well potentials," *Phys. Rev. A*, vol. 51, p. 4264, 1995.
- [33] D. Kakofengitis and O. Steuernagel, "Double-well quantum tunneling visualized via wigner function," *arXiv:1108.2214v1 (2011)*, 2011.
- [34] M. Razavy, "An exactly soluble schrodinger equation with a bistable potential," *Am. J. Phys.* 48 285–8, vol. 48, p. 285, 1980.

- [35] F. Finkel, A. Gonzalez-Lopez, and M. A. Rodriguez, “On the families of orthogonal polynomials associated to the razavy potential,” *J. Phys. A: Math. Gen.*, vol. 32, pp. 6821–6835, 1999.
- [36] S. Habib, A. Khare, and A. Saxena, “Statistical mechanics of double sinh-gordon kinks,” *Phys. D*, vol. 123, pp. 341–356, 1998.
- [37] L. Yuan, S. W. Teitelbaum, A. Robinson, and A. S. Mullin, “Dynamics of molecules in extreme rotational states,” *Proc. Natl. Acad. Sci. U.S.A.*, vol. 108, p. 6872, 2011.
- [38] U. Steinitz, Y. Prior, and I. S. Averbukh, “Laser induced gas vortices,” *Phys. Rev. Lett.*, vol. 109, p. 033001, 2012.
- [39] W. G. Harter, *Springer Handbook of Atomic, Molecular, and Optical Physics*, vol. 32. Springer, 2 ed., 2005.
- [40] E. P. Wigner, *Group Theory and Its Application to the Quantum Mechanics of Atomic Spectra*. Academic Press, 1959.
- [41] W. G. Harter, *Principles of Symmetry, Dynamics, and Spectroscopy*. Wiley-VCH, 1 ed., 1993.

Appendix A

Description of Research for Popular Publication

Exactly prediction of period is extremely important for many applications in the advancement level of civilization in human history. In ancient time, accurate dated celestial events are essential things for establishing a coherent society, such as lunar phase calendar for cultivating crops. Particularly, the Moon eclipse and Solar eclipse were vital for religious, political, and social purposes, so that, the prediction of eclipse period is of great challenges for ancient astrologers. In modern time, advanced microelectronic and photonic devices are all based on the novel quantum wave mechanics, so the prediction of quantum wave events is of great interests for cutting edge technology. However, the exact prediction of quantum wave revivals is of great challenges for quantum scientists. Now, for the first time, the exact prediction of quantum wave events in anharmonic Morse oscillator has been achieved by a concise formula.

“Consider an analogy with macro lunar event to describe micro quantum event, the achievement of my formula is likely to develop an exact prediction of moon eclipse, whereas existing publications are only of moon phase forecasting,” says Alvason Zhenhua Li, a recent Ph.D. graduate at University of Arkansas. “I am quite amazed that the formula I made stands up and gives rise precise results for any parameters. I almost gave up during this long-haul researching journey.”

His prediction method is of building block concept — In this quantum world, there is existing the minimum or fundamental period, any completely period is made of integer numbers of the fundamental period. Thus, any complete period in the quantum world is quantized. Alvason thinks his strategy for searching exact period prediction may be applied in other areas, such as stock market trend and earthquake prediction.

“More interesting thing is that there are two kinds of building block for the same period,” says Alvason. “A useful analogy to this fact is that we can pay the same product by two basic monetary units, such as applying either U.S. dollar or Chinese yuan. The fantastic thing is that the exchange rate between these two currencies is exhibiting Fibonacci ratio when they are used in the quantum world.”

Within a fundamental period, the resonant pattern of the quantum wave packet will exhibit the same as the geometric pattern of Ford circles in classical daily world. “The beauty of this research is that modern quantum resonant pattern can be traced and outlined by ancient Greek geometry,” says William Harter, a theoretical physicist specializing in molecular dynamics and spectroscopy at University of Arkansas. “Remarkably, this Ford circles or Farey-sum feature is sharing among several quantum systems including quantum oscillators and rotors.

“My cooperater in physics at Caltech suggests this fantastic research to be published in Physical Review Letters”, says Wenying Shou, a professor of the basic science division at FHCRC center, Seattle.

Both William Harter and Alvason Li suggest that this simple quantum model will provide remarkable examples of naturally occurring and experimentally accessible systems, in which the resonance and revival of quantum matter wave may eventually lead to great applications for quantum information processing and computing.

Appendix B

Executive Summary of Newly Created Intellectual Property

A total of four new intellectual property items were created and developed during this dissertation research:

1. An idea or concept of quantized period in certain quantum world.
2. A method for exactly predicting revival period in quantum resonance and revivals of the Morse oscillator.
3. A discovery of Farey-sum structure and Ford circles geometry in the quantum resonance and revivals of the Morse oscillator and quantum rotors.
4. A best-fit-parameter scheme and the corresponding efficient matrix scheme for the exact solutions in the Double-Morse oscillator.

Appendix C

Potential Patent and Commercialization Aspects of Each Numbered Item in Appendix B

C.1 Patentability of Intellectual Property

First, the listed items were considered from the perspective of whether or not the item could be patented.

1. The idea or concept of quantized period can not be patented, because it is just a new scientific term.
2. The method developed in this research to predict the completely revival time in the quantum resonance and revivals of the Morse oscillator will not be patented, because the detailed application scheme is required for the patent processing.
3. The discovery of Farey-sum structure and Ford circles geometry in the quantum resonance and revivals will not be patented, because the detailed application scheme is required for the patent processing.
4. The best-fit-parameter scheme and the corresponding efficient matrix algorithm for the exact solutions in the Double-Morse oscillator will not be patented, because the detailed application scheme is required for the patent processing.

C.2 Commercialization Possibilities of Intellectual Property

Then, the following listed were considered from the perspective of whether or not the item should be patented.

1. The idea or concept of quantized period can not be patented.
2. The method developed in this research to predict the completely revival time in the quantum resonance and revivals of the Morse oscillator should not be patented. Because the detailed application scheme is lacking.

3. The discovery of Farey-sum structure and Ford circles geometry in the quantum resonance and revivals should not be patented. Because the detailed application scheme is lacking.
4. The best-fit-parameter scheme and the corresponding efficient matrix algorithm for the exact solutions in the Double-Morse oscillator should not be patented. Because the detailed application scheme is lacking.

C.3 Possible Prior Disclosure of Intellectual Property

The following items were discussed in a public forum that could impact the patentability of the listed intellectual property.

1. The idea or concept of quantized period has been discussed in an international conference, however, the detail of method has not been published.
2. This newly developed method of period prediction has been discussed in an international conference, however, the detail of the method has not been published.
3. The discovery of Farey-sum structure and Ford circles geometry in Morse oscillator has been discussed in two international conference (the APS March Meeting 2012 and the International Symposium on Molecular Spectroscopy 2012), however, the detail of analysis has not been published. The discovery of Farey-sum structure and Ford circles geometry in half-integer spin system has not been discussed in any forum.
4. The best-fit-parameter scheme and the corresponding efficient matrix algorithm for the exact solutions in the Double-Morse oscillator has been discussed in an international conference (the International Symposium on Molecular Spectroscopy, 67th meeting 2012), however, the detail of scheme and algorithm has not been published.

Appendix D

Broader Impact of Research

D.1 Applicability of Research Methods to Other Problems

The strategy and approach for developing exactly prediction of quantum resonant beat and revival period were considered valuable in any prediction or forecast system. In principle, any system has its unique harmonic or resonant frequency so that the basic philosophy of this research could be applied elsewhere.

D.2 Impact of Research Results on U.S. and Global Society

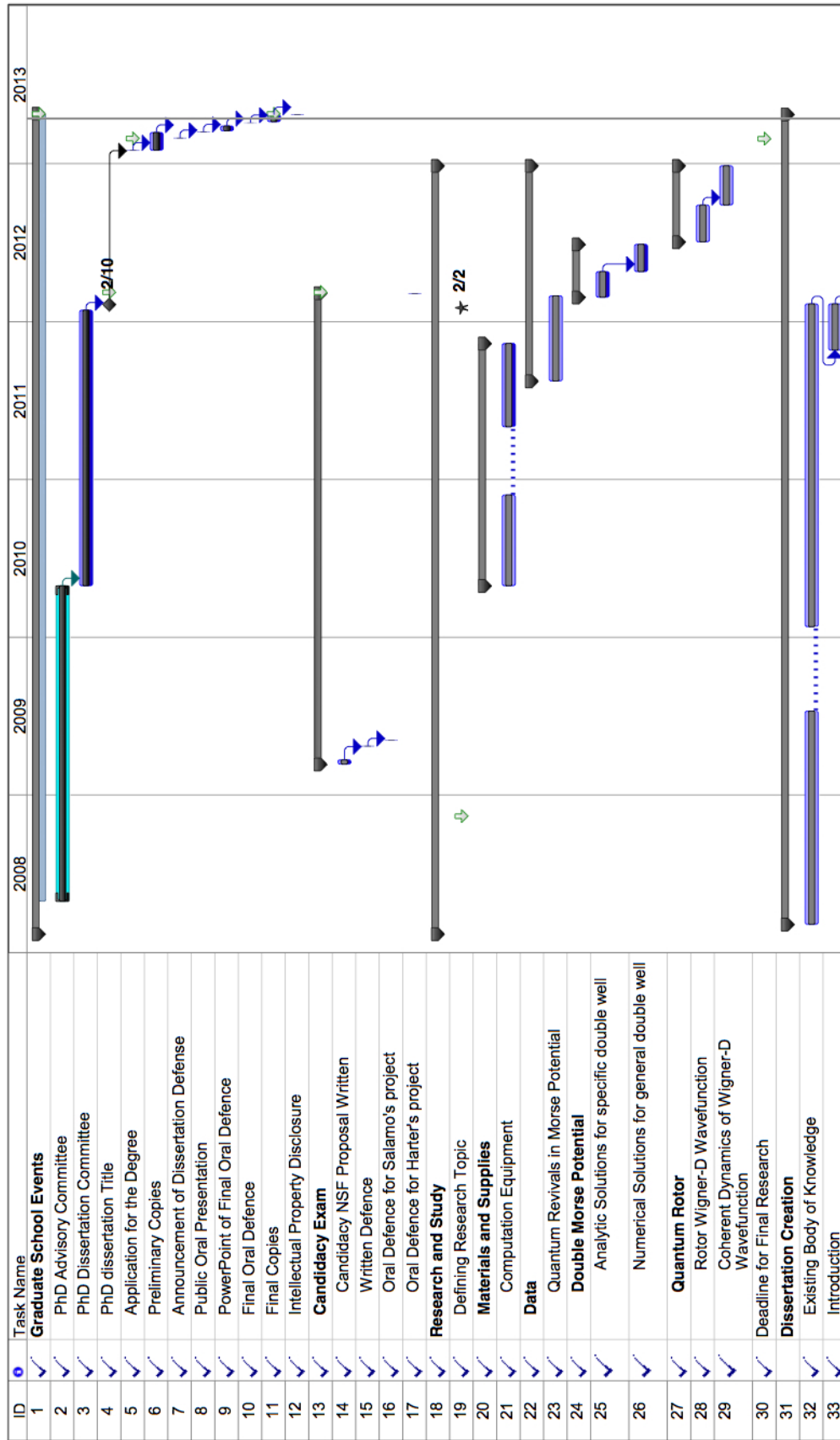
The idea or concept of quantized period is created for the first time, will have profound impact on U.S. and global society. In this dissertation research, the author proposed and developed a creative idea that in a certain quantum world, there is existing a minimum or fundamental period, any completely period is made of the fundamental period integrally. Thus, the completely period of a quantum world is quantized. For this reason, a instant method for global knowledge distribution of this dissertation contents should be considered.

D.3 Impact of Research Results on the Environment

This research method is purely theoretical way that does not have any unfavorable or harmful environmental impact. However, this research method of double-well or bistable system may potentially be applied to model the environment problems.

Appendix E

Microsoft Project Printout of Microelectronics-Photonics PhD Degree Plan



ID	Task Name	2008	2009	2010	2011	2012	2013
34	Chapter 2 (Morse Oscillator)						
35	Chapter 3 (Double Morse Oscillators)						
36	Chapter 4.1 (Rotor Wavefunctions)						
37	Chapter 4.2 (Rotor Dynamics)						
38	Conclusion						
39	First Version						
40	Final Version						
41	Deadline for Final Publication						
42	Boardcasting of Research Works						
43	Publication						
44	Evolution of Holed Nanostructures by Ga Droplet Epitaxy						
47	Holed Nanostructures by Al droplet epitaxy on GaAs Substrate						
56	Footprint of Self-driven Ga Droplet on GaAs Substrate						
61	Quantum Revivals in Morse Potential						
62	Initial Version						
63	Revised Version						
64	Final Version						
65	Conference						
66	Apple Developer Worldwide Conference 2009						
67	Villa Nanostructures Conference 2009 on US Virgin Island						
68	Nano Cruise Conference 2009 in San Diego						
69	MRS Fall Conference 2009 in Boston						
70	Abstract for Oral Presentation						
71	APS March Conference 2012 in Boston						
72	Abstract for Oral Presentation						
73	Registration						
74	Oral Presentation						
75	International Spectroscopy Conference 2012 in Ohio Columbus						
76	Abstract for Oral Presentation						

ID	Task Name	2008	2009	2010	2011	2012	2013
77	Registration						
78	Oral Presentation						
79	International Spectroscopy Conference 2013 in Columbus, Ohio						
80	Abstract for Oral Presentation						
81	Registration						
82	Deadline for Final Publication						



Project: Zhenhua Alvason Li Project1
Date: Mon 4/15/13

Task		External Milestone		Manual Summary Rollup	
Split		Inactive Task		Manual Summary	
Milestone		Inactive Milestone		Start-only	
Summary		Inactive Summary		Finish-only	
Project Summary		Manual Task		Progress	
External Tasks		Duration-only		Deadline	

Appendix F

Identification of All Software Used in Research and Dissertation Generation

Computer #1:

Model Number: MacBook Pro

Serial Number: W88494381GN

Location: Laptop

Owner: A. Zhenhua Li

Software #1:

Name: Mathematica 8 for Students

Purchased by: A. Zhenhua Li

License #: 3226-6762

Software #2:

Name: Microsoft Office 2008 for Mac

Purchased by: A. Zhenhua Li

Product ID #: 92464-498-6887922-12071

Software #3:

Name: BaKoMa Tex

Purchased by: A. Zhenhua Li

Serial Number: 18727P1584

Appendix G

All Publications Published, Submitted and Planned

G.1 Publications in Journal Papers

First Author:

1. **"Quantum Revivals of Morse Oscillator and Fibonacci-Farey-Ford Geometry"**, Alvason Zhenhua Li, William G. Harter, *in reviewing and publishing processing*, 2013.
2. **"Holed Nanostructures Formed by Aluminum Droplets on a GaAs Substrate"**, Alvason Zhenhua Li, Zhiming M. Wang, Jiang Wu, and Gregory J. Salamo. *Nano Res.*, 3: 490-495 (2010).
3. **"Evolution of Holed Nanostructures on GaAs"**, Alvason Zhenhua Li, Zhiming M. Wang, Jiang Wu, Yanze Xie, Kim A. Sablon, and Gregory J. Salamo.

Multiple First Authors:

1. **"Critical size of self-propelled motion of droplets on GaAs (100) surface"**, Jiang Wu, Zhiming M. Wang, Alvason Z. Li, Mourad Benamara, Jihoon Lee, Sabina D. Koukourinkova, Eun Soo Kim, and Gregory J. Salamo. *J. Appl. Phys.* 112, 043523 (2012)
2. **"Nanoscale Footprints of Self-Running Gallium Droplets on GaAs Surface"**, Jiang Wu, Zhiming M. Wang, Alvason Z. Li, Mourad Benamara, Shibin Li, Gregory J. Salamo. *PLoS ONE* 6(6): e20765. doi:10.1371/journal.pone.0020765 (2011)
3. **"On the Secondary Droplets of Self-Running Gallium Droplets on GaAs Surface"**, Wu, Jiang; Wang, Zhiming M.; Li, Alvason Z.; Benamara, Mourad; Salamo, Gregory J.. *ACS Applied Materials & Interfaces*, 3, 6, 1817-1820 (2011)

G.2 Publications in Conference Abstracts and Contributed Talks

1. "Resonance and revival in Quantum Rotors: Comparing half-integer and integer spin", *International Symposium on Molecular Spectroscopy, 68th Meeting* (2013)
2. "Resonance and revival in Morse Oscillator and double Morse Well Dynamics", *International Symposium on Molecular Spectroscopy, 67th Meeting* (2012)
3. "Quantum Revivals of the Morse Oscillator in Position Space and Momentum Space", *American Physical Society March Meeting* (2012)
4. "Nanorings of Aluminum Droplet Epitaxy on GaAs Substrate", *Materials Research Society Fall Meeting* (2009)

EigenWaves Morse Well

■ Physical Constants

```

resolutionX = 600;

meter = 100 cm;
kg = 1000 gm;
joule = meter kg meter second^-2;
c = 2.99792458 × 10^8 meter second^-1;
h = 6.62606957 × 10^-34 joule second;
ħ =  $\frac{h}{2\pi}$ ;
mole = 6.02214129 × 10^23;

```

■ Fibonacci Numbers

■ Molecular Parameters

```

ωe = wee cm^-1 (2 π c); (* the harmonic frequency of classical small vibrations
length ro *)
ωX = wx cm^-1 (2 π c); (* anharmonic frequency *)
m1 = 40 gm mole^-1;
m2 = 40 gm mole^-1;

nmaxN =  $\frac{\omega_e - \omega_X}{2 \omega_X}$  // N
nmax1 = Floor  $\left[ \frac{\omega_e - \omega_X}{2 \omega_X} \right]$ 

```

■ Morse Potential

$$\mu = \frac{m_1 m_2}{m_1 + m_2} \quad (* \text{ reduced mass } *)$$

$$D = \frac{\omega e^2}{4 \omega \chi} \quad (* \text{ dissociation energy } *)$$

$$a = \sqrt{\frac{\omega e^2 * \mu}{2 D}}$$

$$\gamma = \frac{4 D}{\hbar \omega e}$$

cm = 1; gm = 1; second = 1;

$$s[n_] := \frac{\gamma - 2 n - 1}{2}$$

$$y[x_] := \gamma * \text{Exp}[-a x]$$

$$\text{VM}[x_] := D (1 - \text{Exp}[-a x])^2 \quad (* \text{ Morse Potential } *)$$

$$\text{En}[n_] := \hbar \omega e \left(n + \frac{1}{2} \right) - \hbar \omega \chi \left(n + \frac{1}{2} \right)^2$$

$$\psi_M[n_, x_] := \sqrt{\frac{a (\gamma - 2 n - 1) (n!)}{\text{Gamma}[\gamma - n]}} * y[x]^{s[n]} * \text{Exp}\left[-\frac{y[x]}{2}\right] * \text{LaguerreL}[n, 2 s[n], y[x]]$$

The lowest m wavefunctions in Double Morse Potential

■ Solving for C_n and S_n

$m = 22$

22

- Solving for $\{C_1$ (supposedly it is known), $C_3, C_5, C_7, \dots\}$
- Solving for $\{S_1$ (supposedly it is known), $S_3, S_5, S_7, \dots\}$
- Setup C_n and S_n

$C_1 = \xi; S_1 = \xi;$

$\text{Table}[C_{2n+1} = (C_{2n+1} / C_{nn}[[1]])[[n]], \{n, 1, \frac{m}{2} - 1\}];$

$\text{Table}[S_{2n+1} = (S_{2n+1} / S_{nn}[[1]])[[n]], \{n, 1, \frac{m}{2} - 1\}];$

■ Solving for Wavefunction

$h = 1; \kappa = 1; \mu = 1;$

$x_{\min} = -3; x_{\max} = 3; d = 2;$

$\xi = N[m \text{ Sech}[2d], 48] (* \xi = n \text{ Sech}[2d] \text{ for making sure that } x=d, V = (\xi \text{ Cosh}[2x] - m)^2 = 0 *)$

$E_n = N[\text{Re}[\text{Union}[E_n, E_{no}], 48]$

$\text{Sort}[\%, \text{Greater}] // \text{Column}$

$\psi_{mm}[x_] := \text{Exp}\left[\frac{-1}{2} \xi \text{Cosh}[2x]\right]$

$\psi_{MMel}[x_, n_] := \psi_{mm}[x] \psi_{Even}[x] / . E_{nn} \rightarrow E_n[[n]]$

$\psi_{MMol}[x_, n_] := \psi_{mm}[x] \psi_{Odd}[x] / . E_{nn} \rightarrow E_n[[n]]$

$\psi_{MM1} = \text{Table}[\{\psi_{MMel}[x, 2n+1], \psi_{MMol}[x, 2n+2]\}, \{n, 0, \frac{m}{2} - 1\}] // \text{Flatten};$

Wigner-D Wave of (γ as variable)

- Rotor Wave (γ as variable) for Symmetric Top

```

arrayNumber = 12; resolutionP = 200;
j = 2.5;
mL = j;

alpha = 0; beta = pi/2;
pRange = All;
gammaMin = 0;
If [IntegerQ[j], gammaMax = 2 pi, gammaMax = 4 pi];
gammaMax
4 pi

■ Hamiltonian of Symmetric Top : I_x = I_y ≠ I_z
(* Hamiltonian of Symmetric Top I_x=I_y≠I_z *)
Ejnn[j_, mB_] := (Ix j (j + 1) + (Iz - Ix) mB^2) h
Ejn[j_, mB_] := Ejnn[j, mB] / Ejnn[j, 0.5] (* for simplify the energy level expression *)
(* Parameters for ammonia NH3: *)
Izz = sqrt[5 - 1] / 2 // N (* Golden Ratio *)
Ixx = 1;
Iz = h^2 / (2 Izz); Ix = h^2 / (2 Ixx);
h = 1;
0.618034

■ Hamiltonian of Symmetric Top : I_x = I_y ≠ I_z
coherentPsiD[j_, mL_, alpha_, beta_, gamma_, t_] := Sum[Conjugate[WignerD[{j, mL, mB}, alpha, beta, gamma]] Exp[-i (Ejn[j, mB] - Ejn[j, 1.5]) t] / h, {mB, -j, j}]
tmin = 0;
tmax = 2 pi / (Ejn[j, 1.5] - Ejn[j, 0.5]);

```